PHYSIK–DEPARTMENT

Development and experimental implementation of a physical concept for quality assurance of new CT methods

Doktorarbeit

von

Claudia Christine Brunner

TECHNISCHE UNIVERSITÄT
MÜNCHEN

TECHNISCHE UNIVERSITÄT MÜNCHEN

Fachbereich Strahlenphysik

Development and experimental implementation of a physical concept for quality assurance of new CT methods

Claudia Christine Brunner

Vollständiger Abdruck der von der Fakultät für Physik der Technischen Universität München zur Erlangung des akademischen Grades eines

Doktors der Naturwissenschaften

genehmigten Dissertation.

Vorsitzender:	Univ.-Prof. Dr. Martin Zacharias
Prüfer der Dissertation:	
	1. Hon.-Prof. Dr. Herwig G. Paretzke
	2. Univ.-Prof. Dr. Franz Pfeiffer

Die Dissertation wurde am 24.11.2010 bei der Technischen Universität München eingereicht und durch die Fakultät für Physik am 21.03.2011 angenommen.

Contents

Zusammenfassung

Um der stetig steigenden Strahlenbelastung durch die Computertomographie entgegenzuwirken, werden, unter anderem, neuartige CT-Systeme entwickelt. Ob diese Systeme aber tatsächlich mit weniger Dosis die gleiche Bildqualität erzielen, muss mit geeigneten Verfahren untersucht werden. Deshalb beschäftigt sich diese Arbeit mit neuen Methoden zur Qualitätsanalyse von CT-Bildern und ihrer Anwendung auf die neu entwickelte CT-Geometrie CT d'Or. Standardmäßig wird die Bildqualität heute mit auf Fouriertransformation basierenden Methoden ausgewertet, bei denen die Auflösung mit der Modulationsübertragungsfunktion und das Rauschen mit dem Rauschleistungsspektrum bestimmt wird. Da bei der Fouriertransformation Annahmen gemacht werden, die von digitalen Systemen nicht erfüllt werden, wurde in dieser Arbeit zusätzlich ein pixel-basiertes Verfahren verwendet, das die Daten im Bildraum analysiert. Nachdem dieser Ansatz bisher nur auf die 2-dimensionale Radiographie angewendet wurde, mussten zuerst entsprechende Methoden zur Messung und Datenverarbeitung für CT-Bilder mithilfe bekannter Systeme entwickelt und getestet werden. Dies geschah in Zusammenarbeit mit der U.S. Food and Drug Administration, an deren Labor-CT-System die ersten Untersuchungen durchgeführt wurden. Außerdem wurde die bildraum-basierte Methode auch an einem konventionellen CT-Gerät des Klinikums rechts der Isar der Technischen Universität München getestet und die Ergebnisse wurden mit denen der Standardverfahren verglichen.

Anschließend wurden beide Verfahren auf die Bilder des CT d'Or Systems angewendet. Dazu wurde der vorhandene CT d'Or Demonstrator so umgebaut, dass er nun in Kombination mit einem klinischen CT-Gerät betrieben werden kann. Die Datenverarbeitung wurde im Vergleich zum Vorgängerprojekt deutlich verbessert und für die Kombination mit CT-Daten optimiert. Außerdem wurde erstmals die Dosis im CT d'Or gemessen und mit der Dosis im herkömmlichen CT verglichen.

Es zeigte sich, dass durch die Abschirmungen des Demonstrators die Dosis im Ring um über 60 % reduziert wird. Die Bildqualität bleibt jedoch vor allem aufgrund der geringen Sensitivität und Anzahl der im Demonstrator verwendeten Detektoren hinter der von herkömmlichen CT-Geräten zurück.

Die Anwendung des bildraum-basierten Verfahrens auf die verschiedenen Systeme ergab, dass der Ansatz einen deutlich höheren Mess- und Rechenaufwand mit sich bringt als die Standardverfahren. Die Eigenschaften des bildgebenden Systems werden aber teilweise besser beschrieben als durch die Fouriermethoden.

1. Introduction

1.1. History of Computed Tomography

“Ordinary X-ray examinations of the head had shown the skull bones, but the brain had remained a gray, undifferentiated fog. Now, suddenly, the fog had cleared”. With these words Professor Torgny Greitz awarded 1979 the Nobel Prize in Physiology and Medicine to Allan McLeod Cormack and Sir Godfrey Hounsfield for the invention of the computed tomography (CT). Their work was based on the findings of Johann Radon, an Austrian mathematician, that the distribution of a material or material property in an object layer can be calculated if the integral values along any number of lines passing through the same layer are known [Rad17]. In the 1960’s, Allan McLeod Cormack from Tufts University in Massachusetts [Cor73] and Sir Godfrey Hounsfield in Hayes, United Kingdom at EMI Central Research Laboratories [Hou73] applied this theory to medical applications. Hounsfield was lucky to work for EMI, which made its money those days mostly with the enormous success of the Beatles, providing Hounsfield with almost unlimited fundings for his research[Goe10]. Therefore, he was able to build the first prototype of a CT scanner in 1971. An image of it is shown in Fig 1.1a in comparison to a modern CT scanner in Fig. 1.1b.

The type of CT scanner presented by Hounsfield in 1971 is called “first generation CT”. It consisted of a single pencil beam and a single detector element, which were rigidly connected.

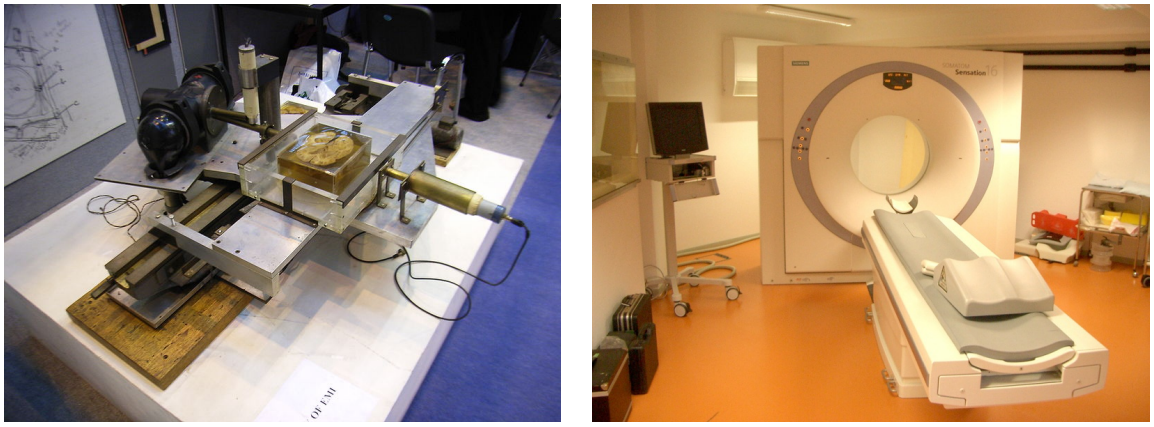

(a) (b)

Figure 1.1: *The very first CT prototype invented by Godfrey Hounsfield (a) and a modern CT scanner for comparison (b). (Source: Wikipedia)*

The source was translated across the patient to obtain a set of 160 parallel projection measurements in one direction as shown schematically in Fig. 1.2a [Hsi03]. The source-detector pair was then repeatedly rotated about 1° and subsequent sets of measurements were obtained during each translation passing the patient. In this way the scan of a single slice took several minutes, which led to severe image quality problems due to patient motion.

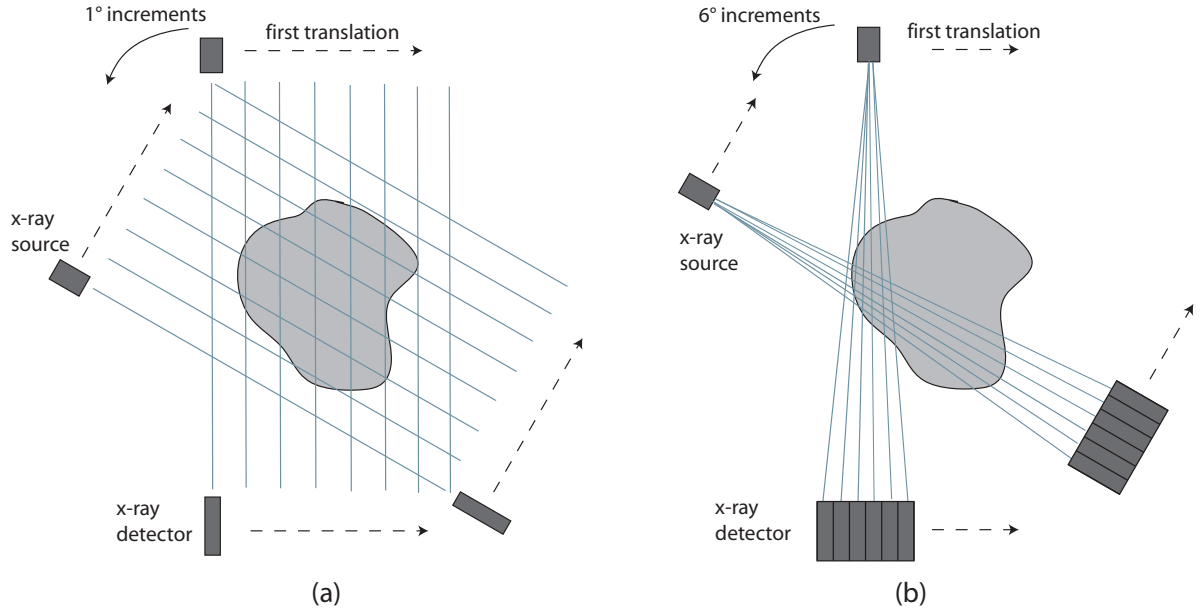

Figure 1.2: *First generation (a) and second generation (b) CT scanner geometry.*

In order to reduce the data acquisition time, the second generation of CT scanners used a source with a narrow fan beam and a row of detectors to sample the data. A scheme of the geometry is provided in Fig. 1.2b. It allowed the collection of several projections during one translation what made the data acquisition significantly more efficient and with about 20 seconds per slice also much faster than the first generation scanners.

The third generation uses a wide fan beam combined with an arc of detectors concentric to the source, which rotates around the patient (Fig. 1.3). The fan beam and the size of the detector is large enough so that the entire patient is in the field of view in each projection and the translational movement is therefore redundant. The early models of the third generation scanners suffered from problems with entangled cables, which required an alternating clockwise and counterclockwise rotation of the gantry. The so called slip-rings solved this problem and cleared the way for spiral CT devices [Kal90]. Nearly all state-of-art scanners on the market today are third generation spiral CTs.

Fourth generation scanners tried to overcome the drawbacks of the third generation, such as detector instability and aliasing, with an enclosed detector ring, which remains stationary during the scan, while the x-ray source rotates around the patient [Hsi03]. This geometry however suffers from severe problems with scattered radiation, because each detector cell receives photons

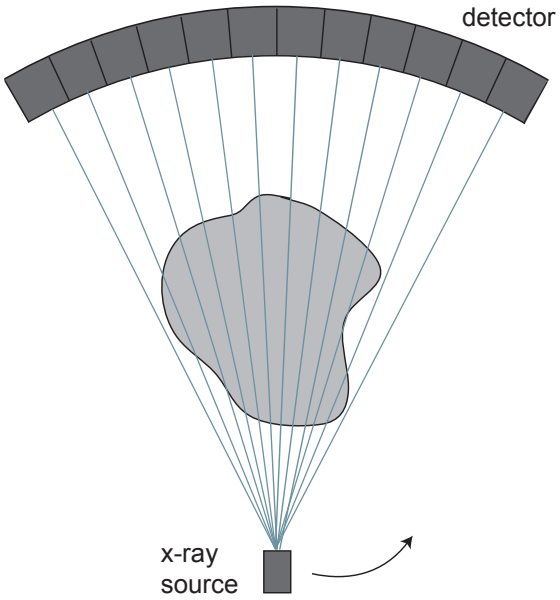

Figure 1.3: *Third generation scanner geometry*

over a wide angle so that no effective and practical scatter rejection can be performed by post-patient collimation. Furthermore, the huge amount of detectors needed to obtain a resolution comparable to a third generation scanner drastically increases the prize of fourth generation scanners. Therefore, instead of adopting the fourth generation technology, third generation scanners have been constantly improved.

The z-flying focal spot technique uses a periodic motion of the focal spot in the longitudinal direction to double the number of simultaneously acquired slices with the goal of improved longitudinal resolution and elimination of spiral artifacts. Together with the implementation of multislice detectors, the scanning time was drastically reduced so that these techniques became standard in modern CT scanners. Online tube current modulation [Kal99, Gre04] decreased the applied dose to the patient significantly by adjusting the tube current to the attenuation in each projection. Dual-source CT systems (DS-CT), working with two tubes and two corresponding arc detectors with an angular offset of 90°, allowed a temporal resolution down to 83 ms for coronary CT angiography in 2006 [Flo06]. Flat-detector computed tomography (FD-CT) promises a higher spatial resolution than conventional arc detectors, but still suffers from drawbacks such as a lower dose efficiency, a smaller field of view, a lower temporal resolution, and scatter [Kal07].

To complete the overview about CT systems, the inverse-geometry volumetric CT, presented by Schmidt et al. in 2004 [Schm04], has to be mentioned. It suggests a complete different geometry with a source array and multiple flat detector arrays of the same axial extent. It is able to image thick volumes in a single gantry rotation with isotropic resolution and without

cone-beam artifacts [Maz07]. But though it is a promising approach, the inverse-geometry CT is work in progress and therefore still has to prove its clinical feasibility.

1.2. Health risks

According to the Bundesamt für Strahlenschutz [BfS08], dose exposure from natural sources is in the range from 2 to 3 mSv per year in Germany. Artificial sources add in average another 2.0 mSv/a to this value, of which 1.8 mSv/a originate almost completely from medical examinations. The composition of the average radiation exposure of the German population is shown in Fig. 1.4a.

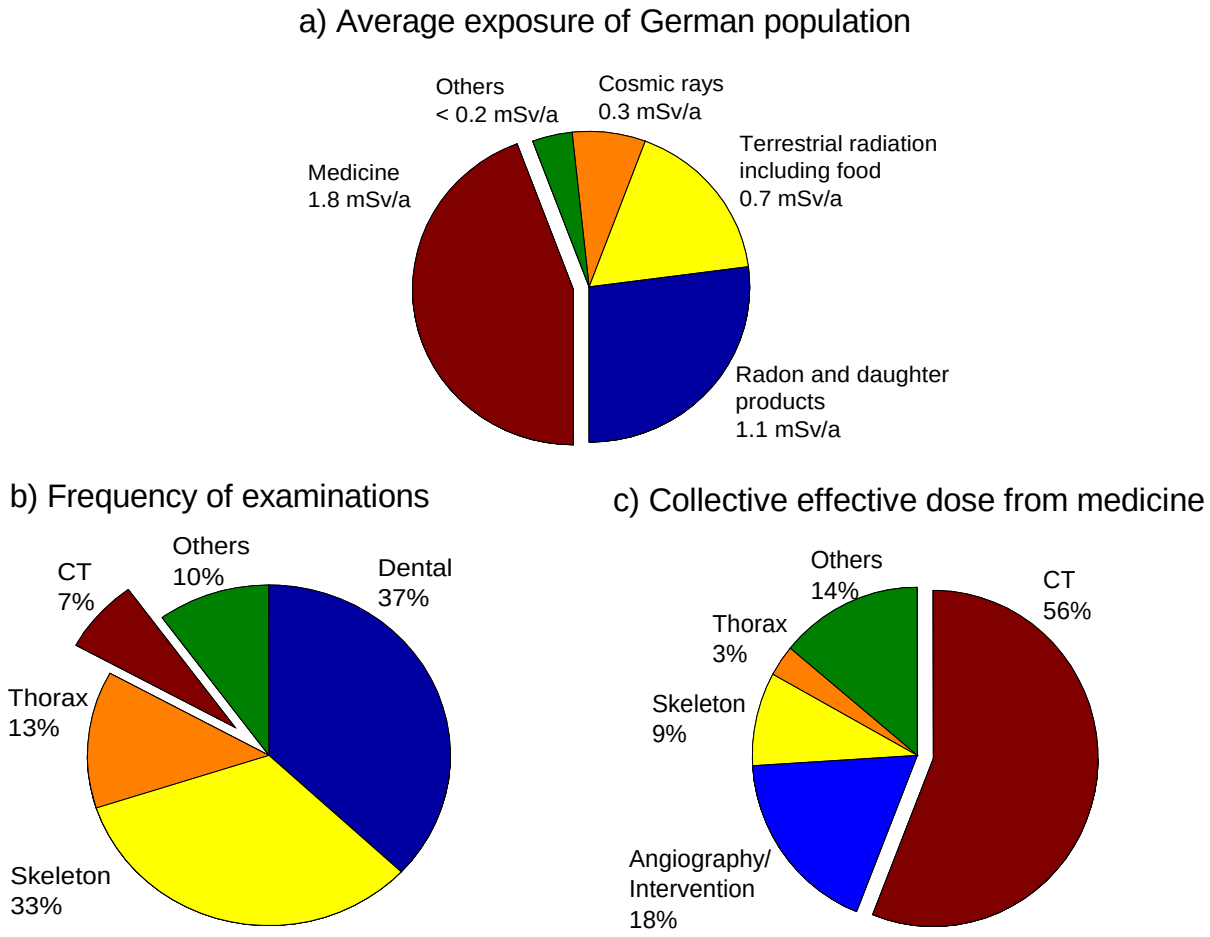

Figure 1.4: *Statistics on radiation exposure of an average German citizen.*

Figures 1.4b and c show that while CT imaging represents only 7 % of the medical examinations using x-rays, it contributes 56 % to the collective effective dose from medicine. CT scans represent therefore the largest articifical contribution to the radiation exposure in Germany. For other industrial nations the contribution of CT to the overall dose is in the same order of magnitude or even higher, as for example for the USA and Japan [Bri05]. Researchers at Emory

University in Atlanta reported in August 2009 that examination records of nearly 1 million US citizens collected by insurance companies showed that 68 % had at least one CT scan in three years [Faz09].

The International Commission on Radiological Protection (ICRP) [ICRP07] reports that CT is increasingly being used to replace conventional x-ray studies. Figure 1.5 shows that while the radiation exposure from all other medical applications except CT decreased in the last years, the dose from CT constantly increased.

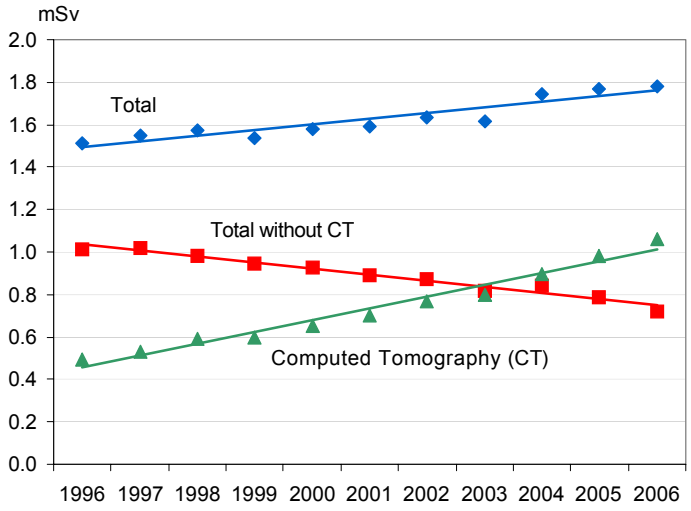

Figure 1.5: *Statistics on radiation exposure of an average German citizen [BfS08].*

However, the values mentioned above are collective effective doses (i.e., averaged over a whole population), the dose for an individual patient can be several times higher. For example, the adult effective dose from a CT exam of the head is about 2 mSv and therefore equivalent to the adult effective dose from roughly 100 chest x-ray examinations. The effective dose from a CT exam of the abdomen with a typical value in the range of 16 mSv equals about 800 chest x-ray examinations [FDA10].

Stochastic effects caused by this amount of radiation, which for example lead to an increased life time risk for cancer, are not yet fully understood. While there are theories that low doses might even decrease the risk of developing cancer through the activation of an adaptive response that may protect against radiation effects ("hormesis") [Fei05], there are also theories that claim low doses to be disproportionate more dangerous ("supra-linear") [Gof92]. The general scientific consensus, however, is currently the linear-no-threshold (LNT) hypothesis [Wal06], which involves epidemiological data at higher doses to establish an "anchor point", and extrapolates the excess cancer risk linearly down from this point to the low dose of interest [Bre06]. This implicates that every radiation exposure is a possible risk for the person concerned, what led to the recommendation of the ICRP and the American Association of Physicists in Medicine (AAPM) to keep the patient dose as low as reasonable achievable, the so-called ALARA principle [ICRP07, AAMP08, RoeV02].

However, since no immediate radiation effects appear from typical CT scans, the awareness of the population and even of the physicians and medical staff for health risks due to the applied radiation dose is commonly still low. This attitude changed slightly when several accidents in connection with CT were reported in fall 2009 [Bog09]. One of them happened in a small community hospital in Arcata, North California, where a two and a half year old boy, who complained about neck pain after falling from his bed, was accidentally subjected to CT scans for more than an hour. Skin irritations were an immediate consequence of this extreme overexposure, and radiation experts predict that the child will develop cataracts in three to five years. Additionally, since children are much more sensitive to radiation than adults, there is an unpredictable rise in the boy's life cancer risk.

Another series of accidents was reported from the famous Cedars-Sinai Medical Center in Los Angeles, where over 200 potential stroke patients were administered up to eight times the regular dose. The American College of Radiology (ACR) and American Society of Neuroradiology (ASNR) have thereupon released a joint statement calling for an established set of CT scan and radiation dosage protocols [Bye09]. The National Institutes of Health (NIH) started to record the medical examinations with x-rays and the dose the patients were exposed to so that the number of tests past and the estimated cancer risk for the patient is available for the attending physician [Kri09]. It is supposed that this information might influence his or her decision to order a particular type of exam and prevent the patient from unnecessary imaging procedures that have already been conducted.

In February 2010, the U.S. Food and Drug Administration (FDA) announced an initiative to reduce unnecessary radiation exposure from the three greatest contributors to total radiation exposure from medical imaging procedures: CT, nuclear medicine studies, and fluoroscopy [FDA10]. The goal is to promote safe use of medical imaging devices, support informed clinical decision making, and increase patient awareness. In addition, the FDA and the Centers for Medicare and Medicaid Services are collaborating to incorporate key quality assurance practices into the mandatory accreditation.

In Germany, the Bundesamt für Strahlenschutz tries to reduce CT doses by introducing reference values for a various number of scans [RoeV02, BfS10]. These reference values provide the maximum necessary dose for a various number of diagnostic and interventional scans. The updated version includes for the first time four examinations for children at six different age brackets and weight categories respectively. Institutions which do not meet the reference values are advised of how to optimize their procedures.

1.3. Aims of this work

Since the risk due to low dose exposures is still unknown and CT contributes more and more to the effective average dose of the population, dose reduction in CT is a very urgent goal of efficient radiation protection. Overall, reducing dose to the patient in CT depends mainly

on two points (Fig. 1.6): CT technology and quality assurance. Existing CT technology can be improved in hardware as well as in software, but there are limitations. Inventing new approaches is challenging and very time-consuming, but has the potential to overcome these limitations. One of these inventions is the new reconstruction algorithm OPED (Orthogonal Polynomial Expansion on the Disc) (Sec. 2.1.2), which is not based on the Fourier slice theorem in contrast to the conventionally used filtered back projection algorithm (FBP) (Sec. 2.1.1). The new CT geometry CT d'Or (CT with Dual Optimal Reading) (Sec. 2.2) takes advantage of OPED's special characteristics by introducing a mask, which works both as a shielding and as a second detector. Combined, OPED and CT d'Or allow a theoretical dose reduction of up to 50 % while providing the same image quality as conventional CT systems using FBP. However, these theoretical predictions still have to be verified. Taking steps towards proving them is therefore one of the aims of this work.

This leads to the second main point important for dose reduction in CT: the quality assurance. In clinical routine, this implicates controlling the strict implementation of the ALARA principle in the investigation protocols and the avoidance of unnecessary investigations. Additionally, quality assurance implicates the regular check of the CT scanners. CT devices are defined by the quality of the produced images and the dose which has to be applied to obtain these images. Only both parameters in combination allow a meaningful estimation of the system quality.

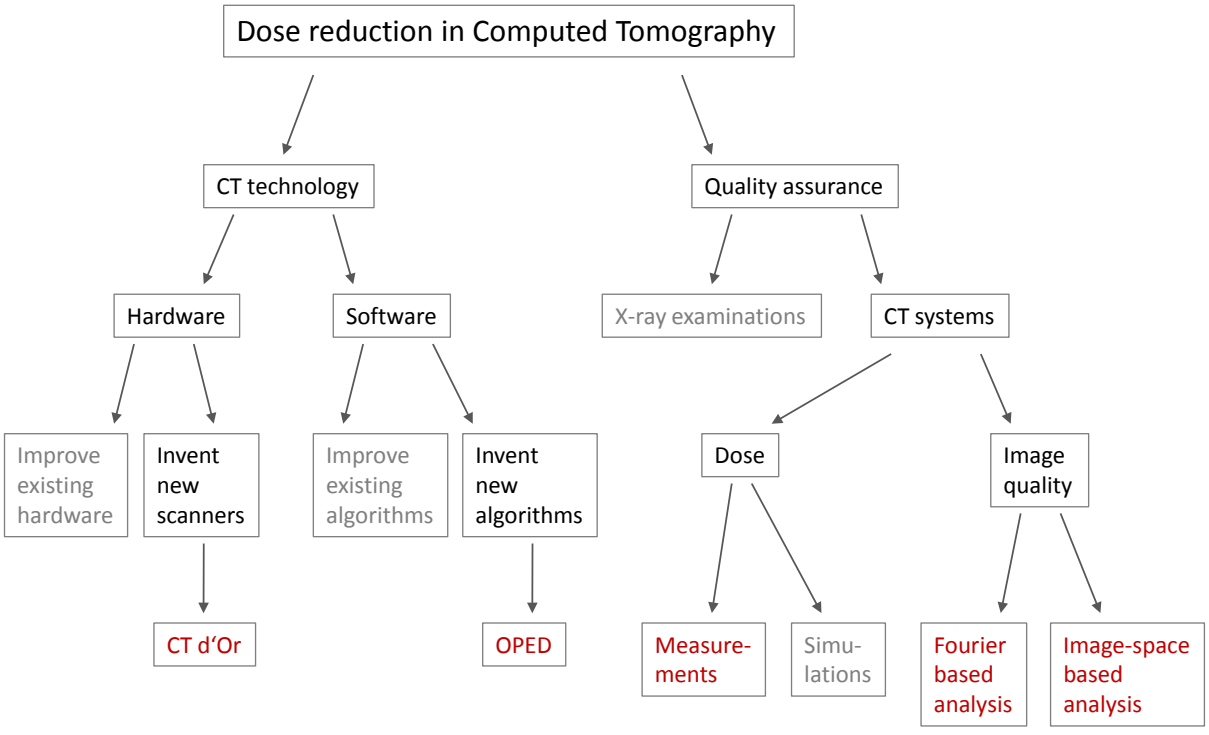

Figure 1.6: *The various ways to reduce dose in computed tomography provided the motivation for this work.*

Image quality analysis is conventionally done using the Fourier based methods which quantify the spatial resolution by the modulation transfer function (MTF) and the noise by the noise power spectrum (NPS) (Sec. 2.3.1). However, the Fourier approach makes some limiting assumptions for digital systems such as shift invariance and wide sense stationarity, which are not satisfied by real CT systems. Therefore, the application of an image-space based approach to CT was developed additionally, which defines spatial resolution and noise in the object space (Sec. 2.3.2). Since it is not yet an established method, the image-space approach was not only compared to the conventional Fourier approach, but its adaptability and practicability for CT and CT d'Or was verified too.

In detail, the image-space approach was first applied to a laboratory cone-beam CT, which allowed to control all parameters of the measurement and the reconstruction. The comparison to the results of the Fourier approach revealed the similarities and differences of the two approaches. The subsequent application to a clinical CT tested the adaptability of the image-space approach to systems where not every parameter can be controlled or is known. It furthermore demonstrated the potential of the two approaches and the achievable image quality of a modern CT scanner.

Since the hardware of new CT scanners has to be characterized too, but its properties are masked by the reconstruction algorithm and applied filter, a method to analyze the raw data with the Fourier approach was developed. This was done for the clinical CT, but an application to new CT systems such as the CT d'Or would be straightforward, because the spatial resolution and the noise were determined independently of the number of acquired slices.

In order to analyze the image quality of the CT d'Or, first the existing demonstrator was improved. It can now be combined with a clinical CT scanner so that for the first time it can be run in the configuration it was originally invented for. In the course of this modification, a completely new concept for image reconstruction had to be developed. Comparisons to images reconstructed with the old algorithms demonstrated the considerable improvement in image quality. The combination with the clinical CT and the new algorithms allowed to apply the previously developed methods for image analysis with the image-space approach and the Fourier approach. In order to thoroughly describe this combined system, additional dose measurements were performed.

2. Theoretical background

This chapter provides an overview of the theory essential for the work presented here. First the two applied reconstruction algorithms, the filtered backprojection algorithm and OPED, are shortly presented in Sec. 2.1. Then the new scanning geometry CT d'Or, which is combined with OPED, is described in Sec. 2.2. Finally, two approaches for image analysis, the conventional Fourier based and an image-space based approach, are presented and their main differences are emphasized in Sec. 2.3.

2.1. Image reconstruction

2.1.1. The filtered backprojection algorithm

The filtered backprojection (FBP) algorithm is the most commonly used reconstruction algorithm, implemented in almost every conventional CT scanner. Like every reconstruction algorithm, it is based on the Radon transform, which provides the basis for image reconstruction from 1-dimensional projections [Kak01]. The object is represented by a two-dimensional function $f(x, y)$ and each line integral through it by the parameters (θ, t), where t is the distance of the line to the origin and θ is the angle between the normal vector to the line and the x-axis. A line j through the object is then described by

$$t_j = x \cos\theta_j + y \sin\theta_j, \tag{2.1}$$

which leads to the definition of the line integral as

$$P_\theta(t) = \int_{(\theta,t)line} f(x, y)ds. \tag{2.2}$$

The Radon transform $P_\theta(t)$ of $f(x, y)$ is defined by rewriting this equation using a delta function

$$P_\theta(t) = \int_{-\infty}^{\infty}\int_{-\infty}^{\infty} f(x, y)\delta(x\cos\theta + y\sin\theta - t)dxdy. \tag{2.3}$$

A projection is formed by combining a parallel set of line integrals as given by $P_\theta(t)$ for a constant θ.

The Fourier Slice Theorem states that the Fourier transform of $P_\theta(t)$

$$F(u, v) = \int_{-\infty}^{\infty}\int_{-\infty}^{\infty} f(x, y)e^{-j2\pi(ux+vy)}dxdy \tag{2.4}$$

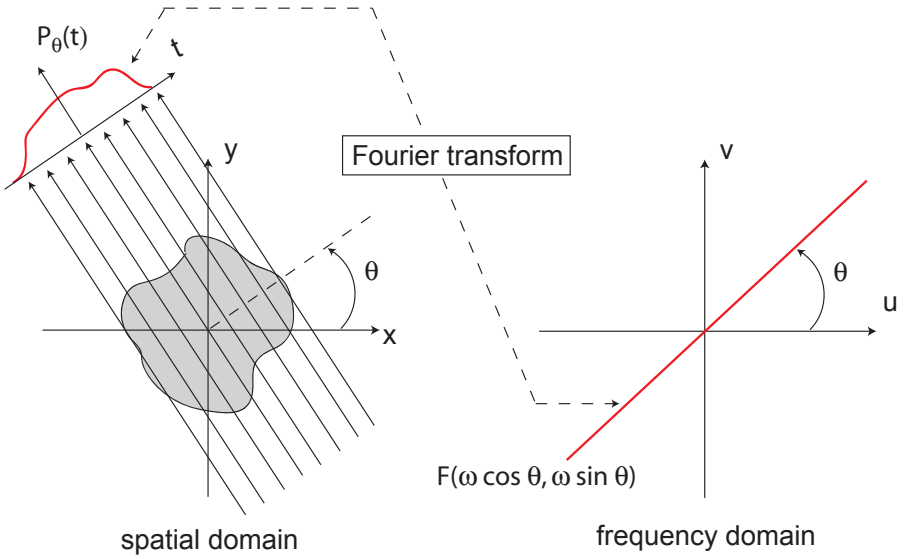

Figure 2.1: *The Fourier Slice Theorem relates the Fourier transform of a projection to a line through the origin in the frequency space.*

is a line through the origin of the Fourier domain rotated by the angle θ, where u and v are frequencies in the Fourier space. This concept is depicted in Fig. 2.1.

For an infinite number of projections, $F(u, v)$ is known for all points in the frequency domain and the object $f(x, y)$ can be recovered by using the inverse Fourier transform:

$$f(x,y) = \int_{-\infty}^{\infty} \int_{-\infty}^{\infty} F(u,v) e^{j2\pi(ux+vy)} du dv. \tag{2.5}$$

However, in practice only a finite number of projections can be taken so that $F(u, v)$ is only defined along a finite number of radial lines, which have to be interpolated or regridded to a Cartesian coordinate system.

The FBP algorithm solves this problem by applying the weighting or ramp filter $\pi \left|w\right| / K$ to each projection in the frequency domain, where w is the distance from the origin of the coordinate system and K is the number of projections. Figure 2.2 schematically shows how the weighting function works. The data needed per projection to know all points in frequency space are supposed to be wedge-shaped (a). The actual measured data are stripes (b), which get wedge-shaped by applying the weighting function on them (c). At each spatial frequency w, the wedge in (c) has the same volume as the pie-shaped wedge in (a), but it is perpendicular to the plane. Thus the weighted projections represent an approximation, which can be improved as much as desired by using an appropriate number of projections.

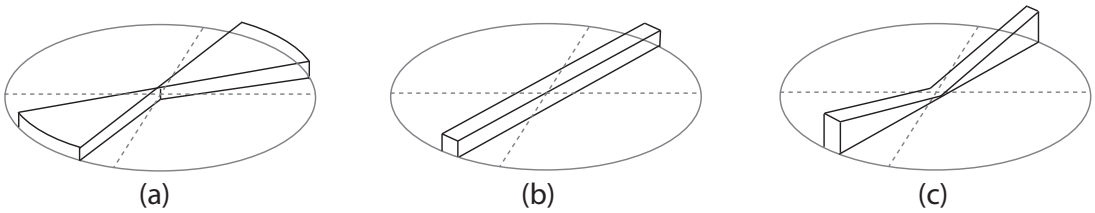

Figure 2.2: *Data in the frequency domain needed per projection (a), the actual measured data (b), and the weighted data (c).*

The ramp filter $|w|$ has to be band-limited in order to enable an inverse Fourier transformation. In other words, there has to be zero energy contained outside the frequency interval $(-\Gamma, \Gamma)$. This is done by multiplying the filter with the window function $b(w)$:

$$b(w) = \begin{cases} 1 & |w| < \Gamma \\ 0 & \text{otherwise.} \end{cases} \tag{2.6}$$

The resulting, band-limited ramp filter $H(w) = |w|\, b(w)$ is shown in Fig. 2.3. The impulse response $h(t)$ of this filter is given by the inverse Fourier transform of $H(w)$ in dependence of the sampling interval $\tau = (2\Gamma)^{-1}$:

$$h(t) = \int_{-\infty}^{\infty} H(w) e^{+j2\pi wt} dw = \frac{1}{2\tau^2} \frac{\sin 2\pi t/2\tau}{2\pi t/2\tau} - \frac{1}{4\tau^2} \left(\frac{\sin \pi t/2\tau}{\pi t/2\tau} \right)^2 \tag{2.7}$$

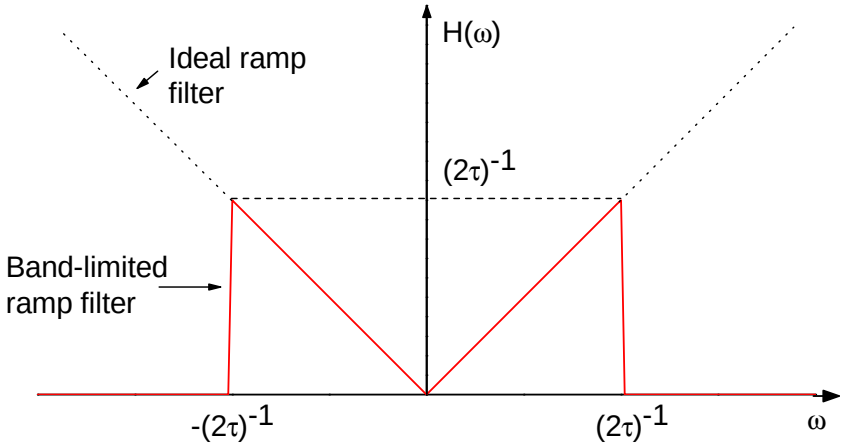

Figure 2.3: *Frequency representation of the band-limited ramp filter* $H(w)$

Since the projection data are measured at discrete τ, $h(t)$ is only defined for n discrete positions:

$$h(n\tau) = \begin{cases} \frac{1}{4\tau^2}, & n = 0 \\ 0, & n = even \\ -\frac{1}{n^2\pi^2\tau^2}, & n = odd. \end{cases} \tag{2.8}$$

The discretized impulse response $h(t)$ of the ideal backprojection filter is shown in Fig. 2.4. Due to the negative values for odd n, noise in CT images reconstructed with the FBP algorithm is anti-correlated (compare Sec. 2.3.2 and Sec. 4.2).

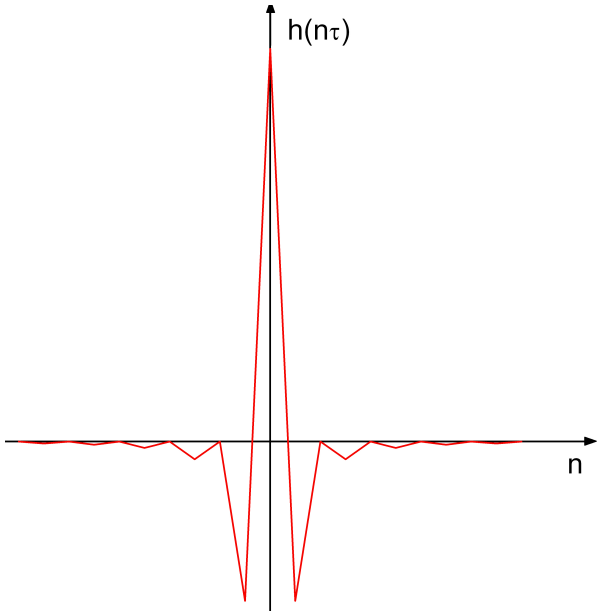

Figure 2.4: *Impulse response of the ideal backprojection filter*

The second step of the FBP algorithm is adding together the 2-dimensional inverse Fourier transforms of each weighted projection. It is called backprojection, because it can be perceived as backprojecting each filtered projection over the image plane. Since in practice each projection is only of finite extent, $P_\theta(k\tau)$ is set to zero outside the index range $k = 0, 1, ..., N-1$. The filtered projection Q_θ is therefore defined as

$$Q_\theta(n\tau) = \tau \sum_{k=0}^{N-1} h(n\tau - k\tau) P_\theta(k\tau), \qquad n = 0, 1, ..., N-1. \tag{2.9}$$

In order to implement the filtering operation in a fast algorithm, multiplication in Fourier space is preferred to convolution in object space. This, however, leads to the implementation of a circular convolution instead of a theoretically correct aperiodic convolution. This approximation results in artifacts, known as the so-called wrap-around effect or interperiod interference. To reduce these artifacts, each projection is zero-padded before applying Fourier transform and filtering operations, meaning that the beginning and the end of the sequence are filled with zeros. If the number of zeros is at least equal to the number of samples in the original projection minus one (N-1), the artifacts can mostly be prevented [Hsi03].

The algorithm discussed above is derived for a parallel-beam geometry not given in modern third generation CT systems. The conversion from fan-beam projection data to parallel-beam data requires a two-step interpolation process called rebinning [Hsi03]. The difference in ray density at the center of the field of view compared to the outer regions is, however, not accounted for, risking a loss of information by performing rebinning [Tis10]. Therefore, other

reconstruction algorithms were developed, which use the data directly without rebinning, such as e.g., OPED.

2.1.2. The reconstruction algorithm OPED

The reconstruction algorithm OPED was proposed and proved to be stable and accurate by Xu in 2006 [Xu06a, Xu06b, Xu07a]. OPED is an acronym for **O**rthogonal **P**olynomial **E**xpansion on the **D**isc.

The implementation of the OPED algorithm referred to here approximates the object function $f(x, y)$ as an expansion of N Chebyshev Polynomials of the second kind U_k:

$$U_k(x) = \frac{\sin[(k+1)\theta]}{\sin\theta}, \qquad x = \cos\theta. \tag{2.10}$$

The Chebyshev polynomials of the second kind are known to generate an orthogonal system with the weight $\sqrt{1-t^2}$ on the interval [-1, 1] [Dun01]

$$\int_{-1}^{1} U_m(t)U_n(t)\sqrt{1-t^2}dt = \int_0^{\pi} \sin[(m+1)\varphi]\sin[(n+1)\varphi]d\varphi = \frac{\pi}{2}\delta_{m,n}, \tag{2.11}$$

where $m, n \geq 0$.

For further considerations, it is necessary to introduce ridge polynomials, which play an important role in the study of Radon transforms [Xu06b]. They are used to define bivariate functions $f(x, y; \theta)$ to be constant along their so-called "ridges" $x\cos\theta + y\sin\theta = t$ at a fixed t:

$$f(x, y; \theta) = f(x\cos\theta + y\sin\theta).$$

For convenience, the Chebyshev polynomials can be denoted in terms of the ridge function

$$U_k(x\cos\theta + y\sin\theta) \equiv U_k(x, y; \theta)$$

Defining $B_2 = (x, y) : x^2 + y^2 \leq 1$ as the unit disc and f as a function such as $f : B_2 \to \mathbb{R}$, then

$$\int_{B_2} |f(x, y)|^2 dxdy < \infty \Leftrightarrow f \in L^2(B_2).$$

For $L^2(B_2)$, it has been shown that [Xu06b]

$$\frac{1}{\pi}\int_{B_2} U_k(x, y; \varphi)U_k(x, y; \varphi)dxdy = \frac{1}{k+1}U_k(\cos(\varphi - \theta)). \tag{2.12}$$

By reducing the ridge angle θ to k equidistantly distributed positions $\theta_{k,j}$ on a circumference

$$\theta_{k,j} = \frac{\pi j}{k+1}, \qquad 0 \leq j \leq k, \tag{2.13}$$

it can be found that the trigonometric polynomials $U_k(x, y; \theta_{k,j}), j = 0, ..., k$ are orthonormal:

$$\frac{1}{\pi}\int_{B_2} U_k(x, y; \theta_{k,j})U_k(x, y; \theta_{k,i})dxdy = \frac{1}{k+1}U_k(\cos(\theta_{k,j} - \theta_{k,i})) \tag{2.14}$$

$$= \frac{1}{k+1}\frac{\sin[(j-i)\pi]}{\sin[(j-i)\frac{\pi}{k+1}]} \tag{2.15}$$

$$= \delta_{j,i}. \tag{2.16}$$

Hilbert theory states that all trigonometric polynomials generate a dense set of $L^2(B_2)$ [Dun01], therefore

$$L_2(B_2) = \overline{\bigcup_{k=0}^{\infty} P_k},$$

where P_k denotes the linear combinations of $U_k(x, y; \theta_{k,j})$. This shows that the set of Ridge Chebyshev polynomials of the second kind

$$U_k(x, y; \theta_{k,j}) = U_k(x\cos\theta_{k,j} + y\sin\theta_{k,j}),$$

where $0 \leq k \leq \infty$ and $0 \leq j \leq k$, generates an orthonormal basis in $L^2(B_2)$. This allows to represent any function $f \in L_2(B_2)$ by an expansion such as

$$f(x, y) = \sum_{k=0}^{\infty}\sum_{j=0}^{k} U_k(x, y; \theta_{k,j})\frac{1}{\pi}\int\int_B f(x, y)U_k(x, y; \theta_{k,j})dxdy, \tag{2.17}$$

where the double integral corresponds to the projection of the function over the corresponding basis vector $U_k(x, y; \theta_{k,j})$. In order to approximate the object function $f(x, y)$, OPED uses N Radon Projections $R_f(\phi_\nu, t)$ obtained at the equidistant view angles

$$\phi_\nu = \frac{2\pi}{N}\nu, \qquad \nu = 0, ..., N-1 \tag{2.18}$$

and at a distance t from the center of the field of view. Recalling the definition of the Radon transform in Sec. (2.1.1), it is possible to relate the expression of f to its Radon projections in basis of Chebyshev polynomials:

$$\int\int_B f(x, y)U_k(x, y; \theta_{k,j})dxdy = \int_{-1}^{1} P_f(\theta_{k,j})U_k(t)dt. \tag{2.19}$$

Therefore, f can be written as an expansion of its Radon projections

$$f(x, y) = \sum_{k=0}^{\infty}\sum_{j=0}^{k} U_k(x, y; \theta_{k,j})\frac{1}{\pi}\int_{-1}^{1} P_f(\theta_{k,j}, t)U_k(t)dt. \tag{2.20}$$

Xu proved two additional properties, which are important for the reconstruction [Xu06b]:

1. For any $0 \leq k \leq N-1$ and $0 \leq \theta \leq 2\pi$,

$$\frac{1}{N}\sum_{\nu=0}^{N-1} U_k(\cos(\theta - \varphi_{nu}))U_k(x, y; \varphi_\nu) = U_k(x, y; \theta). \tag{2.21}$$

2. For any k and $0 \leq \varphi \leq 2\pi$,

$$\sum_{j=0}^{k} U_k(\cos(\theta_{k,j} - \varphi) U_k(x, y; \theta_{k,j})) = (k+1) U_k(x, y; \varphi). \tag{2.22}$$

By using Gaussian quadrature, which has been shown to be exact for polynomials in order of N [Xu06b], the integral from Eq. (2.20) can be rewritten as

$$\frac{1}{\pi} \int_{-1}^{1} P_f(\theta_{k,j}, t) U_k(t) dt = \frac{1}{N} \sum_{j=0}^{N-1} P_f(\varphi_\nu, \cos\psi_j) \sin(k+1)\psi_j, \tag{2.23}$$

where $\cos\psi_j$ denotes the zeros of the Chebyshev polynomials. The resulting formula for the approximation $A_N f$ of f is obtained by truncating the summation over k to have $N-1$ terms

$$A_N f(x, y) = \frac{1}{N} \sum_{\nu=0}^{N-1} \sum_{k=0}^{N-1} (k+1) U_k(x\cos\phi_\nu + y\sin\phi_\nu) \frac{1}{N} \sum_{j=0}^{N-1} P_f(\varphi_\nu, \cos\psi_j) \sin(k+1)\psi_j \tag{2.24}$$

It has to be pointed out that N is the number of projections taken, but it is also the highest grade of the polynomials with which the approximation can be done. The more projections are available, the more polynomials of higher grade can be used for the expansion and the better gets the approximation $A_N f$ of f.

Equation (2.24) resembles a conventional vectorial expansion, which can be intuitively explained. The last term is the summation over the Radon transform of all beams with an angle of ϕ_{nu}. The second term represents the Ridge Chebyshev polynomials of the second kind as the corresponding basis vectors, which are multiplied by the weighting function $(k+1)$. This filter amplifies polynomials with higher grade and is therefore comparable to the weighting function of the FBP algorithm. The shape of the discretized impulse responses of the two algorithms is thus equal, but the scaling is different. Finally, the first term of the reconstruction formula normalizes the expression with the number of projections N.

Equation (2.24) also implies that OPED uses so-called fan-parallel beams in each projection; these are parallel beams distributed according to the zeros of Chebyshev polynomials. Since the zeros of Chebyshev polynomials correspond to equally angular points on the unit circle [Tis06], a CT geometry which makes use of these properties suggests itself. The result is the CT d'Or described in Sec. 2.2.

OPED as well as the FBP algorithm were applied in this work. Therefore, the major similarities and differences are shortly summarized in the following. Both algorithms are based on the Radon transform. However, the FBP algorithm uses the Fourier slice theorem to relate the object to its Radon transform, while OPED uses the expansion with Chebyshev polynomials of the second kind. This expansion is a direct method, which does not need any zero-padding as necessary for the FBP algorithm. Both algorithms use some kind of weighting function resulting in similar impulse responses and anti-correlated noise in the reconstructed images. The

FBP algorithm works with equidistantly distributed parallel data, which have to be created from conventional fan beam scanners by rebinning the data. OPED, by contrast, works with fan-parallel data, which can be directly obtained by reordering the fan beam data. The computing time of the OPED algorithm has been shown to be at least the same as for the FBP algorithm [Xu07b] and with a fast implementation it is up to about 20 - 30 times faster [Xu09]. However, a complete and detailed comparison between OPED and the FBP algorithm still has to be done. 3-dimensional reconstruction with OPED has not yet been published, but in principle, the Feldkamp scheme can be applied in a similar way as in the implementation for the FBP algorithm. It is supposed to be even more straightforward, because an additional interpolation to obtain equidistant rays in the cone as described by Grass [Gra00] is not necessary for OPED.

2.2. The new scanning geometry CT d'Or

In addition to the health risks due to the deposited dose (Sec. 1.2) and the interpolations necessary for the FBP algorithm (Sec. 2.1.1), there are further drawbacks in current CT devices [Her08b]:

- Scattered radiation produces additional noise in the images.
- Due to a minimal rotation time down to 300 milliseconds [ImPACT10] and a gantry weight of up to 2 tons [ImPACT09], the centrifugal forces in the gantry are enormous. This leads to mechanic instabilities, which result in a slight nutation of the gantry around the center, thereby decreasing the accuracy of the data collection.
- A single reading of a detector takes finite time during which the detector slightly moves, so that the effective size of the detector seems to be broader than it really is.

A third generation CT in combination with a collimation mask with shieldings on the side of the x-ray source can overcome these drawbacks (Fig. 2.5). The windows between the shieldings are supposed to have the same width as the shieldings itself in order to let only half of the radiation cross the mask. The amount of radiation applied to the patient in a whole rotation can theoretically be halved by using shieldings made of high-absorption material such as lead, thick enough to prevent the transmission of photons completely. By installing detector elements on the inner side of the mask, two complementary data sets can be collected: One with the inner detectors of the collimation mask (Fig. 2.5)(red), the other with the arc detector of a conventional CT scanner (blue). Thus the system has been denoted: **CT** with **D**ual **O**ptimal **R**eading (CT d'Or). Each of the complementary data sets produces a self-contained sinogram and a corresponding reconstruction. However, only the combination of both allows to fully exploit the potential of CT d'Or in combination with OPED. In order to combine the data sets there are two possibilities: One is to combine the fan data, the second is to add the two reconstructed images. The first method is more accurate and therefore promising to produce

sharper images and suppress artifacts effectively. However, if the two detector sets do not have the same sensitivity, this method is likely to produce ring artifacts. The second method is much less prone to different sensitivities of the detector sets, but if the reconstruction or the alignment of both images was not very accurate, it is likely to produce images more blurred than the first method.

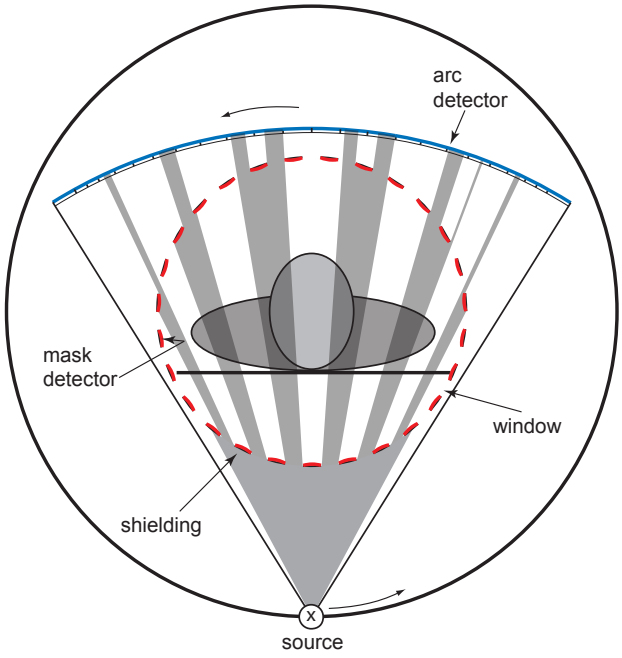

Figure 2.5: *Concept of the CT d'Or with the arc detector of a conventional CT scanner (blue) and an additional collimation mask with shieldings outside and detectors inside (red). (By courtesy of Hugo de las Heras)*

The CT d'Or is especially suitable for the combination with OPED, because it acquires fan-parallel data. Figure 2.6 demonstrates how each ray of a fan is parallel to one ray of another fan for both data sets.

The special geometry of the CT d'Or solves the problems of current CT devices that are mentioned above:

- Scatter is avoided to a fair amount.
- The shieldings allow a direct correction for scattered radiation, because the count rates of the detectors shielded from direct radiation can be used to estimate the amount of scattered radiation. This information can be used to correct the detector signals for scattered radiation and therefore improve the image quality [Schl06, Schl08].
- Gantry movements do not decrease the accuracy of data collection anymore, since each photon belongs to a correct ray due to the collimation.

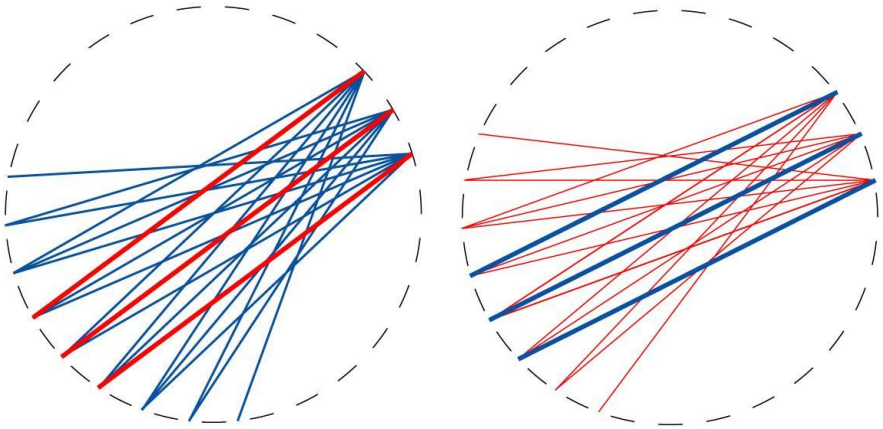

Figure 2.6: *These schemes of a simplified mask with 27 detectors and the fan beams after a rotation about 40° show that each ray of a fan is parallel to one ray of another fan for the mask detectors (a) and the arc detector (b). (By courtesy of Hugo de las Heras)*

- In the same way, the finite reading time of the detectors does not decrease the image resolution anymore.

2.3. Image quality analysis

An intuitive definition of image quality rates an image by whether the radiologist can use it for a meaningful interpretation. This definition, however, is based on a subjective individual human judgment not appropriate to measure the performance of imaging systems objectively. In order to overcome this problem, a variety of techniques has been developed, which have in common that they analyze the resulting image of a known input signal. As a figure of merit for the system performance, the signal-to-noise ratio (SNR) has been established. It is based on the assumption that in order to be detectable an object must have a contrast to its surroundings which is higher or at least equal to the relative standard deviation of the noise [Ang05]. However, the SNR also depends on the shape and amplitude of the signal, the background and the superimposed noise.

In order to study the dependence on these parameters, different tasks have been formulated. The simplest one is the signal-known-exactly/background-known-exactly task (SKE/BKE), where a signal with known parameters such as size, shape and location has to be detected in additive, uncorrelated Gaussian noise on a known background. The SKE/BKE-task is approximated by the Rose model, which provides the relationship between the number of image quanta and the perception of detail [Bur99]. Having a uniform background with a mean number of quanta per unit area $\bar{q}_b$ and an object with a mean number of quanta per unit area $\bar{q}_o$, the contrast C can be defined as:

$$C = \frac{\bar{q_b} - \bar{q_o}}{\bar{q_b}}. \tag{2.25}$$

The Rose signal difference ΔS_{Rose} is defined as the difference between the mean number of quanta in the area connected to the object and the mean number of quanta in an equally sized area A in the background region:

$$\Delta S_{\mathrm{Rose}} = (\bar{q_b} - \bar{q_o})A. \tag{2.26}$$

Rose defined noise as the standard deviation σ_b in the number of quanta $\bar{q_b}$ in an area with the same size as A in the background region [Beu00]. For uncorrelated noise, the Poisson statistics describes the standard deviation as:

$$\sigma_b = \sqrt{Aq_b}. \tag{2.27}$$

Since the SNR is defined as the ratio of the output signal to the standard deviation, the $\mathrm{SNR}_{\mathrm{Rose}}$ is given by

$$\mathrm{SNR}_{\mathrm{Rose}} = \frac{\Delta S_{\mathrm{out}}}{\sigma_b} = \frac{A(\bar{q_b} - \bar{q_o})}{\sqrt{Aq_b}} = C\sqrt{Aq_b}. \tag{2.28}$$

The SNR provides information about the detectability d' of the object and thus about its detection probability p [Kyp05a]. For a SKE/BKE situation, d' equals the SNR [ICRU96]

$$d'_{\mathrm{SKE/BKE}} = \mathrm{SNR}. \tag{2.29}$$

For a two-alternative forced-choice experiment (2-AFC) for example [Kyp05a], p can be related to d' by

$$p = \frac{1}{2}\left(1 + \mathrm{erf}(\frac{d'}{2})\right), \tag{2.30}$$

where $\mathrm{erf}(\frac{\mathrm{d}'}{2})$ denotes the error function

$$\mathrm{erf}(\frac{d'}{2}) = \frac{2}{\sqrt{\pi}} \int_0^{\frac{d'}{2}} \exp[-y^2]dy. \tag{2.31}$$

The resulting sigmoidal curve is plotted in Fig. 2.7. Since there are only two possibilities in a 2-AFC experiment, the detection probability is 0.5 for $d' = 0$. The detection threshold is usually defined as the stimulus intensity at which $p = 0.75$ [Ulr04].

The means or strategy by which the task gets done is called the observer or decision-maker. The observer of a clinical image is normally a radiologist, but much research effort is being expended on the development of computer algorithms for such tasks. The so-called ideal observer uses all statistical information available in order to maximize the task performance. Therefore, it provides an upper bound against which all other observers can be compared. However, if the signal or the background are only known statistically, the ideal observer may not be calculable or may require lengthy numerical calculations using Monte Carlo simulations. The ideal observer has furthermore the disadvantage that it overestimates the performance of the human observer, who lacks the ability to account for correlations in image noise effectively [ICRU96].

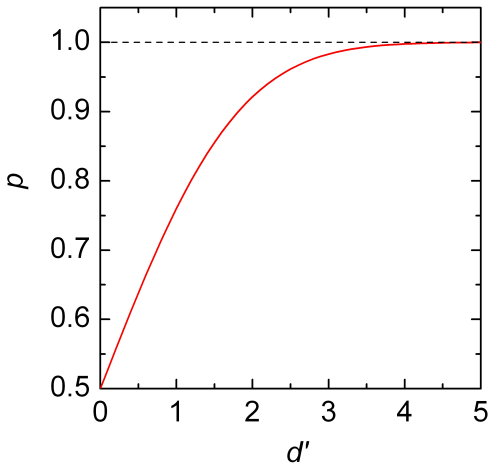

Figure 2.7: *The detection probability p of the object against its detectability d' for a two-alternative forced choice.*

When analyzing clinical imaging systems that will have human observers as end-users, it is therefore desirable to use model observers that are more tractable and that reflect the capabilities of the human observer. The Hotelling observer [Hot31] is a commonly used alternative, because it demonstrates the maximum discrimination ability among all observers that are limited to perform only linear operations on data [Bar85, Bar90]. In essence, the Hotelling approach models the data as Gaussian, regardless of its true statistics. Moreover, it has been found to usefully predict the human performance for a variety of discrimination tasks.

In this work, the SNR has therefore been calculated based on the Hotelling-observer model. Parameters influencing the SNR such as spatial resolution and noise were determined in two different ways: the conventional Fourier based approach and an image-space based approach originating from statistical information theory. Both approaches are described in the following.

2.3.1. Fourier based approach

In the 1970's, figures of merit were developed to specify the spatial resolution and the noise of 2-dimensional radiographic systems. In order to compare the performance of different systems, the methods had to be applicable on analog screen-film systems and processable with the limited computational powers available at that time. The Fourier based concepts of the modulation transfer function (MTF) and the noise power spectrum (NPS) fulfilled these criteria and became the standard method for describing the image quality in radiographic systems. Widely-used and accepted, these concepts were also adapted for modern digitalized systems and CT.

Modulation transfer function

The MTF describes the transfer of an input contrast through the imaging system. It is defined as the ratio of the output modulation to the input modulation for a linear system [Hsi03]. Consider the transfer of a sinusoidal signal $h(x)$

$$h(x) = a + be^{i2\pi ux} \tag{2.32}$$

where u is the spatial frequency. $h(x)$ is real and corresponds to the measurable input signal [Beu00]. The modulation of $h(x)$ is given by

$$M_{in} = \frac{|h_{max}| - |h_{min}|}{|h_{max}| + |h_{min}|} = \frac{(a+b) - (a-b)}{(a+b) + (a-b)} = \frac{b}{a}. \tag{2.33}$$

The output signal $d(x)$ can be derived from the convolution of the signal $h(x)$ with the impulse-response function (IRF) $\mathrm{irf}(x)$

$$\begin{aligned} d(x) &= h(x) * \mathrm{irf}(x) \\ &= \int_{-\infty}^{\infty} h(x')\mathrm{irf}(x - x')dx' \\ &= \int_{-\infty}^{\infty} (a + be^{i2\pi ux'})\mathrm{irf}(x - x')dx' \\ &= a\int_{-\infty}^{\infty} \mathrm{irf}(x - x')dx' + b\int_{-\infty}^{\infty} e^{i2\pi ux'}\mathrm{irf}(x - x')dx' \\ &= aT(0) + bT(u)e^{i2\pi ux} \end{aligned} \tag{2.34}$$

where $T(0)$ equals the area under the IRF and is therefore real, while $T(u)$, in general, is complex. The modulation of the output is given as

$$M_{out} = \frac{|d_{max}| - |d_{min}|}{|d_{max}| + |d_{min}|} = \frac{b}{a}\frac{|T(u)|}{T(0)} = M_{in}\frac{|T(u)|}{T(0)}. \tag{2.35}$$

The MTF is defined as the ratio of the output modulation to the input modulation

$$\mathrm{MTF}(u) = \frac{M_{out}}{M_{in}} = \frac{|T(u)|}{T(0)}. \tag{2.36}$$

By definition, $\mathrm{MTF}(u)$ is unity at $u = 0$.

If the IRF is real, which is generally the case for x-ray imaging systems, then $T(u)$ and $\mathrm{MTF}(u)$ are even. This means that both functions can be expressed in terms of positive frequencies only. For systems where the IRF is real and even, $T(u)$ is also real and even and no phase-transfer information is lost by taking the absolute value to calculate the MTF.

The MTF of CT systems is normally calculated taking the absolute value of the Fourier transform of the point spread function (PSF). The PSF is the response of the system to an ideal point object or a Dirac delta function, $\delta(x, y)$. Since ideal point objects do not exist, thin wires or beads consisting of high-absorption material are commonly used to approximate the PSF. For

an object larger than the limiting spatial resolution of the system, a sinc or a Bessel function can be used to correct the finite extension of the object.

An "ideal", analogous system has a constant MTF equal to 1 for all frequencies, because the input signal is transfered without any degradation through the system. For digital systems, the photons are integrated over pixels of width s so that even the "ideal" MTF always decreases with the sinc function $|\mathrm{sinc}(\pi s u)|$ [Beu00]. Therefore, the MTF of digital systems depends strongly on the frequency. The spatial resolution of a system is often referred to as the frequency value where the MTF decreased to 0.1 [Kal05].

Noise power spectrum

There are two types of noise in the projection data. The first one is a continuously varying error due to electrical noise, variation of detection efficiency or roundoff errors. The second type of noise is a function of the number of x-ray photons that exit the object [Kak01]. The noise power spectrum (NPS) describes the variance of image intensity (i.e., image noise) for a uniformly irradiated image divided among the various frequency components of the image. In other words, the NPS defines the variance (per frequency bin) of a given spatial-frequency component in an ensemble of measurements of that spatial frequency [Beu00]. The magnitude of the NPS reflects thereby the degree of randomness at each spatial frequency and the integral of noise power over all frequencies yields the variance [Rie78]. A concentration of noise power in low-frequency space is due to a coarse graininess of the images, while a concentration in high-frequency space is caused by a finer graininess.

Homogeneous noise images in air (2-dimensional radiography) or in water (CT) are used to calculate the NPS. The images are divided in M squared regions of interest (ROIs), which are Fourier transformed separately. The size of the ROIs is not fixed but is an optimum that balances two opposing effects. Increasing the size of the ROIs increases the number of spatial-frequency points at which the NPS is calculated, but leads to an increased uncertainty in the NPS curve. A decrease of the ROI size results in more averaging, but a less well-defined NPS curve [Pad05]. In order to benefit from the advantages of both sides, ROIs are often chosen to overlap by up to half their size in horizontal and vertical direction in practice. A potential zero-offset and general trends are corrected by fitting and subtracting a second-order polynomial $S(x_i, y_j)$ from the data. The NPS for digitalized systems with an image intensity of $I(x_i, y_j)$ is therefore defined as

$$NPS(u_n, v_k) = \frac{\Delta x \Delta y}{M N_x N_y} \sum_{m=1}^{M} \left| \sum_{i=1}^{N_x} \sum_{j=1}^{N_y} [I(x_i, y_j) - S(x_i, y_j)] e^{-2\pi i (u_n x_i + v_k y_j)} \right|^2 \tag{2.37}$$

where $\Delta x, \Delta y$ is the pixel size and N_x, N_y is the size of the ROIs in horizontal and vertical direction respectively [Beu00].

The NPS in reconstructed CT images is mainly influenced by the design of the reconstruction filter applied in a particular algorithm. Edge-enhancing filters increase the noise for frequencies

relevant for object detection, while smoothing filters decrease the noise, but with it also the spatial resolution.

Fourier based SNR

The MTF describes the signal transfer of the Fourier transformed input signal $|\mathbf{FT}(\Delta \mathrm{S_{in}})|$ through the imaging system. Integrating over all frequencies gives the output signal $\Delta \mathrm{S_{out}}$

$$\Delta \mathrm{S_{out}(f)} = \int \mathrm{MTF}(f) \cdot |\mathbf{FT}(\Delta \mathrm{S_{in}(f)})| df. \tag{2.38}$$

Furthermore, the variance of the background is defined by the NPS so that the standard deviation σ is given by $\sqrt{\mathrm{NPS}}$. For the Hotelling observer [ICRU96], the Fourier based $\mathrm{SNR^2_{Fourier}}$ for a SKE/BKE-task can therefore be derived from Eq. (2.28)

$$\mathrm{SNR^2_{Fourier}} = \frac{\Delta S^2_{\mathrm{out}}}{\sigma^2} = \int \frac{\mathrm{MTF}(f)^2 \cdot |\mathbf{FT}(\Delta \mathrm{S_{in}(f)})|^2}{\mathrm{NPS}(f)} df. \tag{2.39}$$

Inherent assumptions of the Fourier approach

However, the Fourier representation is only valid if the imaging system is linear shift invariant and wide sense stationary [Bar04]. Wide sense stationarity means that the mean value is constant, the variance is finite and the autocovariance is only depending on the relative distance between two pixels. However, neither Poisson noise nor electrical noise fulfill these criteria. The mean and the autocovariance function of a process constituted by an incident x-ray photon depend therefore on the location on the detector. Also the finite size of the imaging system spoils the stationarity criterion, because the autocovariance function could only be invariant when a "digital wrap-around" would be assumed, meaning that two pixels at opposite sides of the array would have the same covariance as two adjacent pixels. This assumption has no physical basis so that it can be stated that the assumptions made by the Fourier approach are not fulfilled by real imaging systems. An approach which does not need these assumptions is the image-space based approach presented in the next section.

2.3.2. Image-space based approach

The change from analog to digital systems in radiography and an increasing computational power allowed the development of alternative approaches for image analysis. A new, modern image evaluation methodology has been developed from concepts based on statistical decision theory. Its application to digitalized images is straightforward, because it is image-space based and it models the system properties using matrix operators. The deterministic properties of an imaging system are described by the H-matrix, and the noise in the images is described by the covariance matrix.

H-matrix

The H-matrix $\mathbf{H}$ describes the transfer of a signal through the imaging system [Bar04, Kyp06a, Kyp08, Kyp09] by mapping a discrete object $\mathbf{f}$ to an image $\mathbf{g}$

$$\mathbf{g} = \mathbf{H}\,\mathbf{f}\,. \tag{2.40}$$

The dimensionality of $\mathbf{H}$ is $M \times N$, where M is the total number of image pixels in $\mathbf{g}$ and N is the total number of elements in the discretized object $\mathbf{f}$. Since M and N are normally not equal, $\mathbf{H}$ is rectangular in general so that a singular value decomposition has to be performed in order to analyze the matrix. Therefore, a Hermitian square matrix is constructed using the matrix product of $\mathbf{H}^\dagger$ and $\mathbf{H}$. The eigenanalysis is then written as

$$\lambda_n \mathbf{u}_n = \mathbf{H}^\dagger \mathbf{H} \mathbf{u}_n \tag{2.41}$$

where λ_n and $\mathbf{u}_n$ are the sorted eigenvalues and eigenvectors of $\mathbf{H}^\dagger\mathbf{H}$. λ_n defines the magnitude of each eigenvector transferred through the system and $\sqrt{\lambda_n}$ corresponds to the singular values of $\mathbf{H}$ [Kyp08].

Equation (2.41) is of special significance, because it generates a set of orthonormal eigenvectors $\mathbf{u}_n$ that form the basis of the imaging system. Since $\mathbf{u}_n$ are orthonormal vectors, they form a complete basis of length N. Consequently, any object $\mathbf{f}$ can be written as an expansion in terms of these eigenvectors:

$$\mathbf{f} = \sum_{n=1}^{N} \alpha_n \mathbf{u}_n, \tag{2.42}$$

where the expansion coefficients α_n are given by the scalar product

$$\alpha_n = \mathbf{u}_n^\dagger \mathbf{f}. \tag{2.43}$$

Since the rank R of $\mathbf{H}$ is in general less than N, the eigenvalues $\boldsymbol{\lambda}_n$ are real and positive only for $n < R$ and zero otherwise. This means that eigenvectors $\mathbf{u}_n$ with $n > R$ are not transferred by the imaging system. Such functions are referred to as null functions of the imaging system. The object can therefore be separated into the measurable part $\mathbf{f}_{\text{meas}}$ and the null part $\mathbf{f}_{\text{null}}$ [Bar04]:

$$\mathbf{f} = \mathbf{f}_{\text{meas}} + \mathbf{f}_{\text{null}} \tag{2.44}$$

where

$$\mathbf{f}_{\text{meas}} = \sum_{n=1}^{\mathrm{R}} \alpha_n \mathbf{u}_n \tag{2.45}$$

and

$$\mathbf{f}_{\text{null}} = \sum_{n=\mathrm{R}+1}^{N} \alpha_n \mathbf{u}_n \qquad \text{with} \qquad \mathbf{H}\mathbf{f}_{\text{null}} = 0 \tag{2.46}$$

In practice, $\mathbf{H}$ is calculated from a 2-dimensional point spread function (PSF), which is sampled in computed tomography from a thin wire or a bead (compare Sec. 2.3.1) [Kyp08, Liu09].

The measured PSF is the image **g**. The corresponding object **f** can be created as an array with an infinitesimal thin signal on exactly one entry (the position of the wire in **g**) and no signal on all other entries. In order to calculate **H**, **f** and **g** are reformed to 1-dimensional vectors. By shifting the PSF and therefore shifting the position of the signal in **g** and **f**, each column of **H** can be calculated. This is schematically shown in Fig. 2.8, where each color represents a different position of the PSF.

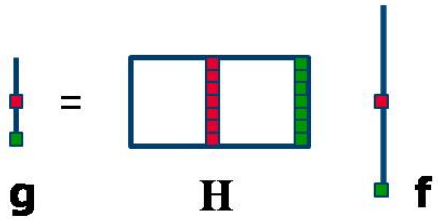

Figure 2.8: *From each position of the infinitesimal thin signal in* **f** *and its image in* **g**, *one column of* **H** *can be calculated.*

In order to describe the system properties accurately, the PSF has to be shifted with a higher resolution than the pixel size. This means that **g** is shifted for one-third or one-forth of the image pixel size at a time, resulting in **f** to be 9 to 16 times larger than **g**. Since this gets very computational intense for large images, a convenient size for **g** is 32×32 pixels, resulting, with a 3-fold resolution, in a H-matrix with a size of $32^2 \times (3 \cdot 32)^2 = 1024 \times 9216$.

Covariance matrix eigenanalysis

A way to describe noise in an image without applying Fourier transformation is by calculating the covariance matrix **K** of the noise [Bar04]. It quantifies whether fluctuations in one pixel are statistically related to fluctuations in another one. For an image **g** with the dimensions N_x x N_y, **K** is given by

$$K_{ij} = \langle (g_i - \overline{g_i})(g_j - \overline{g_j})^* \rangle \,, \tag{2.47}$$

where the asterisk indicates complex conjugate, allowing for the possibility that components of **g** might be complex.

If g_i and g_j are statistically independent, then $K_{ij} = 0$. The diagonal elements of the covariance matrix are the variances of the components

$$K_{jj} = \mathrm{Var}\,\{g_j\} \,. \tag{2.48}$$

The covariance matrix can also be expressed as an outer product

$$\mathbf{K} = \left\langle (\mathbf{g} - \overline{\mathbf{g}})(\mathbf{g} - \overline{\mathbf{g}})^\dagger \right\rangle = \left\langle \Delta\mathbf{g}\Delta\mathbf{g}^\dagger \right\rangle \,, \tag{2.49}$$

where $\Delta\mathbf{g} = \mathbf{g} - \overline{\mathbf{g}}$ with $\overline{\mathbf{g}}$ being the mean vector.

To study the quantum noise of an imaging system, let $\mathbf{g}$ be one realization of the flat-field. $\mathbf{K_g}$ can be diagonalized

$$\mathbf{K_g} = \mathbf{\Phi M \Phi^\dagger} \tag{2.50}$$

where $\mathbf{M}$ is the diagonal matrix of the eigenvalues and $\mathbf{\Phi}$ is a unit-less square matrix, whose columns are the eigenvectors of $\mathbf{K_g}$.

Since $\mathbf{K}$ is an Hermitian matrix, i.e. $K_{ij} = K_{ji}^*$, it has some special properties, which make it easy to work with:

- The set of eigenvectors $\mathbf{\Phi}$ spans a complete orthonormal vector space. $\mathbf{\Phi}$ is also a unitary matrix, i.e. $\mathbf{\Phi^{-1}} = \mathbf{\Phi^\dagger}$.
- The eigenvalues of $\mathbf{K}$ are real, even if $\mathbf{K}$ is complex.
- $\mathbf{K}$ is always positive-semidefinite, which means that the eigenvalues are greater than or equal to zero. If the covariance matrix is defined appropriately, the eigenvectors are linearly independent and the rank R of $\mathbf{K}$, and accordingly the number of nonzero eigenvalues, equals its dimensions M [Bar04].

Since the eigenvectors $\mathbf{\Phi}$ of a Hermitian operator form a complete, orthonormal set of basis vectors in the relevant space, any image $\mathbf{g}$ can be expressed as:

$$\mathbf{g} = \mathbf{\Phi}\boldsymbol{\beta}, \tag{2.51}$$

where $\boldsymbol{\beta}$ is a $m \times 1$ vector with uncorrelated components $\{\beta_m\}$. This expansion of an image in eigenvectors of its covariance matrix is known as Karhunen-Loève or KL expansion. It allows to visualize the structure of the image noise by plotting the eigenvectors as 2-dimensional arrays of the same size as the ROIs the corresponding covariance matrix was calculated with.

In practice, the covariance matrix is calculated by dividing numerous, statistically independent images in quadratic ROIs [Bru10]. By definition, these ROIs have to be independent from each other so that the pixels in one matrix are not correlated to pixels in another matrix. The autocovariance specifies how far apart two points must be for their fluctuations to be uncorrelated. It is defined by:

$$K(\mathbf{r}_1, \mathbf{r}_2) = \langle [f(\mathbf{r}_1) - \langle f(\mathbf{r}_1)\rangle][f^*(\mathbf{r}_2) - \langle f^*(\mathbf{r}_2)\rangle]\rangle \,. \tag{2.52}$$

White noise has a delta-function correlation, but since the noise in reconstructed images is colored, the correlation is a distribution function as shown in Fig. 2.9a. Due to the filter applied in reconstruction algorithms such as FBP and OPED (compare Sec. 2.1.1 and Sec. 2.1.2), noise in CT images is anti-correlated, leading to negative values of the autocovariance.

The covariance matrices of all ROIs are averaged to result in a covariance matrix like the typical one shown in Fig. 2.9b. The diagonal is brighter than the rest, because the correlation of each pixel with itself, also called variance, is of course higher than the correlation of a pixel with any other pixel. The bright lines besides the diagonal indicate the correlation of each pixel with its neighbors. The dark lines reflect the anti-correlation implemented by the FBP algorithm.

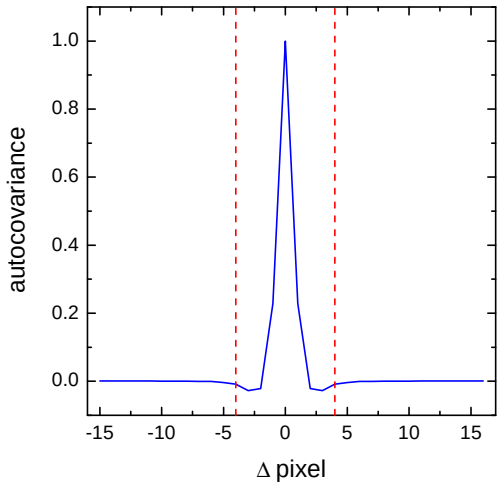

(a) Typical autocovariance function obtained from images reconstructed with a FBP algorithm.

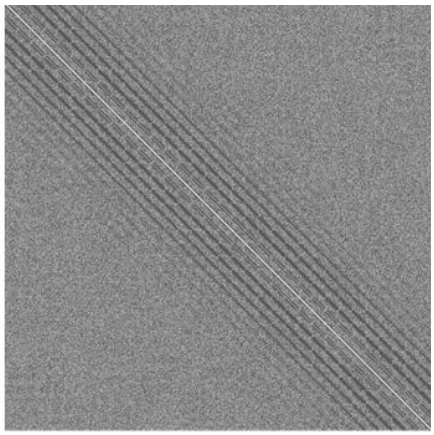

(b) Typical covariance matrix

Figure 2.9: *Principals of calculating the covariance matrix*

Signal-to-noise-ratio

The image-space based approach defines the signal to be detected by an imaging system as the difference between the mean, or noise-free, image $\bar{\mathbf{g}}_{\mathrm{b+s}}$ with a known background that contains the signal to be detected, and the mean, or noise-free, image of the known background $\bar{\mathbf{g}}_{\mathrm{b}}$ [Kyp09]:

$$\mathbf{\Delta S}_{\mathrm{out}} = \bar{\mathbf{g}}_{\mathrm{b+s}} - \bar{\mathbf{g}}_{\mathrm{b}}. \tag{2.53}$$

Using Eq. (2.40) $\mathbf{\Delta S}_{\mathrm{out}}$ can be expressed in terms of the H-matrix and the object $\mathbf{f}$:

$$\mathbf{\Delta S}_{\mathrm{out}} = \mathbf{H}(\bar{\mathbf{f}}_{\mathrm{b+s}} - \bar{\mathbf{f}}_{\mathrm{b}}) = \mathbf{H}\Delta\mathbf{f}. \tag{2.54}$$

For a SKE/BKE task and the Hotelling observer, the SNR for images containing only Gaussian noise is defined in terms of the H-matrix $\mathbf{H}$ and the covariance matrix $\mathbf{K_g}$ [Bar04]:

$$\begin{aligned} \mathrm{SNR}^2_{\mathrm{Image-based}} &= \mathbf{\Delta S}^{\dagger}_{\mathrm{out}} \mathbf{K_g}^{-1} \mathbf{\Delta S}_{\mathrm{out}} \\ &= (\mathbf{H}\Delta\mathbf{f})^t \mathbf{K_g}^{-1} \mathbf{H}\Delta\mathbf{f}. \end{aligned} \tag{2.55}$$

If the imaging system was linear shift invariant and wide sense stationary, $\mathbf{K_g}$ and $\mathbf{H}$ would be diagonalized by Fourier transformation so that

$$\begin{aligned} \mathbf{K_g} &\overset{FT}{\longleftrightarrow} \mathrm{NPS} \\ \mathbf{H} &\overset{FT}{\longleftrightarrow} \mathrm{MTF}. \end{aligned} \tag{2.56}$$

Therefore, the eigenvalues of the covariance matrix and the values of the NPS would be equal and the eigenvectors of the covariance matrix would be exponential wave functions. In the same

manner the singular values of the H-matrix would correspond to the values of the MTF. In this special case, the resulting SNR would be the same for both approaches presented here.

With Eq. (2.56), the image-space $\mathrm{SNR}_{\mathrm{Image-based}}$ of Eq. (2.55) can easily be converted into the Fourier $\mathrm{SNR}_{\mathrm{Fourier}}$ of Eq. (2.39).

Inherent assumptions of the image-space approach

The image-space based approach makes assumptions too. For calculating the covariance matrix, it is assumed that the submatrices used are statistically independent from each other and that the structure and amplitude of the noise is the same for all. By using a large enough pixel spacing between the submatrices the first point can be accounted for, but the second one is hardly given in any reconstructed image. Due to the circular nature of the reconstruction algorithm, whether FBP or OPED, the noise of images does not fulfill this criterion. Furthermore, in order to accurately define the covariance matrix, a huge number of images is necessary. For example, the resulting covariance matrix of 32×32 pixel ROIs has a size of 1024×1024. In order to define this matrix correctly, $1024^2 \approx 10^6$ ROIs would be necessary. In Sec. 6.1 this problem is further elaborated.

3. Imaging Devices

The following chapter describes the different CT systems and experimental set-ups used for this work. The two approaches for image analysis were first applied and tested on a laboratory cone-beam CT system, which allowed to control every single step from image acquisition to reconstruction and analysis (Sec. 3.1). The methods were then applied to a clinical CT device in order to check their applicability to conventional systems and demonstrate the achievable image quality (Sec. 3.2). In order to be able to analyze the image quality of CT d'Or, the data treatment had to be optimized. This was first done for the combination of the CT d'Or demonstrator with the C-arm device (Sec. 3.3, Sec. 3.4.2) and then transfered to the combination with the clinical CT (Sec. 3.4.3).

3.1. FDA laboratory CT system

The studies about the analysis of reconstructed images using the pixel based approach were done in cooperation with the U.S. Food and Drug Administration (FDA). The first experiments were therefore performed at the FDA bench-top flat-panel-based cone-beam CT scanner [Kyp06a, Kyp06b, Kyp07, Kyp08]. A schematic of the experimental set-up and its dimensions is shown in Fig. 3.1. The x-ray tube is a Varian B180 (Varian Corp., Salt Lake City, UT) with a tungsten anode and an inherent filtration of 1 mm aluminum. It has nominal focal spot sizes of 0.3 and 0.6 mm of which the larger one was used for the measurements. An additional filtration of 0.25 mm ytterbium (Yb) was implemented to take advantage of the k-edge emissions of tungsten (W). The Yb filtration absorbs most photons with energies higher than 59 keV, while allowing transmission of photons of the k-edge emission lines of the tungsten anode. The resulting spectrum, shown in Fig. 3.2, was calculated based on the original x-ray spectra published by the Institute of Physics and Engineering in Medicine [Cra97]. An aperture was fixed in 19.5 cm distance from the focal spot of the source to collimate the beam. The flat-panel detector used in the experimental set-up, a Varian 4030CB (Varian Corp. Salt Lake City, UT), was placed 142 cm away from the focal spot of the source. The detector had 2048×1536 pixels with a pixel size of 195×195 μm^2 and a 0.6 mm thick columnar CsI(Tl) scintillator. As indicated in Fig. 3.1, the plane perpendicular to the detector is defined as the xy-plane and the plane parallel to the detector is denoted as the yz-plane.

A water-filled PMMA-cylinder, with a diameter of 12.7 cm and a height of 20.3 cm, was mounted on a rotational table in 79.5 cm distance from the source. The cylinder had two sets of

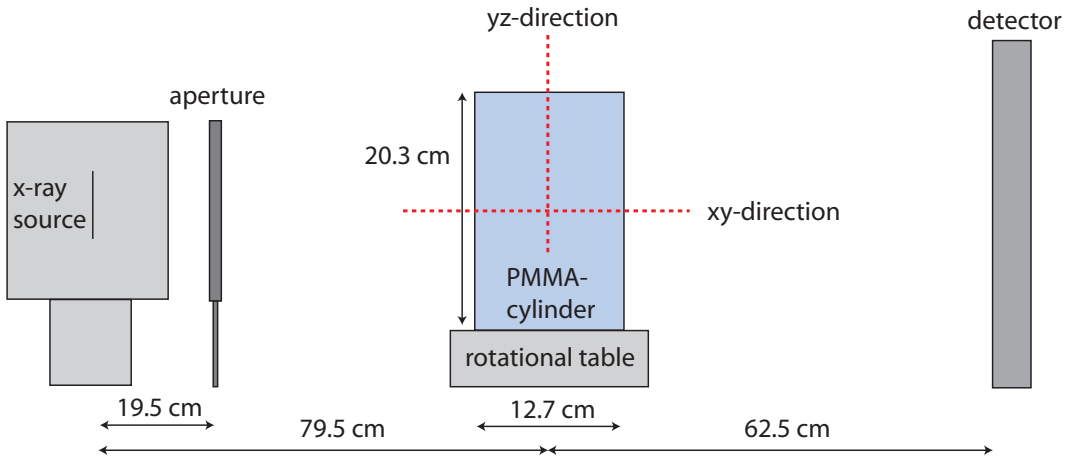

Figure 3.1: *Schematic of the experimental set-up. The red lines indicate the xy- and yz-planes.*

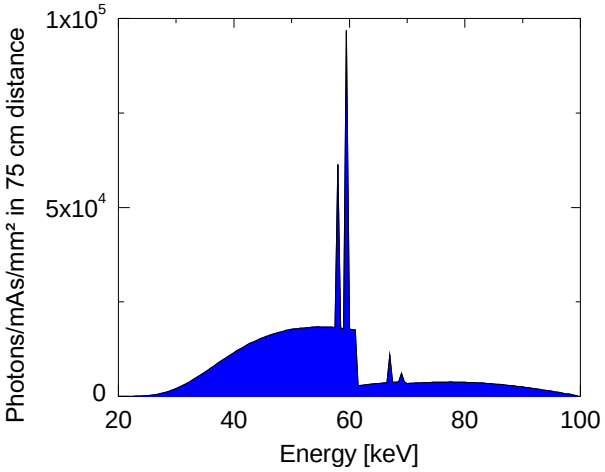

Figure 3.2: *Calculated spectrum filtered with 1.00 mm aluminum and 0.25 mm ytterbium.*

12 equidistant built-in steal ball-bearings forming concentric circles at the top and at the bottom as shown in Fig. 3.3a. The ball-bearings are calibration marks, which allow not only to correct for misalignments but which provide also information in the image about the scanner geometry and acquisition method [Kyp06b].

In order to measure the spatial resolution properties, a "slit" was built consisting of a 0.025 mm molybdenum foil between two pieces of polystyrene as shown in Fig. 3.3b. The polystyrene pieces had a thickness of 2.5 cm and an edge dimension of 4.5×4.5 cm^2. The molybdenum foil was glued to the polystyrene with superglue and directly afterward clenched firmly to create a homogeneous, very thin glue layer. A PMMA stage allowed to place the cube in the center of the water-filled cylinder, but it was not possible to place the cube on the periphery of the cylinder. Hence, only the spatial resolution in the center of the images could be determined.

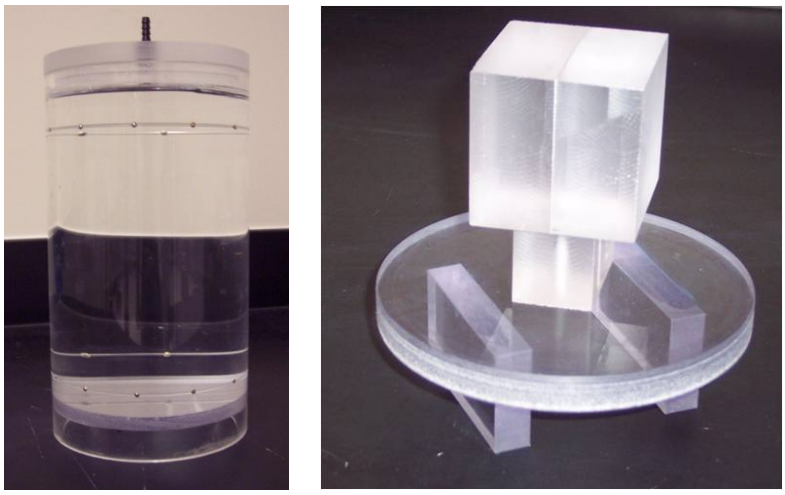

(a) (b)

Figure 3.3: *PMMA-cylinder with built-in steal ball-bearings at the top and at the bottom (a) and the molybdenum "slit" (b).*

The scans were performed with 100 kVp tube voltage, acquiring 360 projection images per rotation. Furthermore, 100 flat-field and 100 dark-field images were taken to perform the flat-field correction of the projected images (described in Sec. 4.1) [Kyp09].

3.2. Clinical CT scanner

The methods developed in this work were tested on a conventional clinical CT before they were applied to CT d'Or. For this purpose, the Siemens Somatom Sensation Cardiac 64 (Siemens Healthcare, Erlangen, Germany) of the Hospital rechts der Isar of the Technical University of Munich was used. An image of the device is shown in Fig. 3.4.

The Somatom Sensation is a third generation 64-slice CT with z-flying spot. The z-flying spot technique uses a periodic motion of the focal spot in the longitudinal direction to double the number of simultaneously acquired slices with the goal of improved longitudinal resolution and elimination of spiral artifacts. The scanner has a focus-isocenter distance of 57.0 cm and a focus-detector distance of 104.0 cm. The x-ray source is a Siemens Straton [ImPACT06], which has a tungsten anode angled at 7° [Kac06]. The ImPACT report dealing with this CT system [ImPACT09] specifies the total filtration on the central axis to be equal to 6.8 mm aluminum. The resulting spectrum, shown in Fig. 3.5, was calculated based on the x-ray spectra published by the Institute of Physics and Engineering in Medicine [Cra97]. Information about whether this already includes the bowtie filter and about the filtration away from the central axis is not publicly available.

The detector array consists of ultra fast ceramic solid state detectors with 672 elements in a row and 40 elements along the z-axis. Depending on the scanning mode, different combina-

Figure 3.4: *Siemens Somatom Sensation Cardiac 64 (picture from official Siemens Clinical website)*

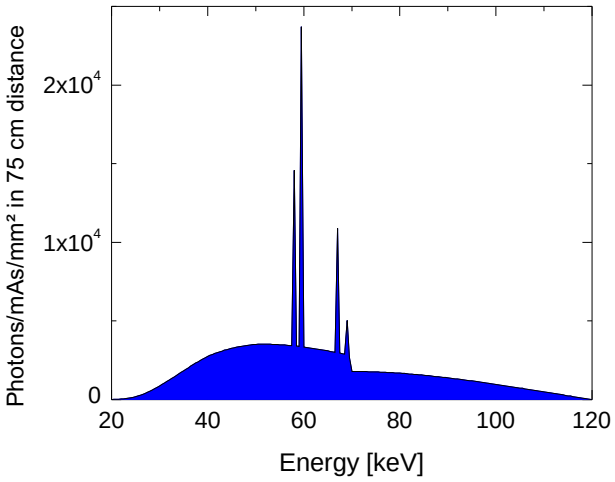

Figure 3.5: *Calculated spectrum on the central axis of the clinical CT scanner for 120 kVp*

tions of source voltage, source current and rotation time are adjustable. The maximal available rotation time is 1.0 s, although 2.0 s can be set for cranial scans. But this only results in 2 scans with a rotation time of 1.0 s each. Further technical details can be found in the corresponding ImPACT reports [ImPACT06, ImPACT09]. Quality assurance of the CT is done regularly by the clinical physicists of the hospital according to DIN EN 61223-2-6 [DIN08]. One phantom used for the analysis of image quality in the Hospital rechts der Isar is the Catphan®phantom (Phantom Laboratory, Salem, NY, USA)[Cat06]. It provides several modules with test devices for high-resolution, low contrast, slice geometry and sensitometry, and a uniform module to measure the noise.

For this work, the spatial resolution was measured using the well-established method [Kwa07, Har10, Wat10] of spanning a wire in air parallel to the rotation axis. In order to approximate a point source, the wire consisted of high-absorbing tungsten and had a diameter of 0.08 mm. 30

images were taken running a sequential abdominal scan for adults with the minimal available slice thickness of 0.6 mm, a rotation time of 1.0 s, a source voltage of 100 kV and a field-of-view (FOV) of 250 mm. The scans were performed with four different mAs-settings, 40 mAs, 150 mAs, 250 mAs and 350 mAs. The images were reconstructed with four different filters: B10s, the smoothest available filter, B30s, the standard reconstruction filter for this scan protocol, B40s, a slightly harder filter also often used in clinical practice and B70s, the hardest available filter.

The noise of the clinical CT scanner was determined using the standard Siemens phantom shown in Fig. 3.6. Its water-equivalent region is a water-filled PMMA cylinder of 20 cm diameter and 3 cm height. To get enough images for a proper analysis, the water region had to be scanned 7 times taking 30 images in each case. Similar to the scans of the wire, a sequential abdominal scan for adults was performed with the minimal available slice thickness of 0.6 mm, a rotation time of 1.0 s, a source voltage of 100 kV and a FOV of 250 mm. The images were reconstructed with the same four different filters as described above.

Figure 3.6: *Standard Siemens phantom. The water region with a diameter of 20 cm and a height of 3 cm is marked by arrows.*

Image quality was analyzed in dependence of the applied dose, which is provided by the system with every image as the weighted computed tomography dose index ($CTDI_W$) [DIN08]. Table 3.1 lists the dose depending on the mAs per scan for the sequential abdominal scan for adults and the above defined parameters. Since the dose is not measured, but calculated by the system based on the calibration, the provided dose is exactly linear to the mAs.

Table 3.1: *$CTDI_W$ for different mAs-setting of the medical CT scanner*

mAs per scan	$CTDI_W$ [mGy]
40	1.68
150	6.29
250	10.47
350	14.66

3.3. C-arm device

Initially, CT d'Or was combined with a C-arm device. Therefore, the Philips MultiDiagnost Eleva Flat Detector (Philips Healthcare, Best, The Netherlands) of the Hospital rechts der Isar of the Technical University of Munich was employed [KCA04]. The system is shown in Fig. 3.7.

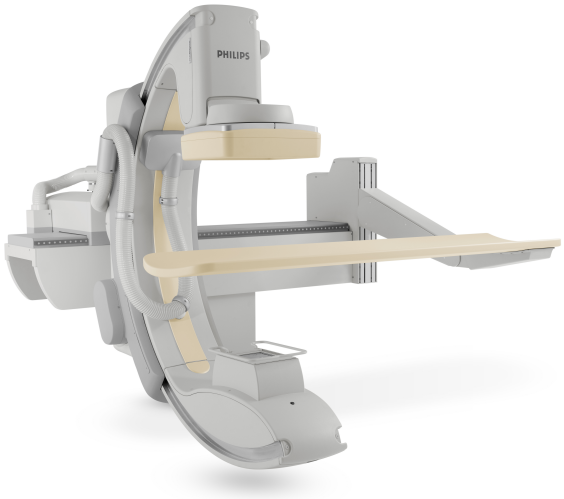

Figure 3.7: *Philips MultiDiagnost Eleva Flat Detector (picture from official Philips website)*

The C-arm device is used in clinical routine as a convenient device to combine diagnosis and interventions on the same system. It has a pulsed source with two available focal spot sizes, 0.6 and 0.8 mm. Since the only reliable information about the filtration is that it is thicker than 2.5 mm aluminum, the expected spectrum could not be calculated. The distance between source and detector can be varied between 95 and 125 cm. The flat-panel detector is a Pixium 4700 (Trixell) with an active area of 381.9×294.1 mm^2, which corresponds to a useful pixel array of 2480×1910 with a pixel size of 154×154 μm^2 [Dan09]. The system creates the images by binning and interpolating over 4.84×4.84 pixels, with an image pixel spacing of 0.746 mm, in order to obtain a 512×512 image (personal communication with a technician from Philips).

3.4. New CT d'Or technology

3.4.1. CT d'Or demonstrator

For this work a "demonstrator" of the CT d'Or geometry was used, which Hugo de las Heras assembled for his PhD thesis [Her08b]. The device is called "demonstrator", because it is only intended to demonstrate the principles of the CT d'Or concept, but not to scan patients. For medical application, the ring would have to be larger with much more detectors with a higher and more homogeneous sensitivity.

CsI(Tl)-scintillator crystals of 1 mm^3 size are covered by a reflecting coating of TiO_2 to improve light capture efficiency. Figure 3.8 shows how the detectors are wrapped in a protective rubber cover and shielded at the back side by 0.5 mm lead. 197 detector elements with a total width of 5 mm are placed regularly at a distance of 25 cm from the center of the device, leaving windows of 3 mm between them.

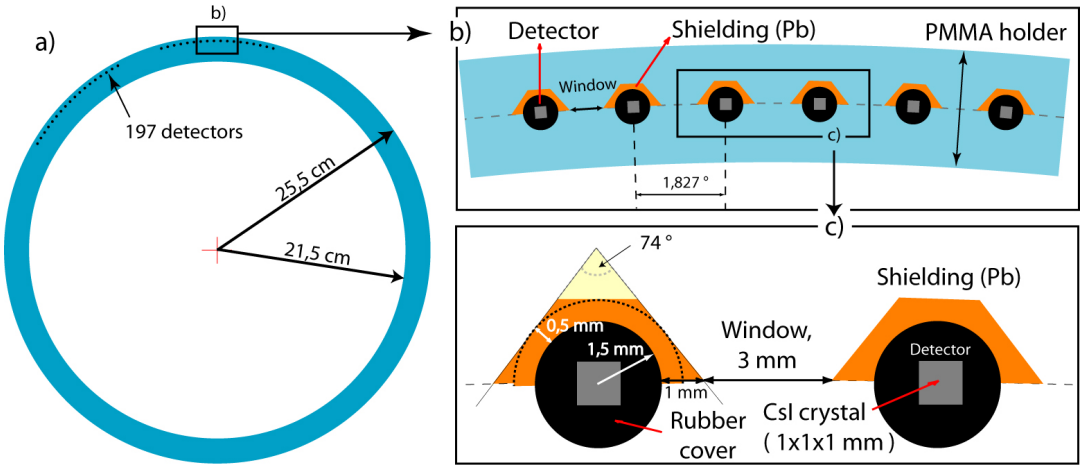

Figure 3.8: *Design of the demonstrator's mask (By courtesy of Hugo de las Heras)*

Optical fibers connect the detectors with photo-diodes, which are very sensitive to external light so that they have to be shielded by additional cases. The software allows data acquisition with sampling times down to 1 ms.

The detector ring is screwed to an aluminum plate to provide mechanical stability and mounted on a rotation desk. This desk is controlled by a software written in LabVIEW 8.2 (National Instruments, Austin, Texas). Probably because of rounding errors in the software, the desk does not respond precisely, so that it rotates somewhat less than 360° when it is ordered to perform a full rotation. Therefore, a scan of 365° was always performed to ensure a complete data set of 360°.

The CT d'Or geometry has the highest efficiency, when shieldings, windows and the effective surface of the detectors have the same size (compare Sec. 2.2). Due to the shape and design of the mask detectors this geometry could not be realized exactly. Figure 3.9 shows which data

are actually collected by the different detector systems. The blue stripes, representing the data collected by the mask detectors, are intermittent by stripes where no data can be collected due to the difference in shielding size and scintillator crystal size. Assuming complete absorption by the lead shieldings, only $\frac{3}{8}$ of the initial photons pass through the windows and only $\frac{1}{3}$ of them actually hits the scintillator. Therefore, only $\frac{1}{8}$ or 12.5 % of the total amount of photons hits the scintillator. In a perfect CT d'Or with shieldings of the same size as the windows and the effective scintillator surface, 50 % of the initial photons would be detected by the mask detectors. This geometry is a major drawback of the demonstrator, but it does not influence its ability to demonstrate the potential of the CT d'Or technology.

The red data of the arc detector in Fig. 3.9 are additionally interrupted by a light green stripe, which connects two mask detectors. These data can obviously not be collected and therefore have to be interpolated. This is inherent to the CT d'Or geometry independent of the special drawbacks of the demonstrator.

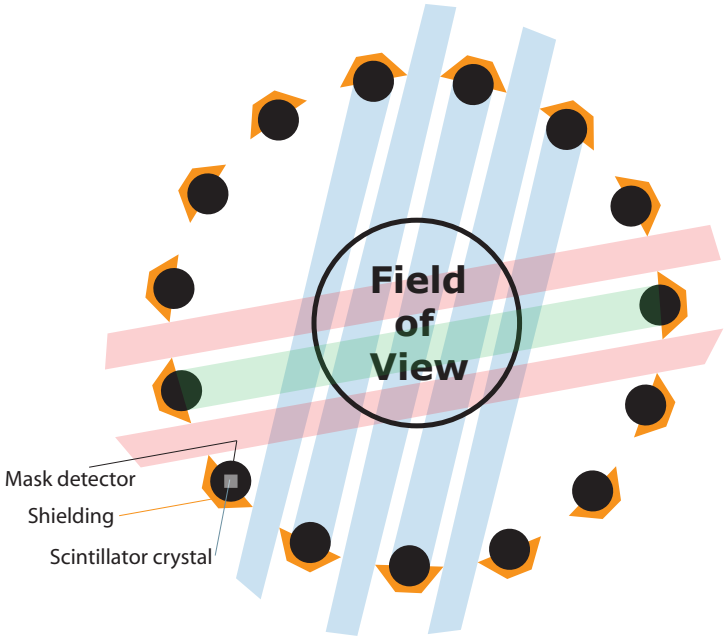

Figure 3.9: *Data collected by the demonstrator of the CT d'Or. The data collected by the mask detectors are blue, the data collected by the arc detectors are red. The white parts between the blue stripes are due to the different size of shieldings and windows. The light green part cannot be detected with CT d'Or in principle. (By courtesy of Hugo de las Heras)*

3.4.2. CT d'Or combined with the C-arm device

The CT d'Or demonstrator in combination with the C-arm device is shown in Fig. (3.10). The source was set to 30 pulses per second for all measurements, which resulted in pulse intervals of 33.3 ms with a pulse width of approximately 5 ms. The sampling time of the mask detectors was set to 20 ms, because this time ensures that only one pulse is scanned in a single sample

as depicted in Fig. 3.11. Separated pulses can easily be added to recover a full pulse and zero samples are deleted. The rotation speed of the desk was set to 2.5° per second. However, since the C-arm device is not constructed with regard to take thousands of images in a short time period, the source would have overheated so that 365°-scans had to be split in 13 series with about 5 minutes cooling time in between. For all scans the source voltage of the C-arm was set to 96 kVp and the source current to 1 mAs. The larger one of the two available focal spot sizes, 0.8 mm, was used, because the resolution of the demonstrator is limited anyhow but the problem with the overheating of the source is smaller. The distance between source and detector was set to 125 cm for all measurements in order to have a reasonable sized FOV to scan the phantom, a slice of an Alderson Rando phantom. It contains real bones and human tissue equivalent material. The chosen slice is at the height of the nostrils so that there are regions of high contrast as well as regions of air. Figure 3.12 shows a picture of this slice and a CT image of it obtained with a slice thickness of 4 mm with the Siemens CT scanner (Sec. 3.2).

The flat panel and the mask had to be aligned so that the central ray of the source, marked in Fig. 3.10 by the dashed line, passed through the isocenter of the CT d'Or ring. Therefore, a 2 cm thick aluminum cylinder was placed in the middle of the ring and a series of images was recorded during a rotation of 180°. If the cylinder did not move between the images for more than the width of one window the alignment was assumed to be correct, because a perfect alignment was virtually impossible with the given experimental set-up.

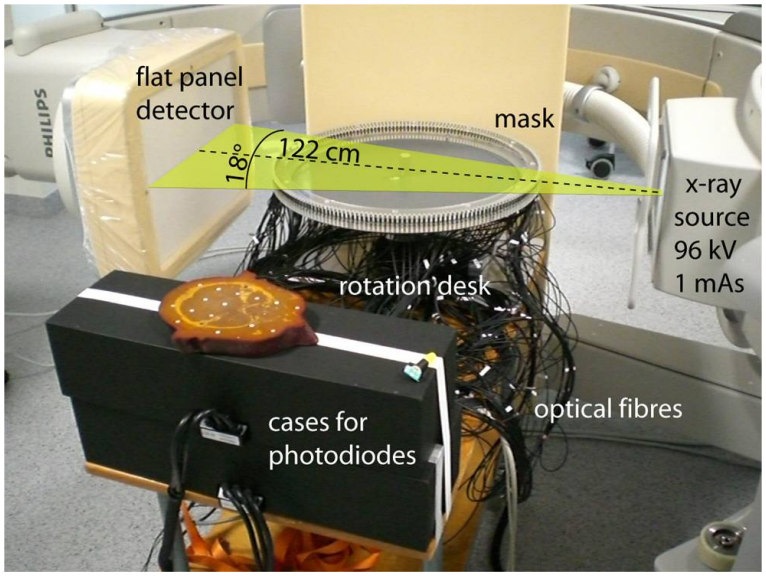

Figure 3.10: *CT d'Or placed between the source and the detector of the C-arm device (By courtesy of Hugo de las Heras)*

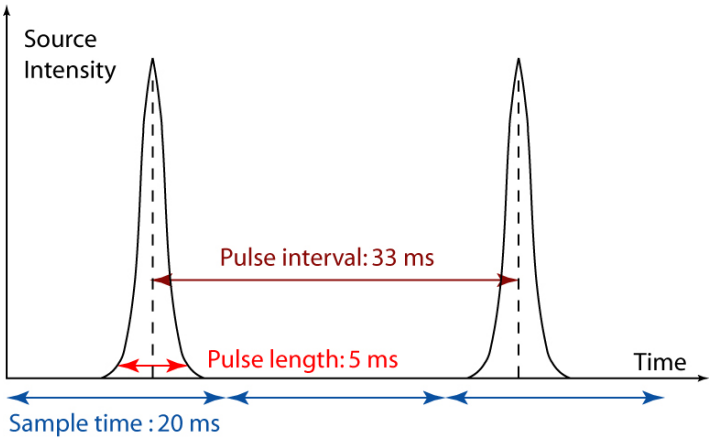

Figure 3.11: *The source pulses had an interval of 33.3 ms with a pulse width of approximately 5 ms (red). By setting the sampling time of the mask detectors to 20 ms (blue), it was ensured that only one pulse was scanned in a single sample. (By courtesy of Hugo de las Heras)*

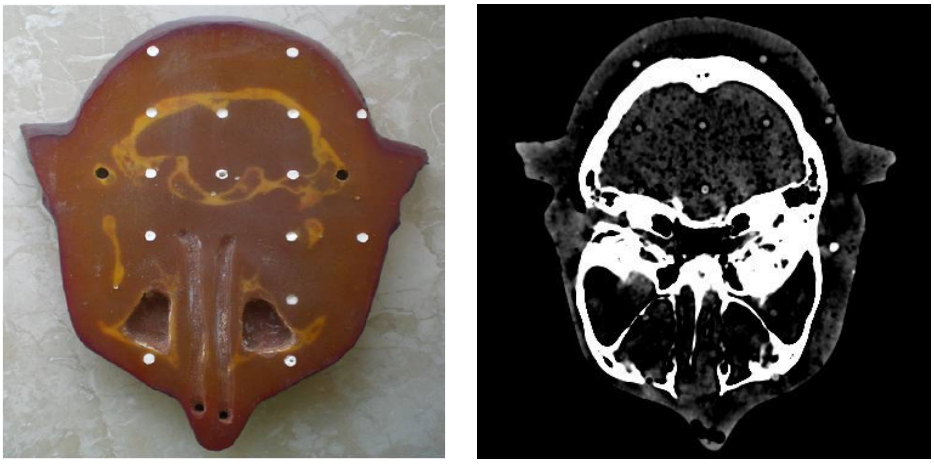

(a) (b)

Figure 3.12: *Photo of the slice of the Alderson Rando phantom used for the measurements (a) and the CT-scan of it obtained with 4 mm slice thickness (b).*

3.4.3. Improved CT d'Or combined with the clinical CT scanner

In the course of this work, the CT d'Or demonstrator was improved in order to position the tilted ring in the gantry of a clinical CT as shown in Fig. 3.13.

For storage, the sensitive CT d'Or ring and the optical fibers are protected by a case with a removable cover plate on the front side. The steal arm, to which the ring is now connected by a joint, can be pulled out. The joint allows to tilt the ring almost exactly around 90°. The height of the arm can be varied to position the ring in the isocenter. Although in a CT the source rotates around the ring, the ring can still be rotated itself in case it is necessary to use it in the C-arm device again. All surfaces are made of stainless steal to guarantee easy cleaning and therefore

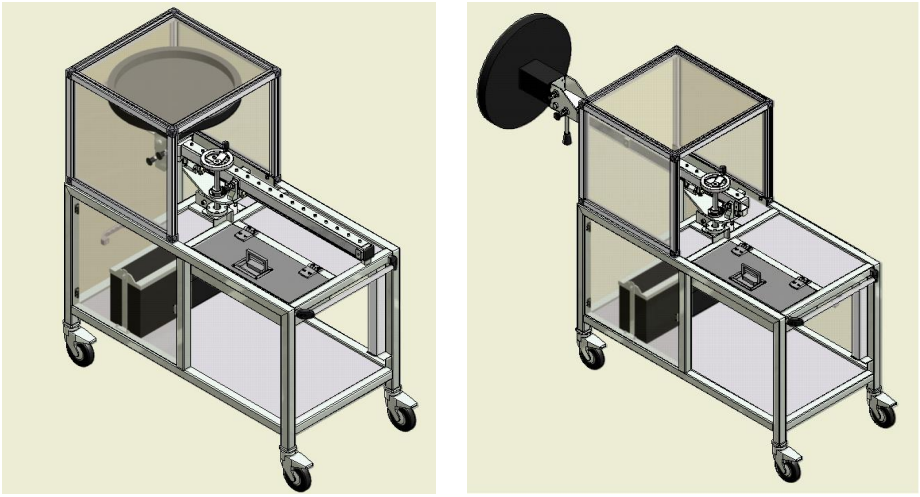

(a) (b)

Figure 3.13: *Scheme of the improved CT d'Or kept for storage (a) and with extended arm for measurement in a CT gantry (b).*

conform to the high sanitary standards in the clinic. The improved CT d'Or combined with the clinical CT is shown in Fig. 3.14.

The center of the CT d'Or ring had to be positioned as accurately as possible in the isocenter of the CT scanner. This position was determined roughly by ensuring that the distance of the ring to the cover of the gantry was the same for all directions. In a next step, CT images were taken with a FOV of 50 cm. Since the radius of the CT d'Or ring is exactly 50 cm, the center of the ring was in the isocenter when all detectors could be seen in the images. With the help of these images, it could also be ensured that the ring was not tilted.

For the measurements with the CT d'Or ring, a head scan protocol and a slice thickness of 18 mm were always used to guarantee that the x-ray cone did not hit the aluminum plate where the detectors of the CT d'Or are mounted.

For the noise measurements a PMMA-disk of 20 cm diameter and 2.5 cm height was used. The spatial resolution properties were measured using a 1.0 mm steel wire.

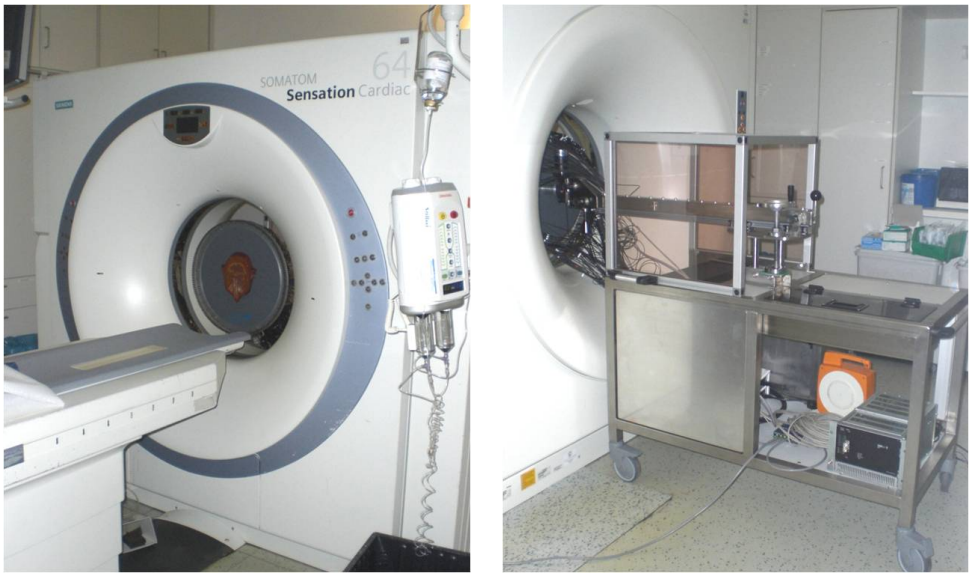

(a) (b)

Figure 3.14: *The CT d'Or ring positioned in the clinical CT from the front (a) and the backside (b).*

4. Data processing

This chapter describes in detail how the measured data for the different CT systems were treated and presents the resulting reconstructed images. For the FDA system, the data processing before and after reconstruction and the steps performed for image analysis are presented in Sec. 4.1. For the clinical CT system, Sec. 4.2 describes the analysis of the reconstructed images and additionally of the raw data in order to get information about the hardware of the scanner. Section 4.3 shows the newly developed data processing method, which considerably improved the image quality for the combination of the CT d'Or with the C-arm device. Its application to the improved CT d'Or demonstrator combined with the clinical CT and the performed image analysis is described in Sec. 4.4.

4.1. FDA laboratory system

With the FDA laboratory system, 360 object images were acquired in one rotation. These images had to be corrected for the image gain, field non-uniformities, the heel effect, and bad pixels and lines [Beu00]. Therefore, 100 flat field and 100 dark field images were taken additionally. Flat field means that the detector was irradiated without an object in the irradiated area, while dark field means that the count rate of the detector was measured without irradiating the detector at all. The average of the dark field images was subtracted from the average of the flat field images and divided by its mean to calculate the image gain. The correction for the image gain and field non-uniformities was done by subtracting the mean dark field from the object images and dividing by the image gain. In order to correct for the heel effect, a plane was fitted to the mean flat field image and the object images were divided by the resulting function. Bad pixels and lines were detected in the mean flat field and corrected in the object images by averaging the neighboring pixels. Finally, the redundant edges of the object images were cut and the pixel values were logarithmized.

The corrected images were calibrated for small misalignments by identifying the location of the steal ball-bearings [Kyp06b] to accommodate the shift-invariant detector point response and the location dependent response of the focal spot. An example for an original (a) and a corrected and calibrated image (b) of the PMMA-cylinder that shows the beads at the top and at the bottom is given in Fig. 4.1.

Images were reconstructed with a pixel cross section of 1436×1436 and a cubic voxel size of 100 μm, using an implementation of the Feldkamp filtered back projection algorithm for flat

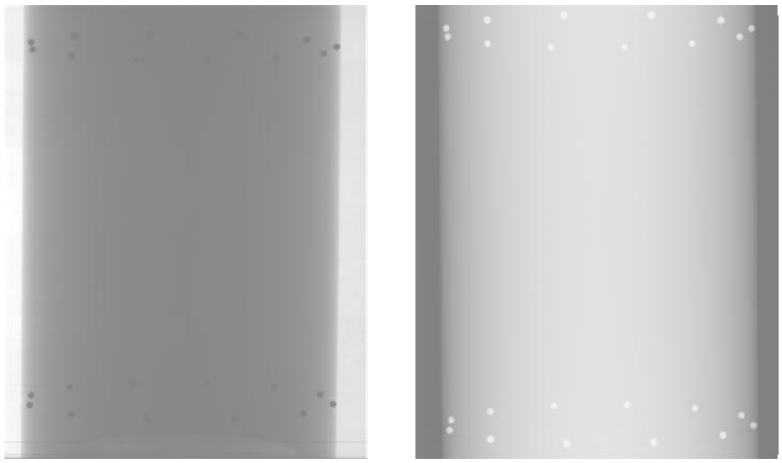

(a) (b)

Figure 4.1: *Original (a) and corrected (b) image of the PMMA-cylinder*

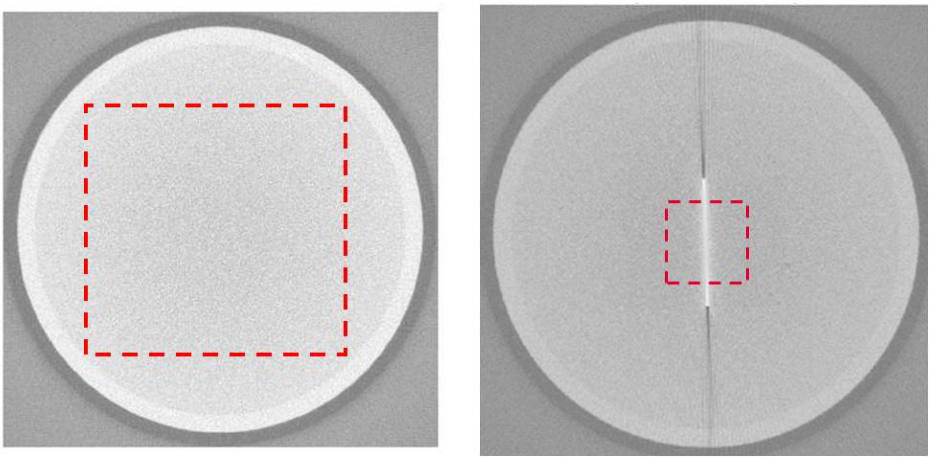

(a) Cylinder with a water region of 877×877 pixels

(b) Molybdenum slit with a rectangular of 381×400 pixels

Figure 4.2: *Examples for reconstructed images*

field detectors [Tur01]. In order to correct for the cupping effect in the xy-plane (perpendicular to the detector) and to convert the pixel values to Hounsfield units, a 2-dimensional second-order polynomial was fitted to the images. The correction was performed by dividing by the fitted polynomial, subtracting one and multiplying by 1000, so that the average value was zero, which corresponds to the Hounsfield unit of water. As illustrated in Fig. 4.2a, a square of 877×877 pixels was cut out of the water-phantom region to analyze the image noise. For the evaluation of the spatial resolution, a rectangular of 381×400 pixels was cut out of the slit images (Fig. 4.2b). The size of the rectangular was chosen taking care to include the tails of the point spread function in one direction, but not the end of the slit in the other direction, where artifacts would have distorted the results.

For the estimation of the spatial resolution, 100 images of the molybdenum slit were reconstructed and corrected as described above. In order to increase the signal to noise ratio, 100 slices were averaged to create the line functions [Kyp08]. The peak of the narrowest line function was fitted with a polynomial, while the tails were fitted with an exponential decay function. The resulting profile was then rotated to generate a 2-dimensional point spread function (PSF) of 300×300 pixels. The 2D PSF was used to calculate the H-matrix with three-fold resolution as described in Sec. 2.3.2.

The MTF was calculated by Fourier transforming the 1-dimensional fitted PSF. In order to obtain a smooth function, a high-order polynomial was fitted to the 1-dimensional MTF, which was then rotated to generate the 2-dimensional MTF.

For the estimation of the noise, the covariance matrix has to be calculated according to its definition from a large set of independent reconstructions. However, for CT this is very time consuming and reduces the life expectancy of the x-ray tube. To overcome these limitations, regions of a single CT volume acquisition were assumed to be independent of each other if they are sufficiently separated to avoid pixel correlations. For typical scanners this distance is supposed to be between four and ten pixels, depending on the type of scanner, the direction (xy or yz) and the reconstruction filter. In order to determine the necessary pixel distance for this scanner, the axis profiles of the central row of the covariance matrix were analyzed to obtain the autocovariance. Due to the anti-correlated nature of noise in images reconstructed with the FBP algorithm, the ROI spacing was selected to be equal to the pixel distance at which the absolute value of the autocovariance function had dropped to 1 % of its maximum. For this system and the applied reconstruction filter, the pixel distance turned out to be four. The water region of each of the 200 images was subdivided into 32×32 pixel ROIs, resulting in a covariance matrix of 1024×1024 pixels. Its eigenvectors were repartitioned into 32×32 pixel arrays, in order to visualize the structure of the noise.

For the calculation of the NPS, the reconstructed images were subdivided in ROIs in the same way as described above for the covariance matrix. The 32×32 pixel ROIs were Fourier transformed and averaged to obtain the 2-dimensional NPS. The 1-dimensional NPS, which provides information about the frequency distribution, was obtained by averaging radially.

Although using ROIs from the CT volume is a convenient method, one has to be aware that it disregards that the noise in the center of an image is different from the noise in the outer regions. Therefore, in addition to evaluating the whole cylinder area for noise, the xy-plane slices were divided into nine square regions and treated separately as described above. The number of submatrices available for the calculation of the covariance matrix decreased to 12800 so that the respective covariance matrices were not described as accurately as for the whole image.

The spatial resolution and the system noise were used to calculate the SNR for two simulated input signals: a disk with a uniform magnitude of 20 HU placed inside a uniform background of -30 HU and a torus of uniform magnitude of -30 HU placed inside a uniform background of 20 HU. The disk models a dense mass inside a lower density region, while the torus models a

dense mass with a fatty margin inside a high density region. The radius of the disk was 0.85 mm, the outer radius of the torus was 1.1 mm and the inner radius was 0.7 mm. These values were chosen to generate two objects with the same area so that their SNRs were directly comparable. Furthermore, the difference of 0.4 mm between inner and outer radius is typical for a fatty ring outside a dense tumor.

In order to check whether the number of ROIs, obtained from the whole images as well as from the 9 regions, was enough to properly define the 1024×1024 matrix, a bootstrapping calculation was performed [Efr79]. For this modern, but computer-intense approach, new covariance matrices were calculated from ROI samples of size n $<$ *Number of available ROIs*, each of which is obtained by random sampling with replacement from all available ROIs. Since the covariance matrix can hardly be defined by only one value such as the mean value or the standard deviation, the new covariance matrices were used to calculate the corresponding image-space SNR and its standard deviation. For each n ($n = 2 \cdot 10^3, 5 \cdot 10^3, 1 \cdot 10^4, 1.5 \cdot 10^4, 5 \cdot 10^4$ and $1 \cdot 10^5$), 10 runs were performed respectively with the disk as input signal and the noise images taken at 9.8 mGy.

4.2. Clinical CT scanner

4.2.1. Analysis of the raw data

The raw data are rarely analyzed, because the data can be exported, but no program is available to read them. Therefore, the first step was to write a program which converted the raw data in a readable format. From a cooperation of the Hospital rechts der Isar with Siemens, information was available about how the files are organized; for example, the length of the main header and the frame headers, the number of detectors per row or the number of views per rotation were known. Since the structure of the raw data is part of the cooperate secret, details cannot be presented here. Using this information and a conventional hex-editor allowed to read the raw data, the individual frames and the header information. The exported data are preprocessed by scaling the logarithmic attenuation values

$$Data = -c \log \frac{I}{I_0} \tag{4.1}$$

where c is a constant, I_0 is the primary intensity, and I is the attenuated intensity.

Spatial resolution

In CT, the standard phantom for measuring the MTF is a wire or a bead. Therefore, a tungsten wire in air was used for the measurements of the spatial resolution. The wire had a diameter of 0.08 mm and was spanned through the gantry parallel to the rotation axis. This is a well-established method [Kwa07, Har10, Wat10], which allows not only to derive the MTF from the raw data, but also from the reconstructed images.

With regard to the CT d'Or geometry that can currently scan only one slice per rotation, the method for analyzing the raw data was developed to be independent of the number of rows of the detector. Therefore, the sinogram of the raw data was used, which is composed of the central row of each frame, independent of the total number of rows. An exemplary sinogram of the tungsten wire at a distance of about 4 cm from the isocenter of the CT is shown in Fig. 4.3. The sinogram was created running a sequential head routine with a source voltage of 120 kVp, a source current of 300 mAs, a rotation time of 1.0 s and a slice thickness of 1.2 mm. The amplitude of the curve and respectively the number of pixels n shadowed by the wire depends on the wire - isocenter distance: The shorter the distance, the lower is the amplitude. When the wire is positioned exactly in the isocenter, the curve becomes a straight line.

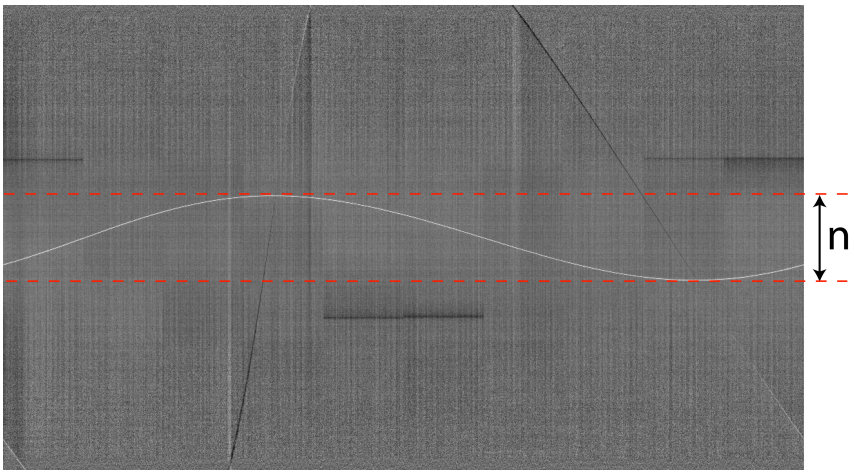

Figure 4.3: *Sinogram of the wire at a distance of about 4 cm from the isocenter. The columns correspond to different views while the rows correspond to different detector pixels. The red, dashed line indicates the number of detector pixels n which are shadowed by the wire in a complete rotation.*

The dark, vertical stripes are artifacts, probably due to dirt (i.e., contrast agent) on the gantry surface during the calibration. During the measurement the gantry was clean, because there are no light artifacts in the sinogram that would be produced by objects in the beam due to the preprocessing of the raw data. The diagonal lines originate from a small slit in the cover sheet of the gantry. The first, steeper one, is produced when the source passes the slit, the second, flatter one, is produced when the detector passes the slit, because the detector is larger and therefore needs more views to pass. However, both types of artifacts do not considerably distort the calculation of the MTF, because they are very faint in the area of the wire.

Fujita et al. [Fuj92] first measured the oversampled MTF in 2-dimensional radiography using a slanted lead slit. Since a wire is nothing but a "negative slit", a similar method was chosen in this work. However, several steps are necessary to convert the curved sinogram of the wire into a data set suitable for this method. Using the parameters in Tab. 4.1, the calculation of the MTF was performed in the following steps:

Table 4.1: *Parameters of the geometry*

Parameter	Abbreviation	Dimension
Distance source - detector	a	104 cm
Distance source - isocenter	b	57 cm
Detector pixel size	s	1.41 mm
Number of detector pixels in a row	N_{pix}	672
Number of views	N_{views}	1160
Diameter of the wire	w	0.08 mm

1. The position of the wire was determined in every row.

2. The number of detector pixels n that are shadowed by the wire in a complete rotation was evaluated (Fig. 4.3).

3. The distance of the wire from the isocenter was calculated with the coordinates defined in Fig. 4.4. The maximum arc length $l_{\max}$ was determined from the number of shadowed pixels n of size s

$$l_{\max} = \frac{n \cdot s}{2} \tag{4.2}$$

The factor 2 is necessary, because only half of the arc is needed for the further calculations. By using the source - detector distance a, the maximum angle $\alpha_{\max}$ in radian was calculated with

$$\alpha_{\max} = \frac{l_{\max}}{a}. \tag{4.3}$$

The distance r of the wire to the isocenter is then

$$r = b \cdot \sin \alpha_{\max}. \tag{4.4}$$

4. The heel-effect was corrected by fitting a second order polynomial to every row and subtracting the fitted curve from this row.

5. The slightly slanted alignment of the wire was corrected by determining the angle β of the wire in each frame. Since the area covered by the tilted wire is about $\arccos \beta$ larger, the value of the pixel mapping the wire position in the corresponding row of the sinogram is multiplied with $\cos \beta$.

6. The changing distance between the wire and the detector, which causes projections of different size, was corrected using the parameters defined in Fig. 4.5. Chord c in every point of the rotation is defined from the position j of the wire in every row

$$c(j) = 2 \cdot a \cdot \sin\left(\frac{(|j - \frac{N_{\text{pix}}}{2}| - 0.5) \cdot s}{10 \cdot a}\right). \tag{4.5}$$

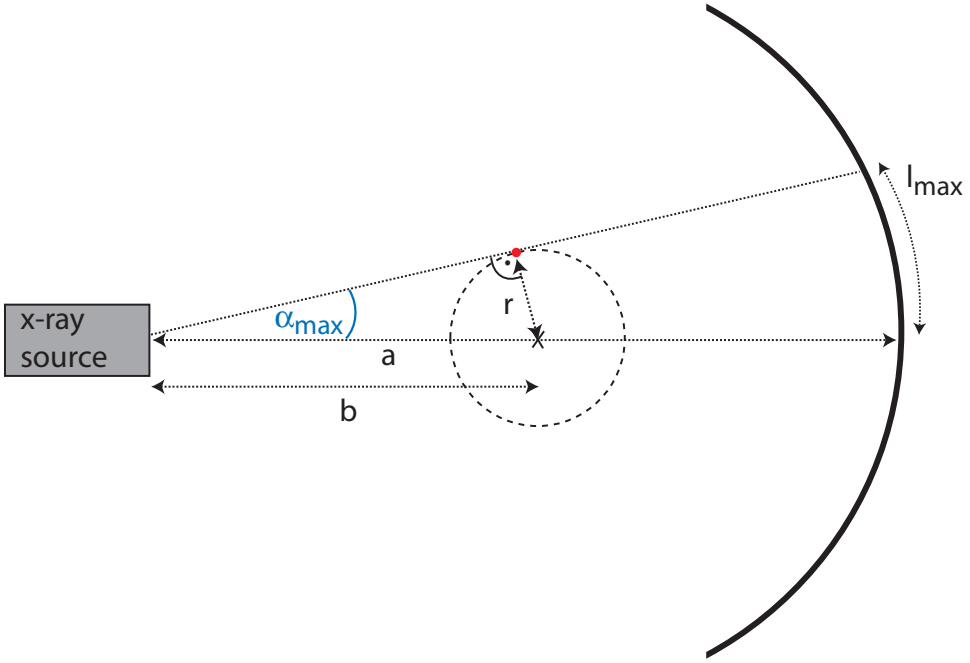

Figure 4.4: *Coordinates used to calculate the distance wire - isocenter distance*

$\alpha(j)$ is then given by

$$\sin\alpha(j) = \frac{\frac{c(j)}{2}}{a} \qquad \longrightarrow \qquad \alpha(j) = \arcsin\left(\frac{c(j)}{2\cdot a}\right). \tag{4.6}$$

For every j there are two possible positions of the wire

$$\begin{aligned} \gamma_1(j) &= \arcsin\left(\frac{c(j)\cdot b}{2\cdot a\cdot r}\right) \\ \gamma_2(j) &= \pi - \arcsin\left(\frac{c(j)\cdot b}{2\cdot a\cdot r}\right) \end{aligned} \tag{4.7}$$

The distance x between source and wire therefore can also have two values

$$\begin{aligned} x_1(j) &= \frac{b\cdot\sin\gamma_1(j)}{\sin(\pi-\alpha(j)-\gamma_1(j))} \\ x_2(j) &= \frac{b\cdot\sin\gamma_2(j)}{\sin(\pi-\alpha(j)-\gamma_2(j))} \end{aligned} \tag{4.8}$$

The wire amplitude of each view is multiplied with one of the correction factors $k_{1,2}$

$$k_{1,2}(j) = \frac{x_{1,2}(j)}{b}. \tag{4.9}$$

depending on whether the wire is closer to the source or to the detector. This information is given by the first derivative of the curve that defines the position of the wire for each view. If the derivative is negative, the wire is on the side of the source and k_1 is applied; if the derivative is positive, the wire is on the side of the detector and k_2 is applied.

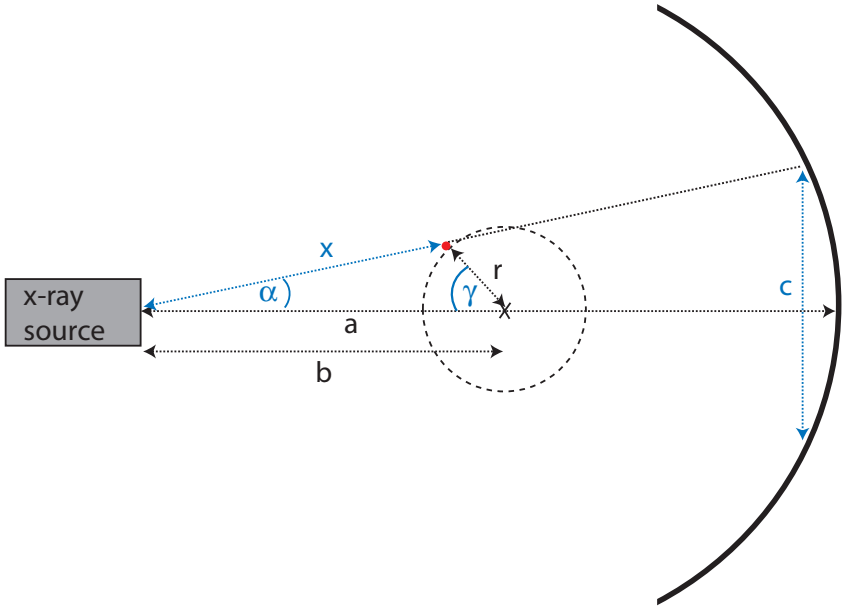

Figure 4.5: *Coordinates used to calculate the distance between source and wire*

7. Each row was shifted so that all pixels mapping the wire positions are on the central detector pixel.

8. The rows were sorted by the values of their maxima. The sum of the central pixel value plus either the right neighboring pixel or the left neighboring pixel gives the tendency of the wire position. The row with the highest maximum is positioned in the center and the maximum values decrease to both sides, where the rows below the center have a tendency to the left while the rows above the center have a tendency to the right. This way, a wire is created which enters the central pixel on the first row and leaves it on the last row. The resulting sinogram after shifting, correcting and resorting the data is shown in Fig. 4.6.

9. The oversampled line spread function (LSF) was created by reforming the array in a 1-dimensional vector adding one column on the end of the next one [Fuj92, Buh03]. The resulting LSF (Fig. 4.7) is therefore $N_{\text{pix}} \cdot N_{\text{views}} = 779520$ pixels long.

10. The MTF was calculated by taking the absolute value of the Fourier transformed LSF. In order to emphasize the trend of the curves and to minimize the fluctuations produced by high noise, the MTF was smoothed with the adjacent average over 9 points.

11. The corresponding spatial frequency u was calculated. The maximum frequency is given by the Nyquist frequency of
$$\frac{1}{2 \cdot s} = 0.355 \frac{1}{\text{mm}} \tag{4.10}$$

12. The spatial frequency was corrected for the edge obliquity by
$$u_{\text{corr}} = \frac{u}{\cos\left(\frac{\pi}{2} - \arctan N_{\text{views}}\right)}. \tag{4.11}$$

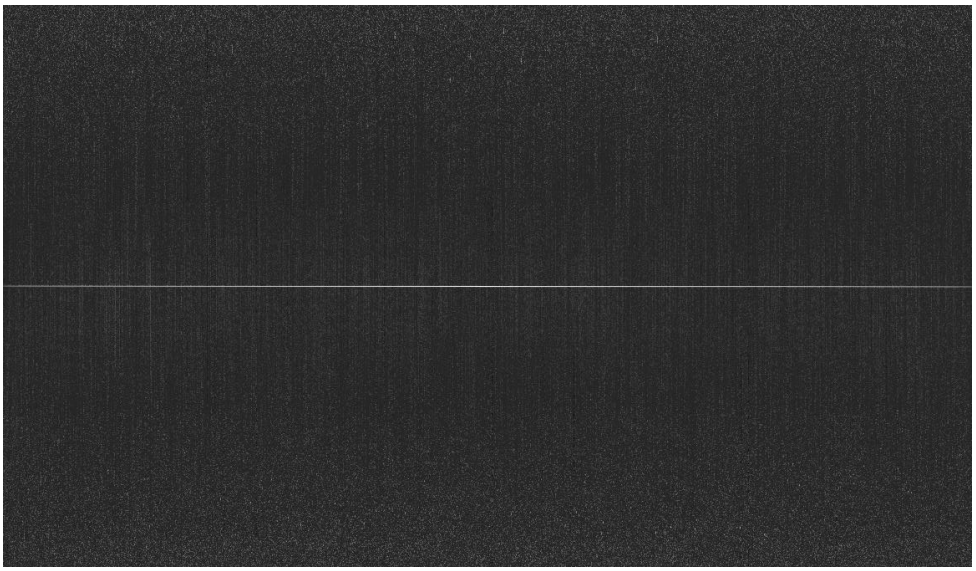

Figure 4.6: *Sinogram after shifting, correcting and resorting the data. Again, the columns correspond to different views while the rows correspond to different detector pixels.*

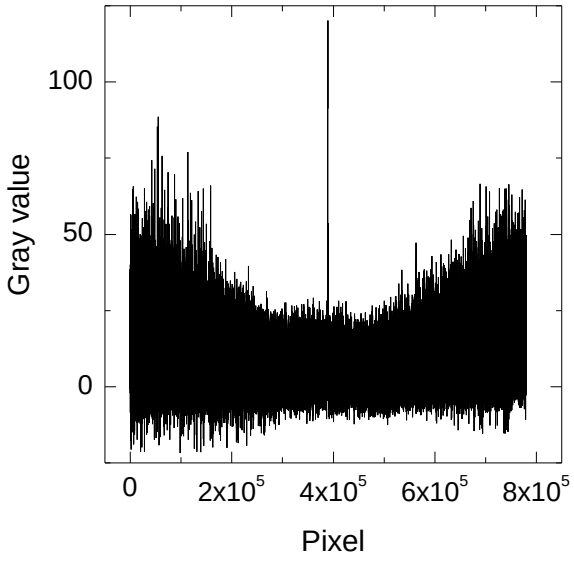

Figure 4.7: *LSF sampled from the sinogram*

13. The MTF was corrected for the finite width w of the wire by dividing by the sinc function

$$k_{\text{wire}} = \frac{\sin(\pi \cdot w \cdot u_{\text{corr}})}{\pi \cdot w \cdot u_{\text{corr}}}. \tag{4.12}$$

14. Values smaller than 0.05 $\frac{1}{\text{mm}}$ were cut off, because high noise on the raw data led to large fluctuations of the MTF in the range from 0 to 0.05 $\frac{1}{\text{mm}}$. For the NPS it is common practice not to start the presentation of the values at 0 $\frac{1}{\text{mm}}$ [Han79], but for the MTF this has been done too [Wag79].

15. The MTF was normalizing to 1 at 0.05 $\frac{1}{\text{mm}}$.

Noise

In projection radiography, the conventional method to calculate the NPS uses 2-dimensional ROIs. The method developed in this work includes as much slices as available and averages them. With regard to its application to the CT d'Or technology in the future, the method is still independent of the actual number of slices. The calculations were performed in the following steps:

1. Trend correction was performed by fitting a second order polynomial to each detector row of every frame and subtracting the fitted curve from this row.
2. A $256 \times N_{\text{slices}}$ pixel ROI was taken from the middle of every row. 256 pixels are sufficient to cover also long-range correlations according to the international IEC standard [IEC03].
3. The Fourier transformed was calculated of each ROI of every frame.
4. All rows of a ROI were averaged to produce the 1-dimensional NPS according to a method developed by Padgett et al. [Pad05].
5. The corresponding spatial frequency was calculated.
6. The high fluctuations in the range from 0 to 0.05 $\frac{1}{\text{mm}}$ were removed.

4.2.2. Analysis of the reconstructed images

Images of the clinical CT scanner were reconstructed with various reconstruction filters:

- B10s: the smoothest available filter
- B30s: the standard filter for the scan protocol abdomen
- B40s: another frequently used filter
- B70s: the sharpest available filter

Since the CT scanner is calibrated for the water phantom, no corrections for the cupping effect had to be applied. But since the CT device saves the pixel values in Hounsfield units plus 1024 to optimize the data storage, this value had to be subtracted from the pixel values.

The slightly tilted tungsten wire allows to generate the oversampled point spread function (PSF) according to Kwan et al. [Kwa07] by using all 30 acquired slices. Therefore, a small region of interest (ROI) of 17×33 pixels around the wire was cut out of every image. The center of mass along the x-axis (CM_x) for each point spread function (PSF) was then computed as

$$CM_x = \frac{\sum_x \sum_y \text{ROI}(x,y) \cdot x}{\sum_x \sum_y \text{ROI}(x,y)}, \tag{4.13}$$

where x and y define the spatial location of the pixel in the ROI. The CM_x values for all 30 images were plotted as a function of the slice number. A linear function was fitted to the data to define the centers of the PSF along the CT slices. The PSF of each slice was generated by integrating over the 17 rows of the corresponding ROI. Each PSF was then shifted by the fitted position of the center of mass. Assembling the PSFs of every slice yielded the oversampled PSF. By analogy with the FDA system, its peak was fitted with a polynomial, while the tails were fitted with an exponential decay function. The resulting, smoothed PSF was rotated to generate a 2-dimensional PSF, which was used to calculate the H-matrix with three-fold higher resolution. The MTF was calculated from the 1-dimensional, fitted PSF by Fourier transformation.

For the estimation of the noise, 210 slices of the water phantom were taken, which provided a maximal water region of 266×266 pixels. This array was again subdivided into 32×32 pixel ROIs that had to be separated by several pixels to approximate independent data sets. Therefore, the autocovariance function was calculated for each reconstruction filter (Fig. 4.8). The ROI spacing was chose to be the pixel distance at which the absolute value of the autocovariance function had dropped to 1 % of its maximum. As expected, the smoothest filter had the longest ranging covariance of up to 8 pixels. This value was henceforward used as spacing between the ROIs for the images of all filters to make sure that always the same number of ROIs was employed for the calculation of the covariance matrix.

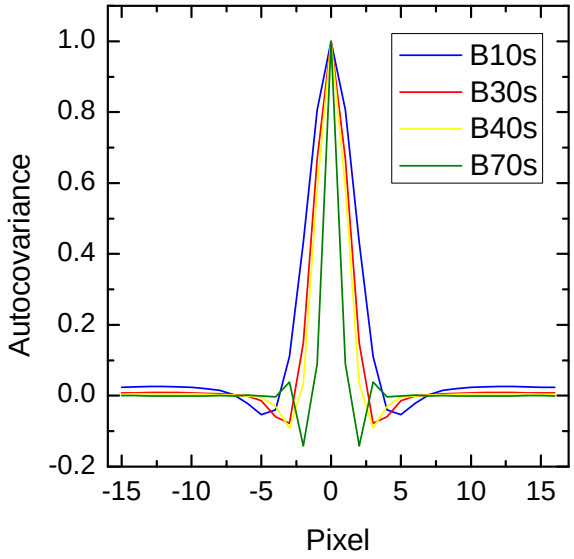

Figure 4.8: *Autocovariance function for the different reconstruction kernels*

For calculating the NPS, the same ROIs were Fourier-transformed and averaged to get the 2-dimensional NPS. The 1-dimensional NPS was again created by radially averaging.

The SNR for both approaches was calculated according to Sec. 2.3 using a simulated disk with an amplitude of 50 HU and a diameter of 2 mm.

Dividing the 266×266 pixel water region in 32×32 ROIs with a spacing of 8 pixels results in 7560 ROIs for the whole images and only 840 ROIs for each of the 9 square regions. A

bootstrapping calculation was performed to estimate the error introduced by using substantially less ROIs than for the laboratory CT system. The image-space SNR and its standard deviation for 10 runs was calculated from subsamples of size n = 1500, 2500, 5000 and 7500 for noise images taken at 10.47 mGy and reconstructed with B30s.

4.3. CT d'Or combined with the C-arm device

The existing programs for the reconstruction of images taken with the CT d'Or demonstrator in combination with the C-arm device had to be adapted to each data set individually. Since this is a very time consuming process and the results depend strongly on the skills and patience of the performer, completely new programs were written for the image reconstruction[1]. The data are now sampled automatically for each data set based on the geometry of the set-up. For the development of the improved algorithms, a data set produced by Hugo de las Heras for his PhD thesis was used. This data set was gained by a scan of the Alderson Rando phantom at a source voltage of 96 kVp and a source current of 1.0 mAs per image. The subsequent comparison between the images generated with the old and the new software is going to demonstrate that the image quality could be improved considerably.

Data of C-arm device

The C-arm device provides more than 4000 images of the CT d'Or ring in one rotation. In order to get the raw data necessary for image reconstruction, a line in the middle of the detector row of the CT d'Or is cut out of every image as shown in Fig. 4.9a. An example for a part of such a raw data set acquired using an Alderson Rando phantom is presented in Fig. 4.9b. Each rhomb corresponds to one data point of the fan data matrix and therefore has to be integrated. The location of the rhombs is determined automatically based on the mathematics in Sec. A.1.1.

For this algorithm, the geometry of the set-up has to be known exactly. In the actual measurement set-up, three parameters could however not be determined with a sufficient accuracy: the starting position relative to the ring, the source-to-isocenter distance of the CT d'Or and the angle between the central ray of the fan and the ray which passes through the isocenter of the CT d'Or. The program calculated the expected location of the data for all possible combinations of these three values and compared the result to the measured data set. The parameter combination with the highest agreement with the data was then used to create a so-called mask. This is an array of the same size as the input data set, where relevant pixels are indicated by 1, while other pixels are 0. The fan data were sampled at the positions defined by the mask.

In a next step, the fan data matrix was converted into the sinogram. Since the detected signal is theoretically the same (ignoring scatter radiation and beam hardening) for rays passing the

[1] The programs were developed together with Dr. Oleg Tischenko from the Department of Radiation Physics and Diagnostics of the Helmholtz Zentrum München.

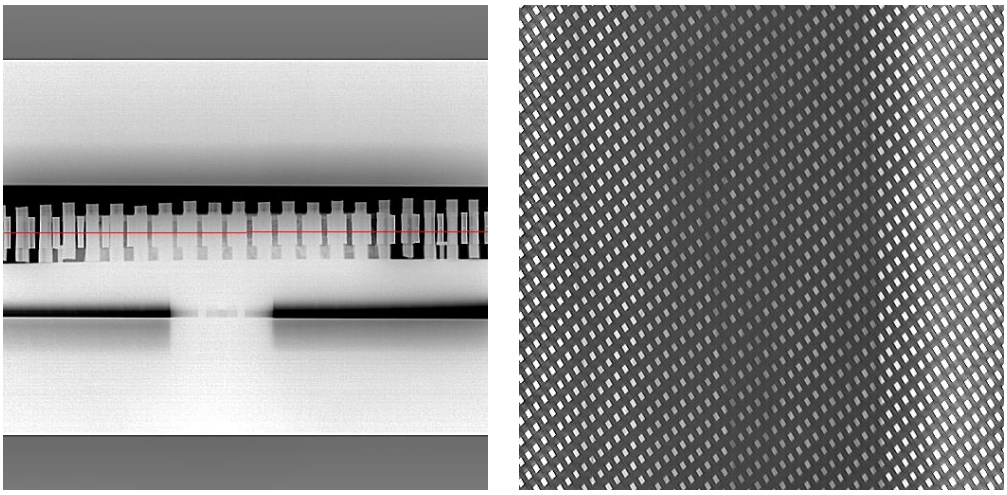

(a) (b)

Figure 4.9: *Image of the C-arm device acquired using an Alderson Rando phantom (a). The red line indicates the line cut out to get the raw data. An extraction of the corresponding raw data set (b).*

windows from one side and those passing 180° from the other side, these data were averaged to decrease the noise. The data were logarithmized according to

$$D_{\text{logged}} = -\log \frac{D_{\text{averaged}}}{\max(D_{\text{averaged}})}. \tag{4.14}$$

For the data set of the C-arm device, only the rays passing through two windows of the CT d'Or ring can be recorded. The rays which pass theoretically from detector to detector are also required for the reconstruction and therefore have to be interpolated. In the past, an interpolation with 1-D splines was used, but for this work, several different methods were tested:

- Averaging over the four adjacent pixels on the corners of the missing one.
- Interpolating using all existing data by weighting each pixel with a sinc function $\frac{\sin x}{x}$, where x is the distance of the pixel to the interpolated one.
- Interpolating with 1-D splines.
- Interpolating by weighting with the sinc^2 function.

For the reconstruction of images of the Alderson Rando phantom, the interpolation with the sinc^2 function turned out to result in the best image.

The last step was to reorder the fan data matrix into fan-parallel data and perform the reconstruction using OPED. A comparison between images reconstructed from the same raw data set with the old (a) and the new software (b) is shown in Fig. 4.10. The new image is noticeably sharper and shows more details than the old one. For example, the internal occipital protuberance (red ring) is clearly visible in the image reconstructed with the new method, while it is

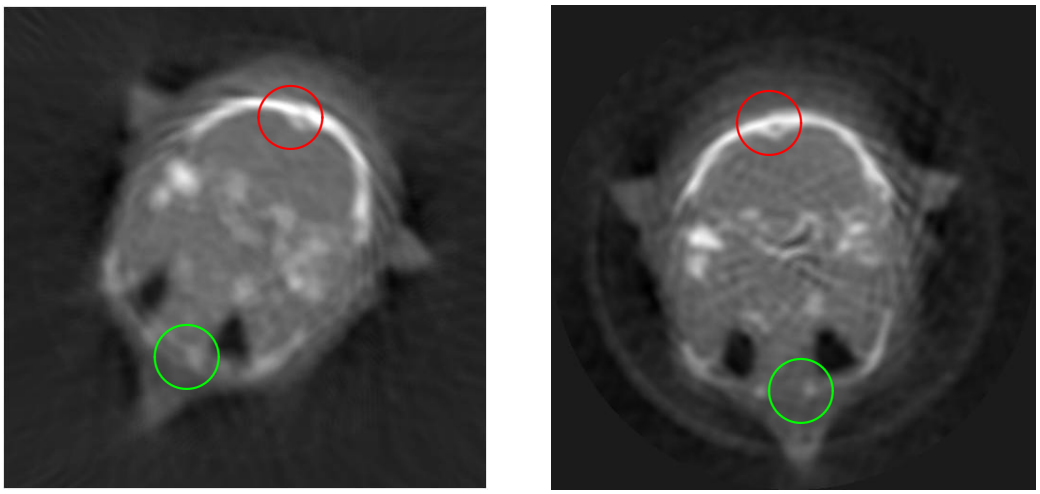

(a) (b)

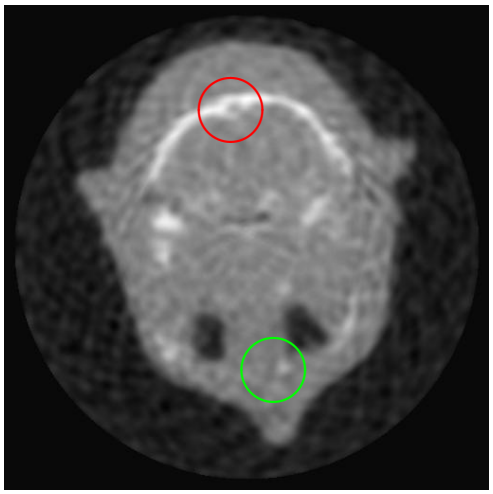

(c)

Figure 4.10: *Comparison of the images of the C-arm device reconstructed with the old software (a), the new software for the C-arm device (b) and the further improved software for the CT scanner (c).*

blurred in the old image. The same holds for the small bones in front of the sinuses maxillaris (green ring). The basilar part of the occipital bone in the center region of the skull looks also sharper in the new image, but it is difficult to decide whether this is really due to a higher image quality or only a result of the severe artifacts, which still decrease the image quality considerably. However, the streak artifacts and the ring around the phantom are supposed to vanish when the data set is combined with the data of the mask detectors.

Data of mask detector

Besides the described problems with the geometrical uncertainties, the mask data have the additional difficulty that they are obtained in 13 series: 12 series over 30° and 1 series over 5°, in

order to correct for the inaccuracy of the rotation table. Figure 4.11a shows an exemplary raw data set for an empty scan over 30°. The columns correspond to the 197 mask detectors and the rows correspond to the views. The broader stripe are the usable data measured by detectors irradiated from the front. The slimmer stripe corresponds to detectors which were irradiated from the back side through the shieldings while they were directly in front of the source. Each data set starts and ends with views during which neither the source was running nor the table was rotating. Then the source started, but the table was not yet moving, thereby producing a vertical pattern in the data. Only the views which have a slanted pattern are usable for the reconstruction, because there the table was rotating. Since a reliable algorithm to automatize the selection of the data sets could not be realized, it still had to be done manually, although this is a time-consuming and error-prone procedure.

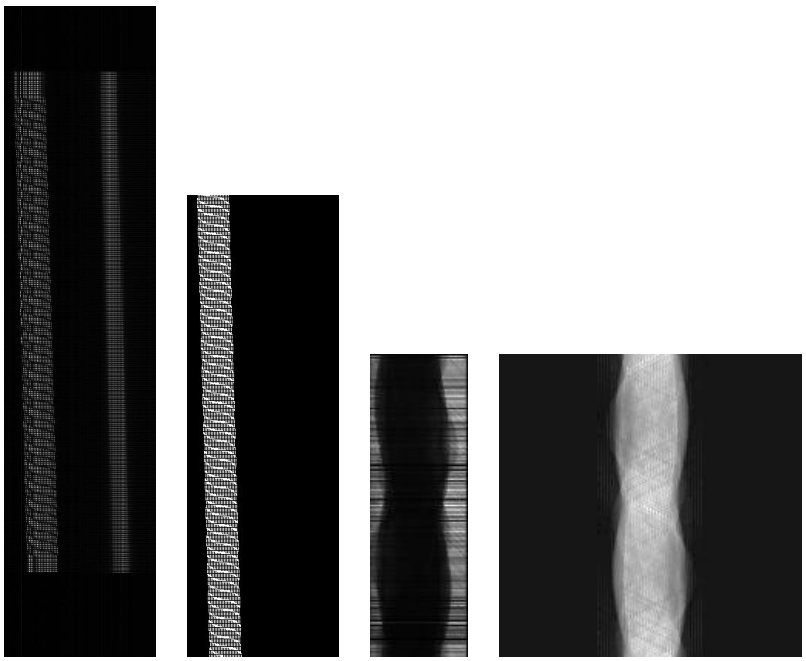

Figure 4.11: *Raw data of the CT d'Or in the C-arm device (a), the corresponding mask (b), the fan data set (c), and the resulting sinogram (d). Please note that for better visualization the raw data set shows an empty scan, while the fan data and the sinogram correspond to a scan of the phantom.*

In these selected data, the positions of the relevant data points were defined with the mathematics presented in Sec. A.1.2. By reconstructing the data of the C-arm, the exact position of the CT d'Or relative to the source was obtained. But still there were three unknown parameters left: the relative position of the first detector to the source, the coordinate on the ring and the time lag between source pulse and detector readout. For all possible combinations of these three values, the expected location of the data was again calculated and compared to the measured data set. Since the three parameters are different for each of the 13 data sets, this fitting had to

be done for each data set individually. Therefore, 13 different masks were generated of which one is shown in Fig. 4.11b. In order to create the complete fan data set, 12 of the fan data sets sampled on the defined positions had to be added. The 13^{th} fan data set was only needed partly to complete the 360° rotation. Figure 4.11c presents the resulting fan data set of the scan of the Alderson Rando phantom. It reveals that the rows corresponding to different detectors have largely varying values. By normalizing each row to the same mean value, this drawback could be widely overcome. About 10 lines had to be set to 0 and interpolated by cubic splines, because they belonged to broken detectors. The sinogram (Fig. 4.11d) was produced by reordering the corrected fan data to fan-parallel data and logarithmizing them.

The images were reconstructed with OPED. Figure 4.12 shows the comparison between an image reconstructed with the old software (a) and with the new software (b). Both images have about the same sharpness, but the old image has a higher contrast between skull and air regions than the new one. However, the old image has an artificial ring around the phantom, which does not appear in the new one. The streak artifacts on the edge of the skull (red circle) are also fainter in the new image than in the old one.

Combination of both data sets

For the reconstruction of CT d'Or images with OPED, there are two possibilities to combine the two data sets: combining the fan data before the reconstruction or adding the reconstructed images appropriately. Combining the fan data eliminates more artifacts, but due to the different energy dependences of the detector types, concentric rings occur in the resulting image. Due to the high resolution of the new image from the C-arm data, just adding the images resulted in a better image than combining the fan data. And most artifacts canceled each other out with this method too. Figure 4.13 shows the comparison between the best images obtained with the old (a) and the new software (b). It is important to point out that the best image with the old software was created by combining the fan data, while the best image of the new software was produced by adding the images of the two data sets.

Figure 4.14 shows that the resulting image has less artifacts than the image obtained with the C-arm device (a) and that the contrast is better than in the image obtained from the mask detectors (b). Considering the drawbacks of the demonstrator (Sec. 3.4), the resulting image is remarkably good and demonstrates the potential of the CT d'Or. However, a lot of optimization still has to be done.

4.4. CT d'Or combined with the clinical CT system

4.4.1. Image reconstruction

A scan of the Alderson Rando phantom was used to develop algorithms for an optimal treatment of the data obtained by combining the CT d'Or device with the clinical CT. The data of the mask

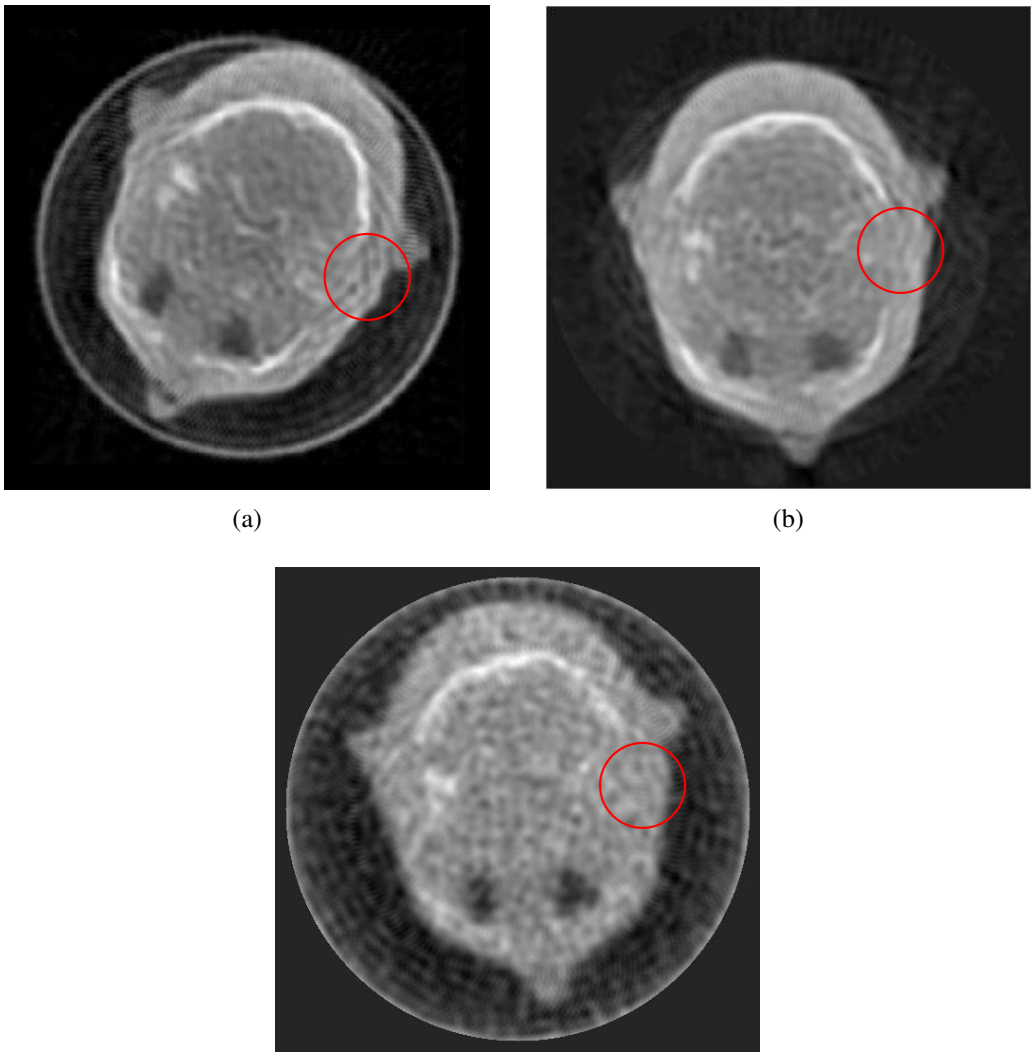

(a) (b)

(c)

Figure 4.12: *Comparison of the images of the mask detectors reconstructed with the old software (a), the new software for the C-arm device (b) and the adapted software for the combination with the CT scanner (c).*

detectors were collected with the minimum available sampling time of 1 ms. With a maximum available rotation time of the CT scanner of 1.0 s, this enabled 1000 views and therefore the best time resolution which can be achieved when combining the current CT d'Or device with this CT scanner. The sensitivity of the mask detectors however is so low that this sampling time resulted in a maximum count rate of about 36 counts per ms in an empty scan and only 1 or 2 counts per ms behind an object. To reduce the resulting noise, several consecutive rotations were averaged. Since the data storage system of the detectors is limited to only 5000 views and due to delays at the start and the end, some data got lost, only four complete rotations could be averaged. The measurements were done in the "perfusion mode", because this is the only mode which allows continuous, repeated scans on the same position. The scans were run with

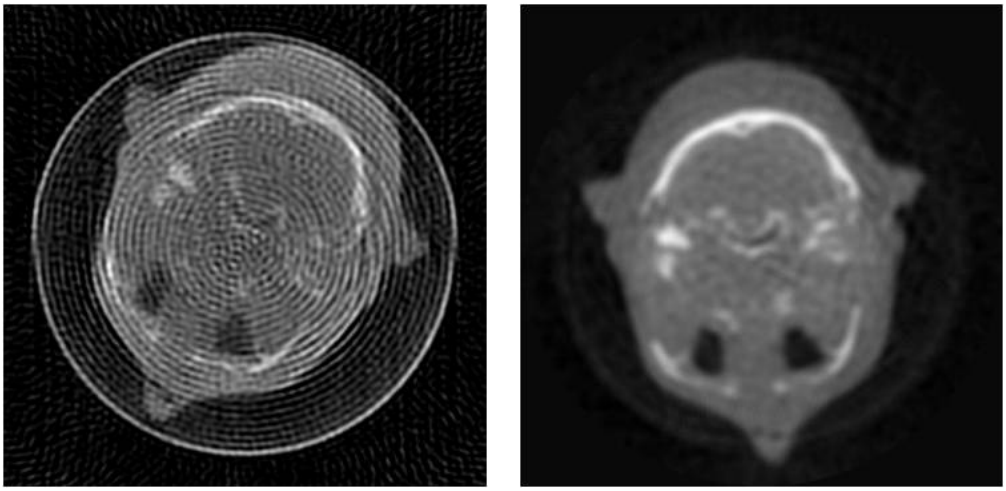

(a) (b)

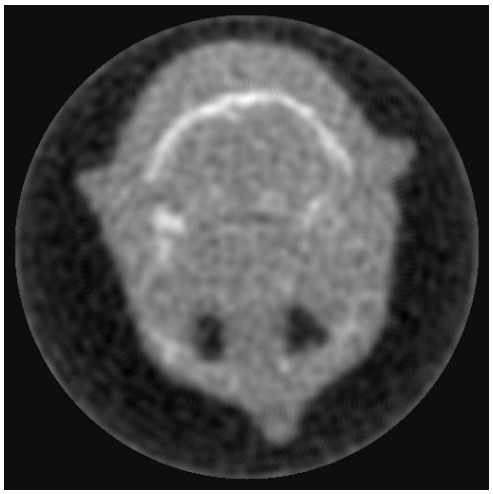

(c)

Figure 4.13: *Comparison of the resulting images obtained by combining the fan data created with the old software (a), by adding the images created with the new software for the C-arm device (b) and for the CT scanner (c).*

a FOV of 50 cm, a source voltage of 120 kVp, a source current of 300 mAs, and a rotation time of 1.0 s. The minimal available slice thickness in the "perfusion mode", which is 2.4 mm, was used. These are parameters typical for a cranial scan and therefore optimal for the phantom.

Data of CT detector

One central line of each frame was used to create the sinogram of the raw data. In order to maximize the resolution, both positions of the z-flying spot were combined. An example for a raw data set of the CT device combined with the CT d'Or ring is shown in Fig. 4.15a.

The data were analyzed in a similar way as the data of the C-arm device, but accounting additionally for the curvature of the detector and the z-flying focal spot. The mathematics used

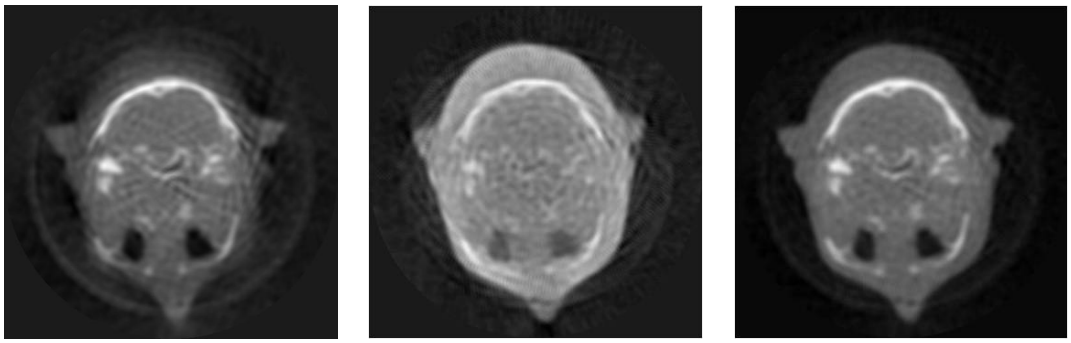

(a) (b) (c)

Figure 4.14: *Adding the images of the C-arm device (a) and the mask detector (b) results in an image with more details and less artifacts (c).*

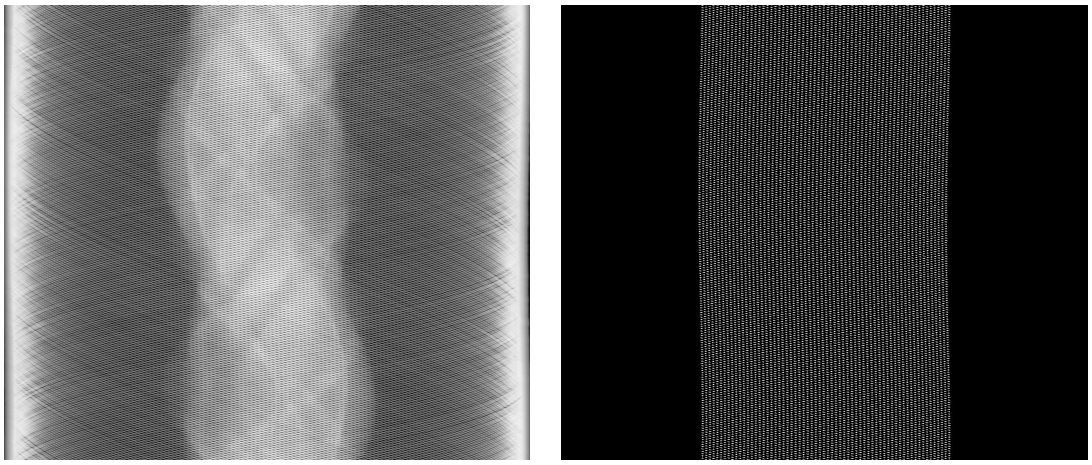

(a) (b)

Figure 4.15: *Exemplary raw data of the CT device combined with the CT d'Or (a) and the created mask (b) for a scan of the Alderson Rando phantom at a FOV of 50 cm.*

for the algorithm can be found in Sec. A.2. The relative position and the angle of the CT d'Or ring to the CT was not known exactly and therefore had to be modulated similar to the way described in the last section. Masks which determined the position of the data points looked like Fig. 4.15b. The fan data set sampled with it is presented in Fig. 4.16a. The 1000 views actually measured have again been binned to 197 effective views which is equal to the number of detectors. The sinogram (Fig. 4.16b) was created in the same way as for the C-arm device and the images were again reconstructed with OPED.

Figure 4.10c shows the resulting image. Its contrast is slightly lower than in the image reconstructed from the data of the C-arm device (Fig. 4.10b), but the contours of the phantom are clearer and the artifacts are less disturbing. This is partly due to a further improvement of the algorithm, which avoids approximations at expense of a longer calculation time. Another reason are the optimized scan parameters for the CT scan, while for the scan with the C-arm

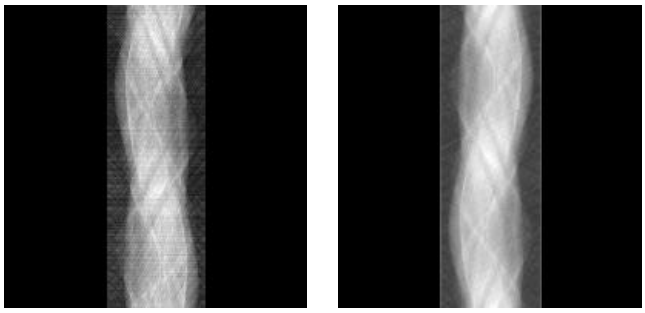

(a) (b)

Figure 4.16: *Exemplary fan data set (a) and resulting sinogram (b).*

device standard parameters were used. But still, artifacts such as the streaks on the side of the skull (red circle) decrease the image quality.

Data of mask detector

An example for an averaged raw data set of a scan of the Alderson Rando phantom at a FOV of 50 cm is shown in Fig. 4.17a. The lighter stripe corresponds to detectors which were irradiated from the back side through the shieldings when they were directly in front of the source. The exact position of the CT d'Or ring in relation to the CT scanner was known from the reconstruction of the CT data, but the relative position of the individual detectors to the source and the relative position of the source to the shieldings and windows had to be determined. Using these parameters the positions at which the data have to be sampled were calculated according to Sec. A.2. The resulting mask for the exemplary data set is shown in Fig. 4.17b. The thereof created fan data set (Fig. 4.17c) was treated in the same way as for the combination with the C-arm device to convert them into the sinogram (Fig. 4.17d) and reconstruct with OPED.

The resulting image is presented in Fig. 4.12c. The contours can be seen clearly, but the noise degrades the image quality drastically. This is on the one hand due to the low sensitivity of the mask detectors. As they are not built to measure with a sampling time of 1 ms, this high noise level had to be expected. The image derived with the C-arm device (Fig. 4.12b) is considerably better due to the better statistics with a sampling time of 20 ms. It is therefore expected that the image taken with the CT scanner would be at least as good as the one from the C-arm device if better mask detectors were used.

On the other hand, the number of samples taken per rotation differed considerably for the two set-ups. When combining the CT d'Or demonstrator with the C-arm device, more than 7000 samples per rotation were collected by the mask detectors, compared to only 1000 samples for the combination with the clinical CT due to the limitations by the maximum rotation time of the CT source of 1.0 s.

In order to further increase the statistics, several images can be added. This considerably reduces the noise, but with an increasing number of images the final image gets more and more

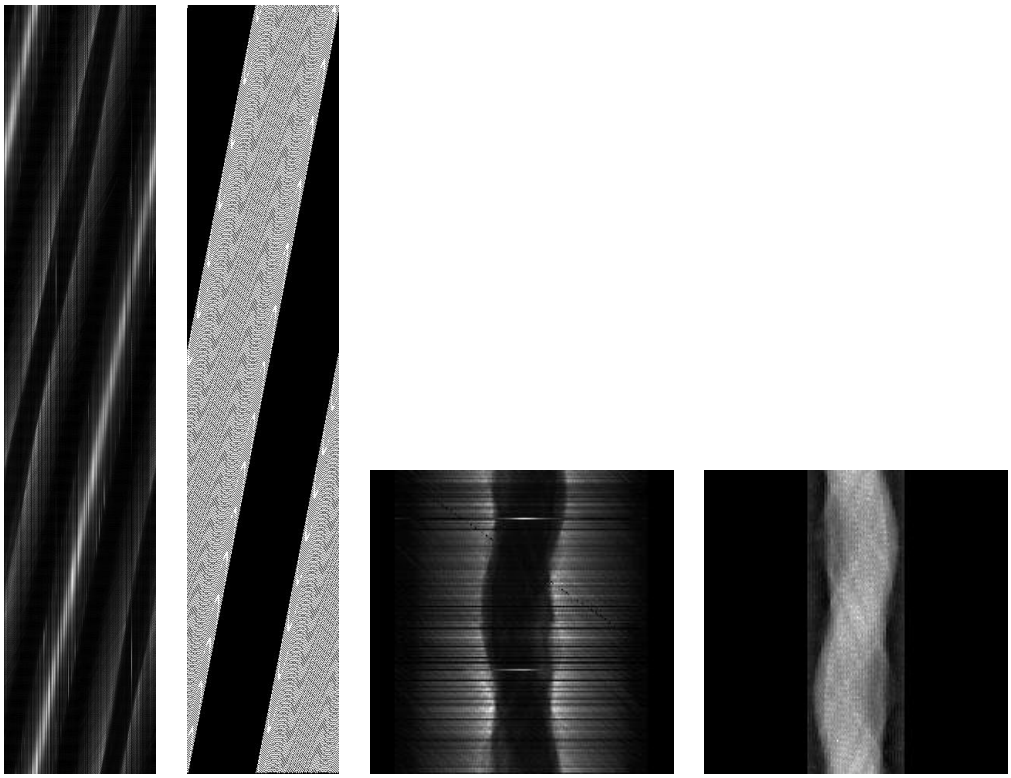

(a) (b) (c) (d)

Figure 4.17: *Exemplary raw data of the CT d'Or ring in the CT scanner (a), the positions at which the data were sampled (b), the fan data set (c), and the resulting sinogram (d) for a scan of the Alderson Rando Phantom at a FOV of 50 cm.*

blurred, due to small inaccuracies in the data sampling. Another possibility is the noise reduction algorithm developed by Tischenko et al. [Tis05]. It compares two images to distinguish between information and noise and subsequently to create a noise reduced image. This method works quite well, but the aim of this chapter was to develop a data processing which can be used for the analysis of the image quality. An artificial increase of the image quality would manipulate the results and therefore be counterproductive. Moreover, both methods need more than one image to produce the final image. Since it was already difficult to get enough measurement time in the clinic to produce the necessary images, it would have been almost impossible to produce twice as much. And as the data have to be independent of each other for the noise analysis, a correction among each other would neither be suitable. Therefore, the original, but rather noisy image, was used for the further analysis.

Combination of both data sets

Adding the image of the mask detectors to the image reconstructed from the CT raw data gives the image shown in Figure 4.18c. The streak artifacts on the side of the skull are reduced (red circle), but the combined image is superimposed by the noise of the mask image. The contrast is

slightly worse for the combined image than for the image obtained from the CT raw data as can be seen using the example of the occipital bone (green circle). It is therefore not clear whether the combined image is really better than the image obtained from the CT data for this data set. Compared to the image obtained with the C-arm device, the image from the CT scanner (Fig. 4.13c) is considerably noisier and has a worse resolution so that less details are visible. But this was also reflected in the time it took to acquire one image. While for the C-arm device it took about three hours, for the clinical CT scanner, the image acquisition, including the data transfer, was finished in three minutes.

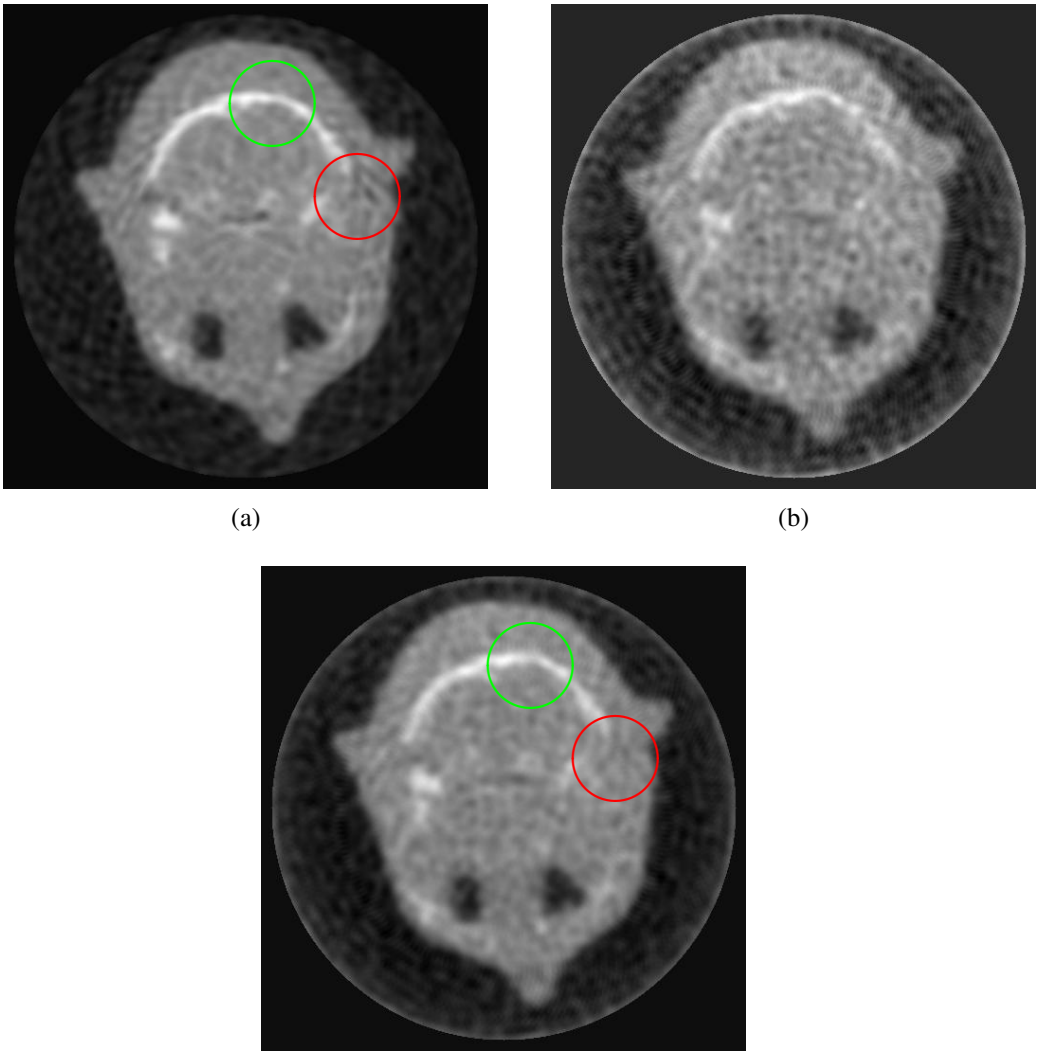

(a) (b)

(c)

Figure 4.18: *Reconstructed images from the raw data of the CT scanner (a), the mask detectors (b) and the combination of both (c).*

4.4.2. Analysis of the reconstructed images

The spatial resolution was determined from combined images of a 1.0 mm steel wire, which was positioned at different distances from the isocenter. The images of the two data sets were added by normalizing them to the maximum of the wire. The resulting images (Fig. 4.19a) show regular patterns, which are due to the data sampling with the calculated mask. The step size in which the four unknown parameters are checked has to be chosen as an optimum between accuracy and computational effort: The smaller the step size, the higher the chance to get an optimal fit to the raw data, but the larger the computation time. Furthermore, the algorithm assumes a perfect alignment of the shieldings. The real CT d'Or ring is however slightly irregular so that the agreement between the raw data and the calculated mask can never be perfect. The patterns appear therefore in every image sampled with the new algorithm, but are masked partially by higher signals for images of the Alderson-Rando and the water phantom.

The PSF could not be oversampled from the wire images, because the CT d'Or demonstrator can only produce one slice. According to Fuchs et al.[Fuc01], the 1-dimensional PSF was instead sampled by rotating the wire image in steps of 0.5° and averaging the resulting 720 profiles. Since rotating the reconstructed image inserts pixel inaccuracies, the profiles were reconstructed individually for every rotation with an adjusted version of the OPED program. By defining the center of the wire, the sampling interval and the angle, any profile through the wire can be reconstructed with the highest available accuracy.

In the same way as for the laboratory and the clinical CT system, the peak of the resulting 1-dimensional PSF was fitted with a polynomial function and the tails were fitted with an exponential decay function. The resulting PSF was rotated to generate the 2-dimensional PSF, which was again used to calculate the H-matrix with three-fold resolution. The MTF was calculated from the 1-dimensional, fitted PSF by Fourier transformation and corrected for the wire thickness d by dividing it through the sinc function:

$$F(u) = \frac{\sin(\pi u d)}{\pi u d}, \tag{4.15}$$

where u is the spatial frequency. For the spatial approach, no correction for the wire thickness was performed.

The noise was analyzed in images of the PMMA-slice (Fig. 4.19b) reconstructed as described above with a pixel size of 0.488×0.488 mm. For the combination of the data sets, the images were normalized to the mean value of the maximum homogeneous region of 285×285 pixels. In the combined image, the average value of the water region therefore was 1, while the average value of air was around 0. The calibration to Hounsfield units was performed by subtracting 1 and multiplying by 1000 so that the average value of the water region became 0, while the average value of air was about -1000. Trend correction was performed by fitting a 2-dimensional second-order polynomial to the 285×285 pixel ROIs and subtracting this function from the ROIs.

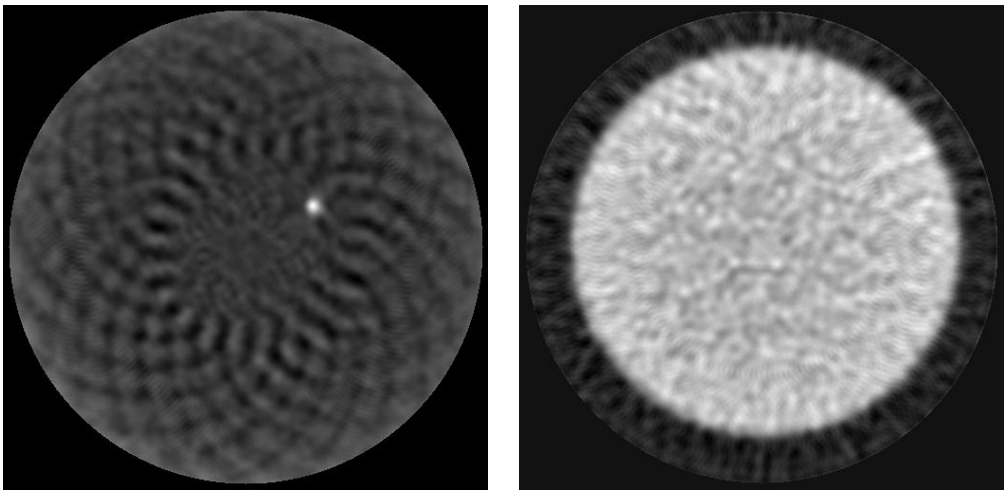

(a) (b)

Figure 4.19: *Examples for reconstructed images of the wire (a) and the PMMA-slice (b).*

Since the acquisition and reconstruction of the images was very time-consuming and the measurement time in the clinic was limited, only 30 images of the water phantom were generated. The resulting autocovariance function (Fig. 4.20) revealed that the range of pixel relations was quite long and not the same for the horizontal and the vertical direction. This is probably due to the regular patterns introduced in the images by the data sampling. In order to accommodate the relations in both directions, the maximum necessary distance of 10 pixels was chosen. With a ROI size of 32×32 pixels and a ROI spacing of 10 pixels, 30 images provided only 1470 ROIs; by far not as much as for the other systems. But this number allowed at least to determine all 1024 eigenvalues of the covariance matrix so that it was invertible and the image space SNR could be calculated. It was however not possible to calculate the location-specific noise for the CT d'Or images.

The spatial resolution at the three different distances from the isocenter and the averaged noise for the whole image were used to calculate the SNR according to the image-space based approach and the Fourier based approach.

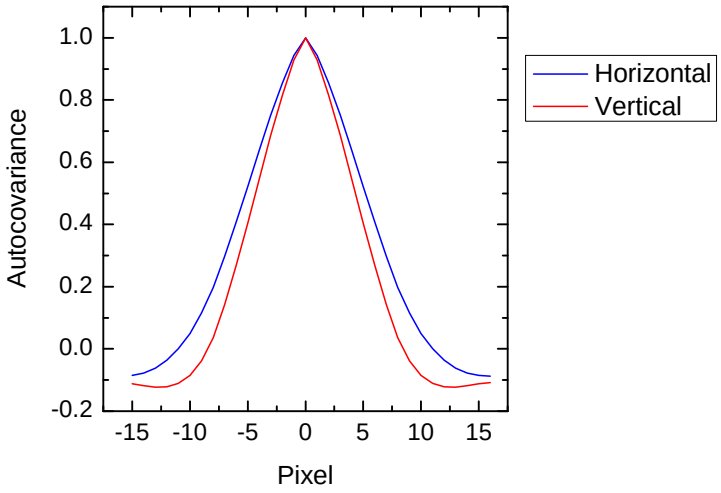

Figure 4.20: *Autocovariance function for the horizontal and the vertical direction*

5. Dose measurements

The quality of an imaging system is defined by the image quality and the dose needed to achieve it. This chapter describes the dose measurements performed for the FDA system (Sec. 5.1) and the CT d'Or demonstrator in combination with the clinical CT (Sec. 5.2).

5.1. FDA laboratory system

In order to make the results of the laboratory CT system comparable to existing data of conventional systems, the dose for each of the four mAs-settings was measured[1]. Therefore, a lid for the cylinder was constructed, which introduced two watertight PMMA-tubes inside the water phantom, one in the center and one on the periphery of the lid (Fig. 5.1). To avoid an air gap, the diameter of the tubes corresponded precisely to the diameter of the 0.6 cc Farmer-type 10×5-0.6 Radcal ionization chamber (Radcal Corp., Monrovia, USA) used for the measurements. The tubes allowed the placement of the sensitive part of the ionization chamber in the central plane of the water-filled cylinder. During each dose measurement, the empty tube was filled with a PMMA-rod to reduce the effects of the air gap. The electrometer used to read out the measured doses is a Radcal 9010 (Radcal Corp., Monrovia, USA). For every current intensity, the dose was measured in the center and at the periphery of the cylinder three times in each case. Table 5.1 lists the averaged results of the measurements and its standard deviations. The variation between the three runs for every setting were apparently very small. In Fig. 5.2, the measured center dose is plotted against the mAs per image. The linear fit (dashed line) shows that due to measurement inaccuracies the center dose for 1.28 mAs per image is slightly too low. This has to be taken into account when analyzing the dependence of the image quality on the dose in Sec. 6.1.

[1] Dose measurements were performed with the help of Samir Abboud from the FDA

Table 5.1: *Overview of the scans and the measured doses*

mAs per projection	Total mAs	Center dose [mGy]	Periphery dose [mGy]
0.625	225.0	9.8 ± 0.0	10.7 ± 0.1
1.28	460.8	17.8 ± 0.1	19.7 ± 0.1
2.00	720.0	28.4 ± 0.1	30.9 ± 0.2
2.50	900.0	35.1 ± 0.1	38.4 ± 0.2

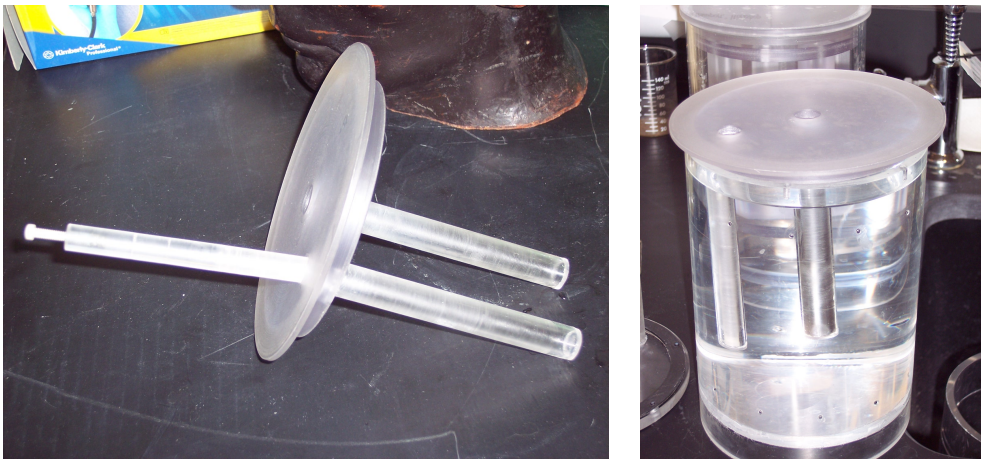

(a) (b)

Figure 5.1: *Lid with two watertight PMMA-tubes and additional PMMA-rod (a) and the cylinder with this lid (b).*

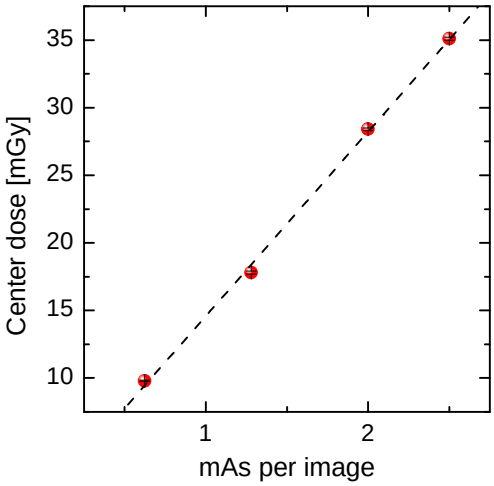

Figure 5.2: *Relation between the mAs per image and the measured dose at the center. The linear fit (dashed line) indicates the expected developing.*

5.2. CT d'Or combined with the clinical CT scanner

5.2.1. Calibration of the TLDs

For the dose measurements in the clinical CT, thermoluminescence dosimeters (TLDs) of type TLD-100H were used, which were provided and analyzed by the Auswertungsstelle of the Helmholtz Zentrum München. These TLDs have a diameter of 4.5 mm and a height of 0.9 mm and are based on crystalline lithium fluoride (LiF), which has been doped with small quantities of magnesium (Mg), copper (Cu) and phosphor (P). The characteristics of TLD-100H that are particularly useful for radiation dosimetry include high sensitivity, almost flat photon energy response, a low fading rate and a linear dose response [Mos06].

The TLDs were calibrated using the radiation emitted by ^{137}Cs. When they are irradiated with a different spectrum, the measured doses have to be corrected. These correction factor can be calculated by dividing the calibration factors for the dose equivalent $H_p(0,07;N)$[2] measured by the Auswertungsstelle with the corresponding conversion factor for air kerma from ISO 4037-3 (Table 18) [ISO99]. Figure 5.3 provides the calculated correction factors with which the measured dose values have to be multiplied to get the actual doses. A factor of 0.83 results for 62.6 keV, the mean energy of the calculated CT spectrum at 120 kVp. Since N-spectra have a completely different energy distribution than CT spectra, this value however was not used for the calibration. The plot is merely supposed to give an impression of the energy dependence of the TLDs.

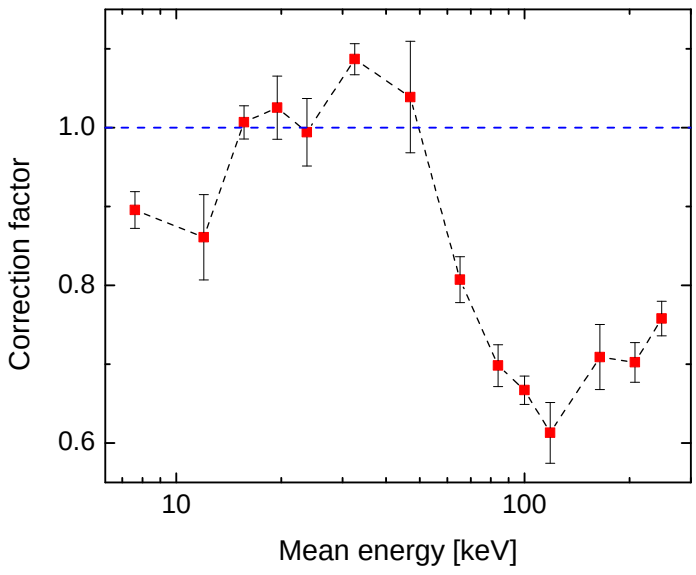

Figure 5.3: *Correction factor for different mean energies*

[2]Dose equivalent in a depth of 0.07 mm for N-spectra and a rod phantom consisting of ICRU tissue at a reference distance of 2 m

Instead, the calibration factor was measured in the Secondary Standard Dosimetry Laboratory (SSDL) of the Helmholtz Zentrum München[3]. Therefore, 50 TLDs were irradiated with a spectrum comparable to the CT spectrum, which was produced using the information that the total filtration on the central axis equals 6.8 mm aluminum for the head scan [ImPACT06]. Similar to the CT scans, a source voltage of 120 kVp was used. A shutter right after the source ensured that exactly 30 mGy were applied to the TLDs. This was confirmed by irradiating a 30 cm^3 ionization chamber (Unidos 10001-1 0003, PTW Freiburg, Germany) with a 3 mm thick plexiglass disk in front of it to simulate the front side of the rack which held the TLDs. The plexiglass rack was loaded twice with 25 TLDs, placed at the same position as the ionization chamber before and irradiated again with 30 mGy.

The average dose measured with the TLDs was 32.53 mGy with a standard deviation of 0.94 mGy or 2.9 %. This resulted in a calibration factor k_Q of

$$k_Q = \frac{30}{32.53} = 0.92. \tag{5.1}$$

Together with the correction factors in Fig. 5.3, this result demonstrates that the TLDs used for this work are suited for dose measurements in energy ranges corresponding to those in clinical CT scanners.

5.2.2. Dose measurement

Dose in the CT d'Or system was measured using the slice of the Alderson Rando phantom presented in Sec. 3.4. The Alderson Rando phantom has 16 holes of 4.8 mm diameter for dose measurements, which are normally filled with PMMA rods. The uncertainty of the measurements was reduced by placing two TLDs in every hole. In order to position the TLDs in the middle of the slice, 32 PMMA rods of 4.8 mm diameter and 1.2 mm height were manufactured to fix the TLDs from both sides. The phantom and the positions of the holes are shown in Fig. 5.4.

For dose measurements with the CT d'Or ring, first the phantom without TLDs was placed in the device and some images were taken with the minimal available slice thickness for head scans of 18 mm. With the help of these images, it was ensured that the CT d'Or ring was aligned correctly and that the x-ray cone did not hit the plate at the backside of the CT d'Or ring, while the whole phantom was irradiated. Then the TLDs were placed in the phantom, which was fixed with double-sided adhesive tape to the plate on which the CT d'Or ring is mounted. A sequential head scan with 2.0 s rotation time, 120 kVp and 300 mAs was performed. It has to be noted that the nominal rotation time of 2.0 s for the head scan means that there are 2 rotations with 1.0 s rotation time each. After the measurement, the TLDs were stored separately in small, numbered plastic bags to be able to assign them to the right positions.

[3]These measurements were performed under the advice of Werner Panzer of the same institute.

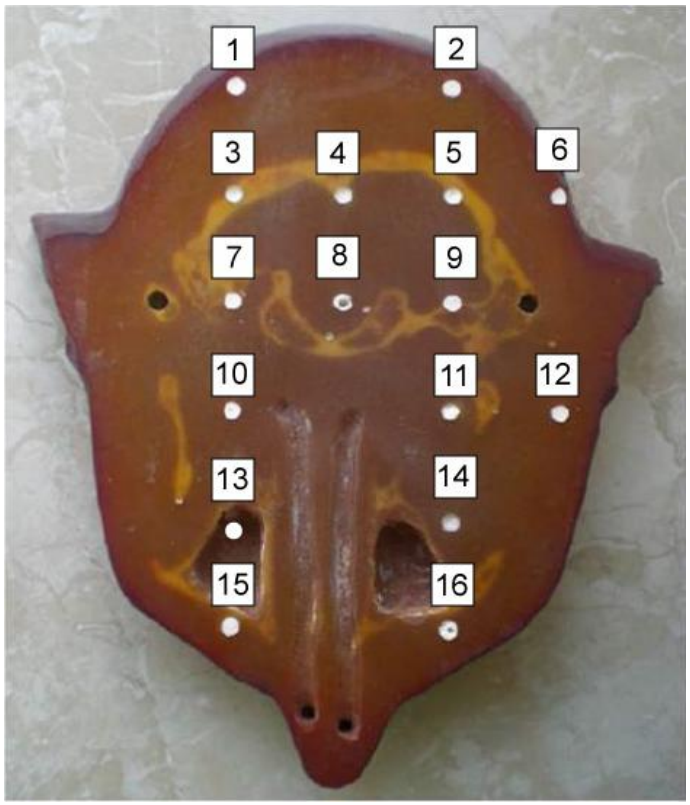

Figure 5.4: *Positions of the TLDs in the Alderson-Rando-phantom*

For dose measurements without the CT d'Or ring, the phantom was stuck to the front side of the water phantom, which is normally used to measure the noise in the CT scanner (compare Sec. 3.2). Again, it was ensured that the phantom was positioned accurately and that the x-ray cone did not hit the water phantom before the TLDs were inserted. The irradiation was performed using the same parameters as for the measurement with the CT d'Or. Directly after the measurements, the numbered bags where sent to the Auswertungsstelle for readout.

The measured dose values were multiplied with $k_Q = 0.92$ to obtain the calibrated values listed in Tab. 5.2. The calibration factor k_Q measured in Sec. 5.2.1 however corresponds to the spectrum on the central axis in air, because the only information available about the filtration in the clinical CT is that it is equal to 6.8 mm aluminum [ImPACT06] in the center. Using this spectrum is only a rough estimation which does not allow to determine the exact calibration factor for the TLDs due to several reasons. First, the ImPACT report does not state definitely whether this filtration also includes the bowtie filter. If not, an additional filtration would harden the actual spectrum on the central axis. Second, the spectrum will become harder with increasing distance from the central axis, because of the increasing thickness of the bowtie filter. Since the exact shape, as well as material and thickness, of the bowtie filter in the clinical CT scanner is part of the cooperate secret, the spectra away from the central axis cannot be simulated. Third, the phantom tissue changes the spectrum additionally. But due to the inherent filtration and the bowtie filter, the spectrum is already so hard that these changes play a minor role.

Table 5.2: *Measured doses with and without the CT d'Or ring and the ratio of the two measurements*

Number of hole	Dose with CT d'Or [mGy]	Dose without CT d'Or [mGy]	ratio
1	7.42	18.96	0.39
2	6.98	19.03	0.37
3	5.28	14.17	0.37
4	4.62	12.47	0.37
5	5.09	14.14	0.36
6	7.15	20.51	0.35
7	4.53	11.92	0.38
8	3.90	10.83	0.36
9	4.28	12.00	0.36
10	4.94	12.77	0.39
11	3.99	11.19	0.36
12	7.29	19.49	0.37
13	6.03	14.90	0.40
14	5.77	15.00	0.38
15	8.17	19.73	0.41
16	7.68	18.65	0.41
		Average of all ratios	**0.38**

Due to these reasons, the actual calibration factor is estimated to be up to 0.2 smaller than the measured one, because the mean energies of the actual spectra are in a range where the efficiency of the TLDs increases abruptly. However, the focus of this work lies on the relative dose comparison between the CT scanner on its own and the combination of CT scanner and CT d'Or device. Since it has been shown in Sec. 5.2.1 that the TLDs are suitable for the applied energies, the actual calibration factor is of minor interest.

Table 5.2 shows that the averaged ratio of the measured dose values is 0.38. As described in Chapter 3.4, the lead shieldings of the CT d'Or ring have a width of 5 mm while the windows are only 3 mm wide. So $\frac{5}{8} = 0.625$ of the circumference are shielded and $\frac{3}{8} = 0.375$ are windows. The averaged ratio of the doses corresponds exactly to the fraction of the unshielded parts suggesting that the shieldings absorb 100 % of the photons.

But simulating the spectra on the central axis with and without 0.5 mm lead (Fig. 5.5) reveals the photon absorption to be only about 93 %. The thinner parts on the corners of the shieldings (compare Fig. 3.8) absorb even less. The incomplete photon absorption can also be seen in the raw data of the CT d'Or device, where the count rate of detectors irradiated from the back side through the shieldings is always increased (Fig. 4.11a and Fig. 4.17a). This effect should

add at least 7 % of the fraction of the shielded part (0.625) to the fraction of the unshielded part (0.375), resulting in an expected ratio of about 0.42 between the dose with and without CT d'Or.

Another issue one has to be aware of is that the spectrum is hardened by the mask and therefore the detectability efficiency of the TLDs for that contribution is further increased. The simulated spectra in Fig. 5.5 show that the mean energy of the spectrum on the central axis increases due to the filtration with 0.5 mm lead from 62.6 keV to 74.9 keV and that the shieldings almost completely absorb energies higher than 88 keV, which corresponds to the K-edge of lead. But this effect is supposed to be most remarkable in the center, since the spectrum on the peripheries is already hardened by the bowtie filter. The harder the spectrum, the less the change caused by an additional filtration such as the shieldings.

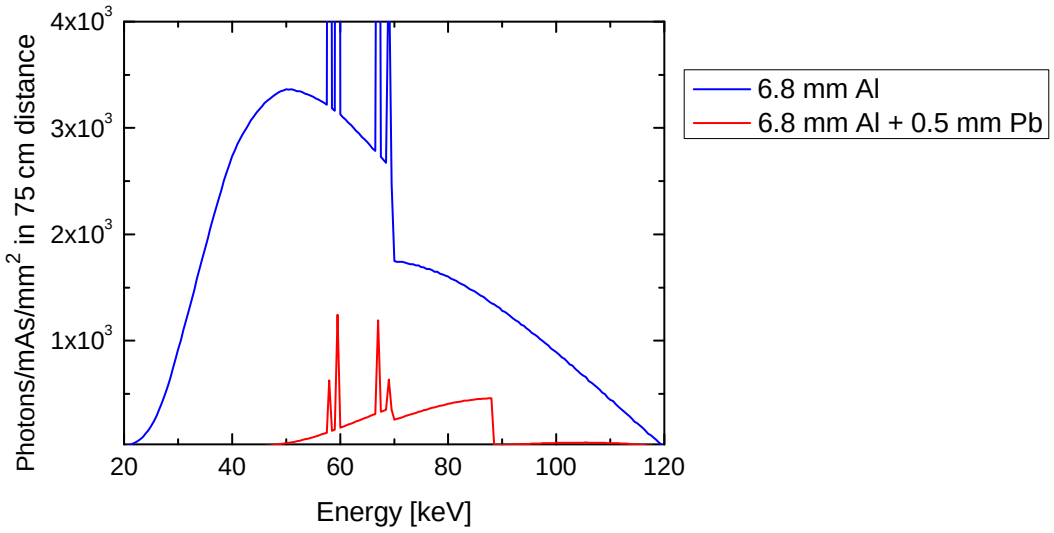

Figure 5.5: *CT spectrum at the center where the filtration corresponds to 6.8 mm aluminum (blue) and with an additional attenuation of 0.5 mm lead (red)*

The reduction of scattered radiation due to the special geometry of the CT d'Or can possibly counterbalance the incomplete absorption by the shieldings. Since only a small amount of radiation passes the shieldings, the scattered radiation in the shielded parts of the object is small, and the contribution of scatter to directly irradiated parts is low. This effect is expected to become even more important for larger volumes (e.g., in multi-slice CT), because the fraction of scattered radiation is increased. For a quantitative estimation, appropriate simulations would have to be performed, but this task is beyond the scope of this work.

It has to be pointed out that the result of these measurements is only meaningful for the demonstrator of the CT d'Or. A clinical applicable CT d'Or is supposed to have at least 1000 detectors and therefore smaller and probably thinner lead shieldings, resulting in a higher transmission of x-ray photons. Simulations showed that this issue can be solved by using tungsten or rhenium instead of lead. Their absorption rate is higher in the relevant energy range due to a higher density, which more than compensates for the lower atomic numbers. Even though more

expensive than lead, tungsten-rhenium alloys are widely used in industry so that they are available at a reasonable price. The resulting increase in cost is expected to be marginal compared to the price of the whole CT system.

6. Analysis of image quality

This chapter presents the results obtained by analyzing the images of the different CT systems using both approaches, the image-space based and the Fourier based. In order to decide which method provides a more realistic description of the imaging system, the results were additionally compared to measured images. The sections about the FDA system (Sec. 6.1) and the clinical system (Sec. 6.2) demonstrate the potential of the image-space and the Fourier approach and the image quality achievable by conventional CT geometries. Section 6.3 then presents the image quality analysis for the CT d'Or demonstrator in combination with the clinical CT.

6.1. FDA laboratory CT system

Spatial resolution

The spatial resolution of the FDA laboratory system was measured with a molybdenum foil and the image data were processed as described in Sec. 4.1. Figure 6.1 presents the profile of the fitted, 2-dimensional PSF, which was used to calculate both the H-matrix and the MTF.

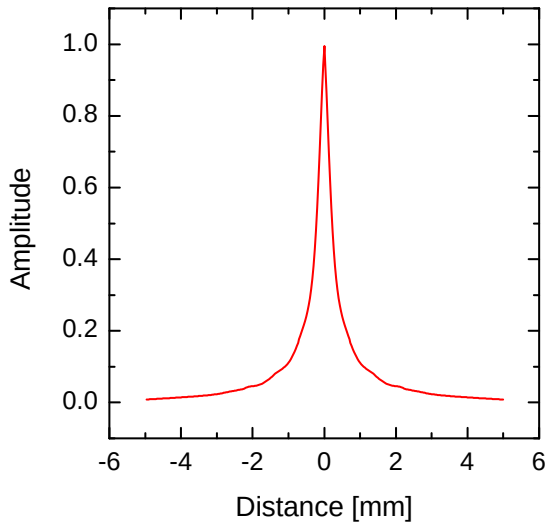

Figure 6.1: *Profile of the fitted, 2-dimensional PSF used to calculate the H-matrix and the MTF.*

The singular values of the H-matrix sorted in descending order (a) and the corresponding MTF (b) of the system are presented in Fig. 6.2. The curves have different absolute values, because the MTF is normalized to 1. Also the shape of the curves differs considerably, as

the slope of the singular values is much steeper than the MTF. This indicates that the spatial resolution of the system is worse according to the image-space based approach than according to the Fourier based approach.

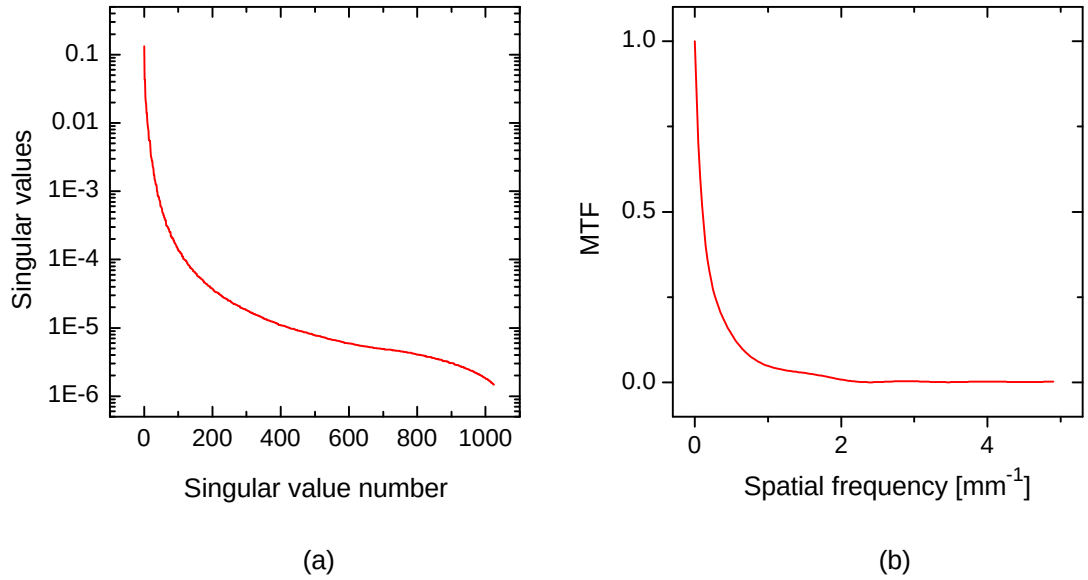

Figure 6.2: *Singular values of the H-matrix (a) and the corresponding MTF (b) of the laboratory CT system. Please note that the scaling on the y-axes is not the same.*

The signal transfer through the imaging system was visualized by simulating two objects and applying either the H-matrix or the MTF: a disk modeling a dense mass inside a lower density region and a torus modeling a dense mass with a fatty margin inside a higher density region (Sec. 4.1). Figure 6.3 and Fig. 6.4 compare the transfer of the input signals $\mathbf{f}$ (a) through the imaging system as calculated with the H-matrix (b) and the MTF (c). For both signals the resulting image is significantly blurred when operating $\mathbf{H}$ on $\mathbf{f}$. The ring seems to be much broader than it really is and the hole in the center is not visible. The images generated with the MTF are much sharper, as indicated by the gentler slope of the MTF compared to the singular values of the H-matrix. A possible explanation for this difference are the very long tails of the scanner PSF, extending beyond 32×32 pixels or 1.6 mm respectively. The reason for these fairly long tails is the large focal spot (0.6 mm) so that the focal spot unsharpness widens the PSF [Kyp05b]. Based on the PSF image, ROIs in the order of 100×100 pixels would be needed, resulting in a H-matrix of $10^4 \times 9 \cdot 10^4$ pixels. This sizes makes it difficult to manipulate and to analyze the matrix by singular value decomposition. The presampled MTF approach does not have this issue, because it captures the long-range tails at the low frequencies.

In order to evaluate which approach provides a more realistic description of the imaging system, measured images of an object comparable to a simulated signal are necessary. Since there was no appropriate phantom available for the laboratory CT system, this discussion had to be postponed to the clinical CT system (Sec. 6.2.2).

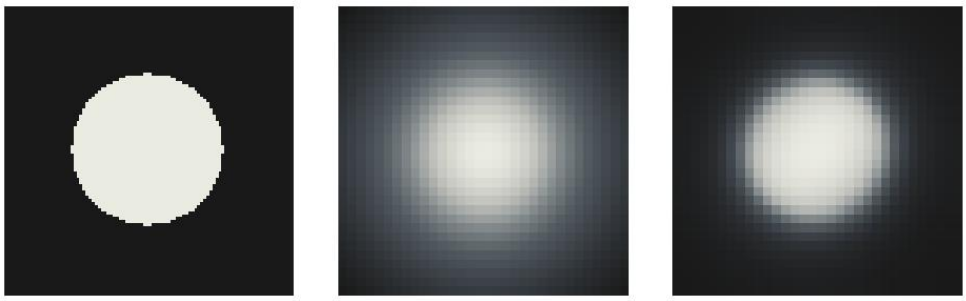

(a) (b) (c)

Figure 6.3: *Comparison of the transfer of the simulated disk (a) using the image-space approach (b) and the Fourier approach (c).*

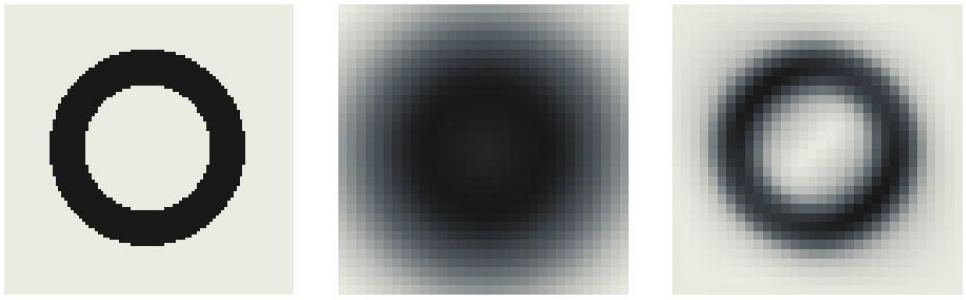

(a) (b) (c)

Figure 6.4: *Comparison of the transfer of the torus (a) using the spatial approach (b) and the Fourier approach (c).*

Noise

The covariance matrix as well as the NPS have 1024 eigenvectors, because 32×32 pixel ROIs were used for the analysis of the noise. The eigenvectors of the Fourier transformation are by definition exponential wave functions, while the image-space based approach obtains optimized eigenvectors from the eigenanalysis of the covariance matrix. The same number of eigenvectors of the covariance matrix is therefore expected to provide a better or at least equal representation of the imaging system as the eigenvectors of the Fourier approach. For a better visualization, the eigenvectors of length 1024 have been reformed to 32×32 arrays, which is justified since the covariance matrix they define was calculated from ROIs of this size. Figure 6.5 shows the first 64 eigenvectors of the covariance matrix for the xy- (a) and the yz-plane (b) ordered with decreasing magnitude of their corresponding eigenvalues. While the eigenvectors of the xy-plane are irregular with no preferred direction, the eigenvectors of the yz-plane show a clear vertical pattern, which indicates vertical correlations introduced by the 1-dimensional nature of the reconstruction filter.

In order to visualize the difference between the eigenvector sets, the exponential wave functions which define the Fourier transformation were calculated for the 2-dimensional NPS. To

make them comparable to the eigenvectors of the covariance matrix, the values of the 2-dimensional NPS were sorted in descending order and the real part of the first 64 eigenvectors is presented in Figure 6.6. Due to this sorting the first eigenvector is not the one with the largest wave length, but the dominating eigenvector.

The comparison reveals that the eigenvectors of the covariance matrices do not have the regular structure of exponential wave functions.

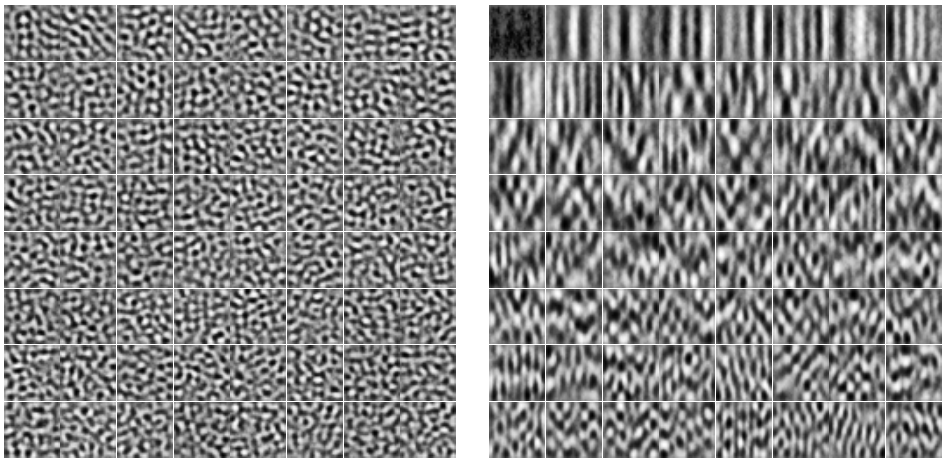

(a) (b)

Figure 6.5: *First 64 eigenvectors of the covariance matrix for 35.1 mGy in the xy-plane (a) and in the yz-plane (b).*

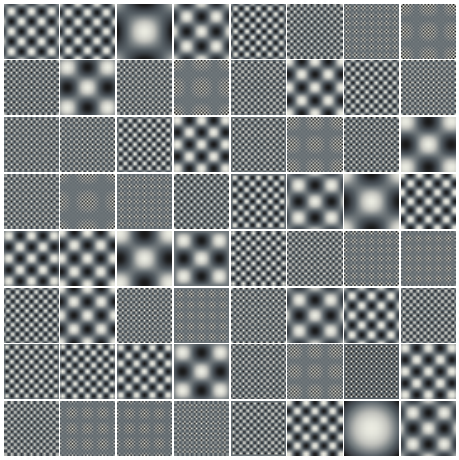

Figure 6.6: *Calculated first 64 eigenvectors of the NPS.*

Figure 6.7 presents the eigenvalues of the covariance matrix (solid symbols) sorted in descending order for the xy-plane (a) and the yz-plane (b). Additionally, the values of the 2-dimensional NPS are listed in descending order (open symbols). The comparison is only qualitative, because eigenvalues and NPS values are not based on the same set of eigenvectors. It is therefore not possible to directly interpret the lower maximum and slightly higher minimum

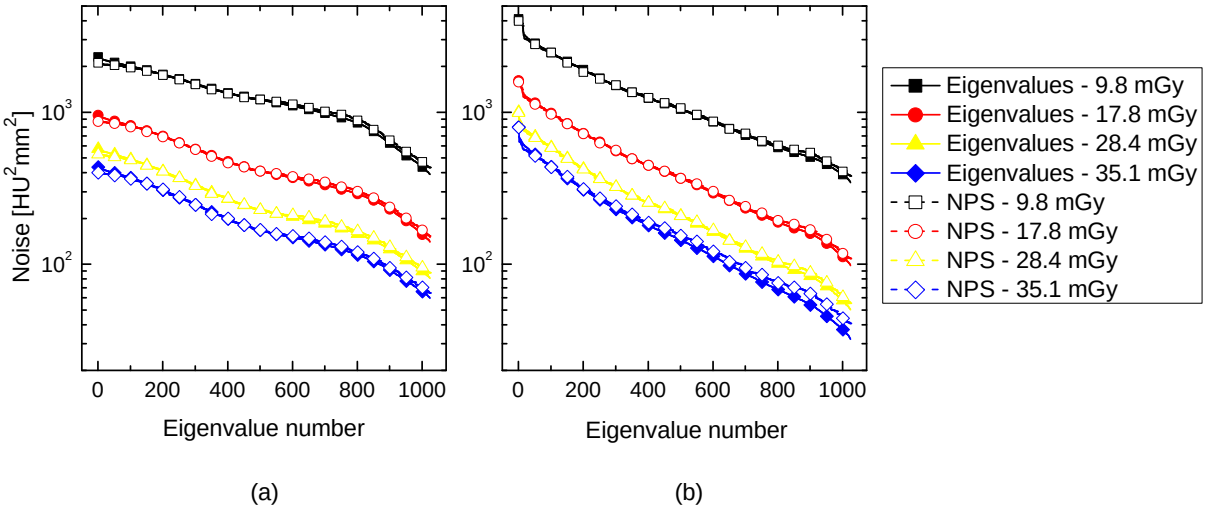

Figure 6.7: *Eigenvalues of the covariance matrix and values of the 2-dimensional NPS sorted in descending order for the xy-plane (a) and the yz-plane (b). As every curve represents 1024 values, the symbols do not correspond to points, but are inserted for better curve separation.*

values of the NPS. However, the integral of the 2-dimensional NPS, as well as the integral of the eigenvalues of the covariance matrix, is supposed to be equal to the variance of the noise. A comparison reveals that the integrals of both curves differ by less than 10^{-6} % from each other and are therefore practically equal. Both approaches thus agree on the total amount of noise. This fact was proved for CT images in this work for the first time.

The 1-dimensional, radially averaged NPS is shown in Fig. 6.8 for the xy-plane (a) and the yz-plane (b). The anti-correlated noise, characteristic for the axial direction of CT scanners, generates a typical curve for the NPS, similar to the ones reported by Wagner [Wag79] and Hanson [Han79]. The NPS of the xy-plane starts at a high magnitude at frequencies close to zero, has a slight drop at low frequencies, increases at mid-frequency range and decreases to zero at higher frequencies. For the same dose level, the bump in mid-frequency range is strongly dependent on the utilized reconstruction filter, which means that the more "edge-enhancing" the reconstruction filter, the higher is the bump. Since the reconstruction algorithm used for this work is mainly focused on optimizing the axial images, it does not perform an edge enhancement for the yz-plane and the corresponding NPS therefore decreases monotonically.

Location-specific noise

In order to analyze the location-specific noise, the xy-cylinder plane was subdivided into nine equally sized, square regions as shown in Fig. 6.9a for an image taken at 35.1 mGy. The covariance matrix and the NPS of each region were calculated to obtain the location-specific eigenvectors and eigenvalues. Figure 6.9b shows the 1^{st} eigenvectors at the positions of the corresponding regions. The resulting starlike pattern of the eigenvectors illustrates the radially symmetric nature of the FBP reconstruction algorithm. Therefore, the central vertical region exhibits vertically symmetric eigenvectors, the central horizontal region exhibits horizontally

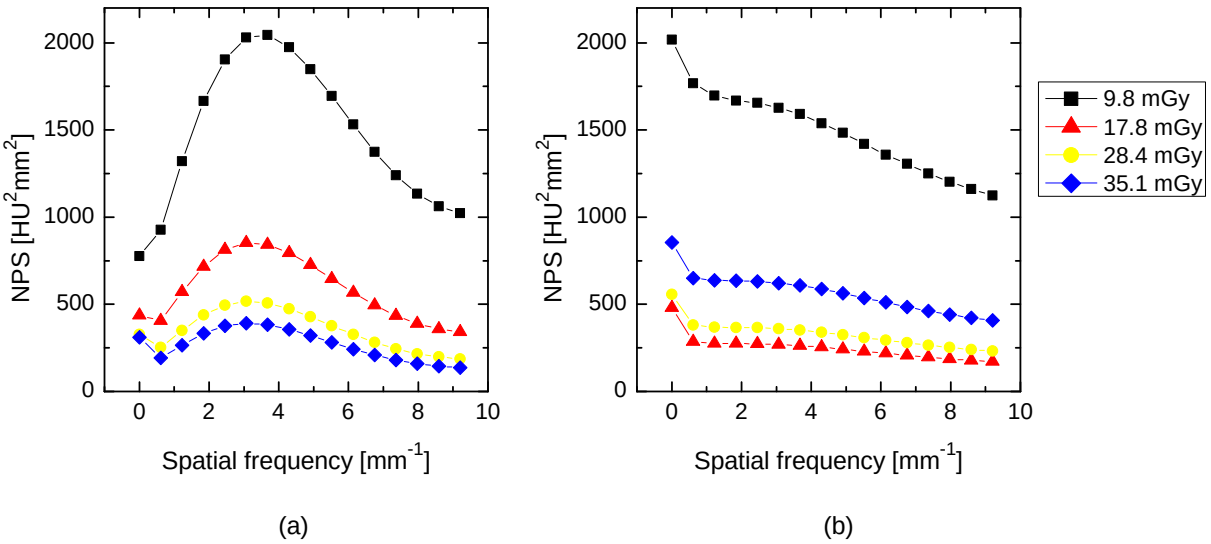

Figure 6.8: *NPS for the xy-plane (a) and the yz-plane (b).*

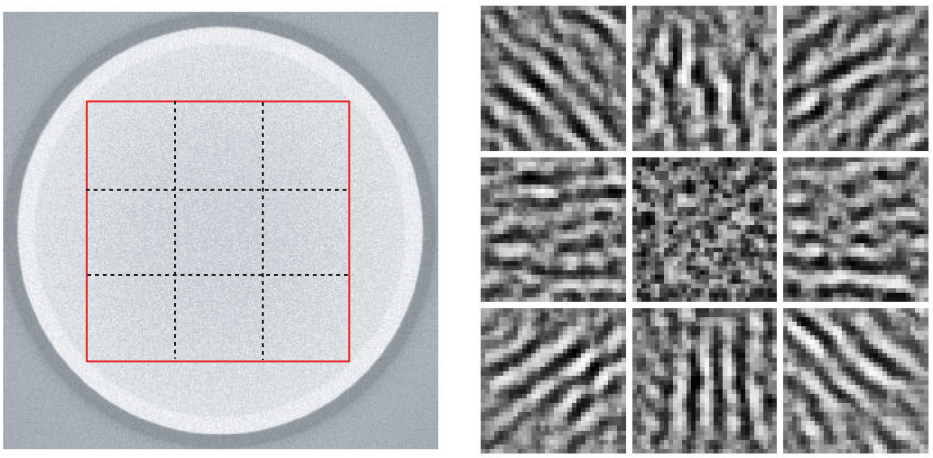

Figure 6.9: *A noise image taken at 35.1 mGy was partitioned into 9 square regions (a) and the 1^{st} eigenvectors were positioned at the corresponding regions (b).*

symmetric eigenvectors, the diagonal regions diagonal, and the central region has no directional preference because the contributions of all directions are superimposed.

The corresponding eigenvalues (a) and the NPS (b) in Fig. 6.10 reveal that the magnitude of noise is higher in the central region than in the peripherals, which is reasonable as the contrast is normally higher in the central region of images reconstructed with the FBP algorithm.

SNR

Comparison of the SNR

For the simulated disk and the torus, the SNR^2 is plotted in Fig. 6.11 for both approaches. The image-space SNR is for both signals smaller than the Fourier SNR. This can be explained by a

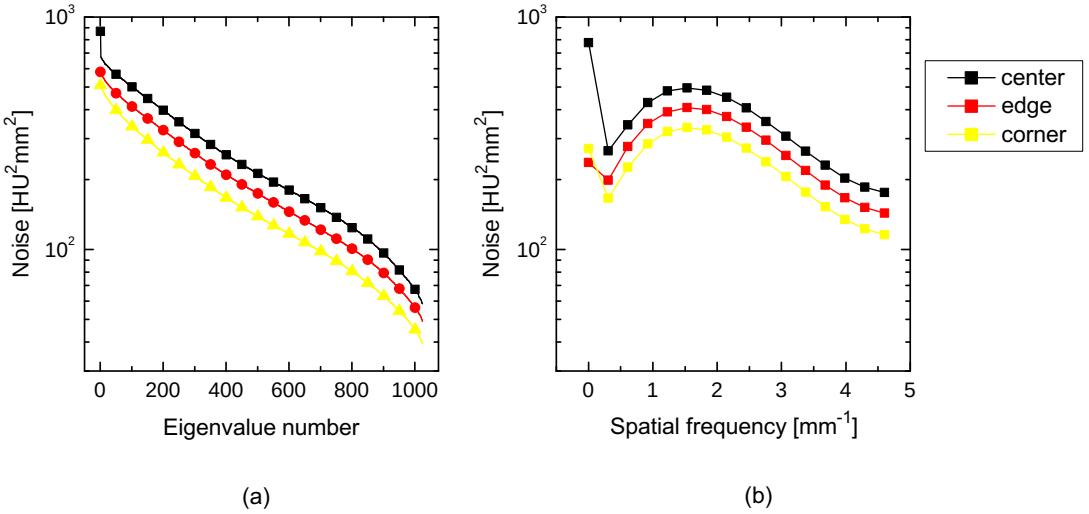

Figure 6.10: *Eigenvalues (a) and NPS (b) for different regions of an image reconstructed from data taken at 35.1 mGy. As every curve in (a) represents 1024 eigenvalues, the symbols do not correspond to points, but are inserted for better curve separation.*

better spatial resolution according to the MTF than according to the H-matrix, while the noise was the same for both approaches. Furthermore, the Fourier SNR^2 is lower for the torus than for the disk even though their surface area is the same, while the spatial SNR^2 is only slightly lower for the torus than for the disk. The applied Fourier transformation seems to be more dependent on the shape of the signal, while the matrix multiplication performed by the spatial approach depends mainly on the actual signal area.

The SNR^2 is not exactly linear with the dose, because of the not exactly linear relation between the mAs-setting and the dose (compare Sec. 5.1). This explains the deviation for the Fourier SNR, but the image-space SNR additionally shows a drop in the last value. Since this effect is the same for both tasks, it cannot be caused by the signal but probably by the generation of the PSF.

Detection threshold

As described in Sec. 2.3, the detectability of an object equals the SNR for a SKE/BKE situation and the detection threshold ($p = 0.75$) can be related to the SNR through an error function. In order to demonstrate the practical benefit of the SNR, the detection threshold as a function of the area and the amplitude of a disk is shown in Fig. 6.12. Due to the higher SNR, smaller and lighter disks can be detected according to the Fourier approach than according to the image-space approach. Such a chart can theoretically be used by the radiologist to determine the necessary dose for an examination depending on the task.

Bootstrapping calculation

With a spacing of four pixels, 105800 ROIs were created from the 877×877 pixel water region of the 200 reconstructed slices to calculate the covariance matrix for the whole images. For each of the 9 regions, only 12800 ROIs were available to determine the location-specific noise.

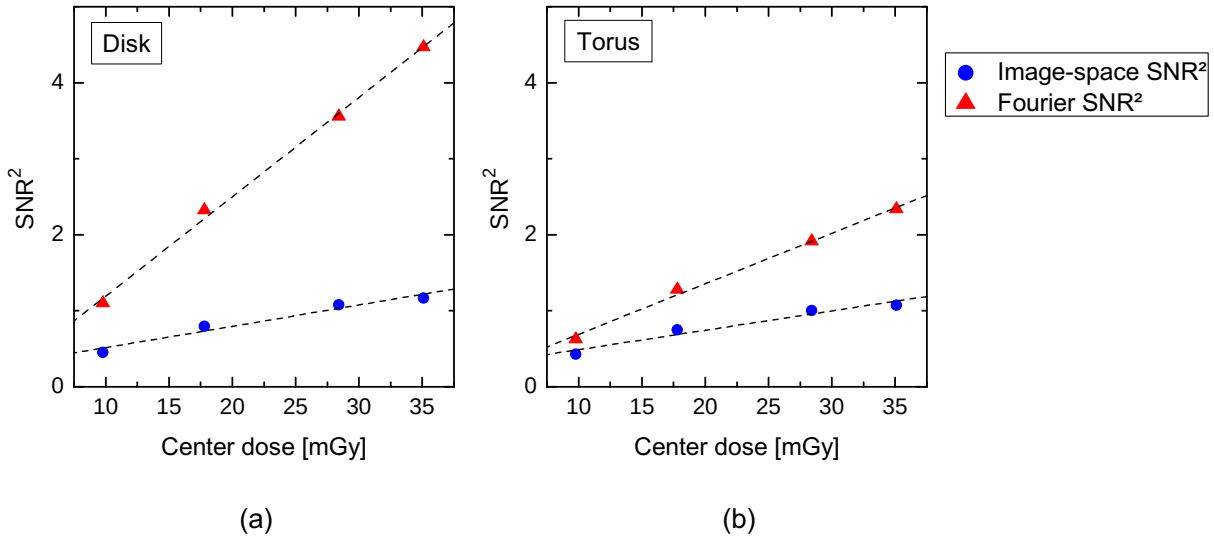

Figure 6.11: *SNR for the simulated disk (a) and the torus (b). Linear fits for the data points are shown with black, dashed lines.*

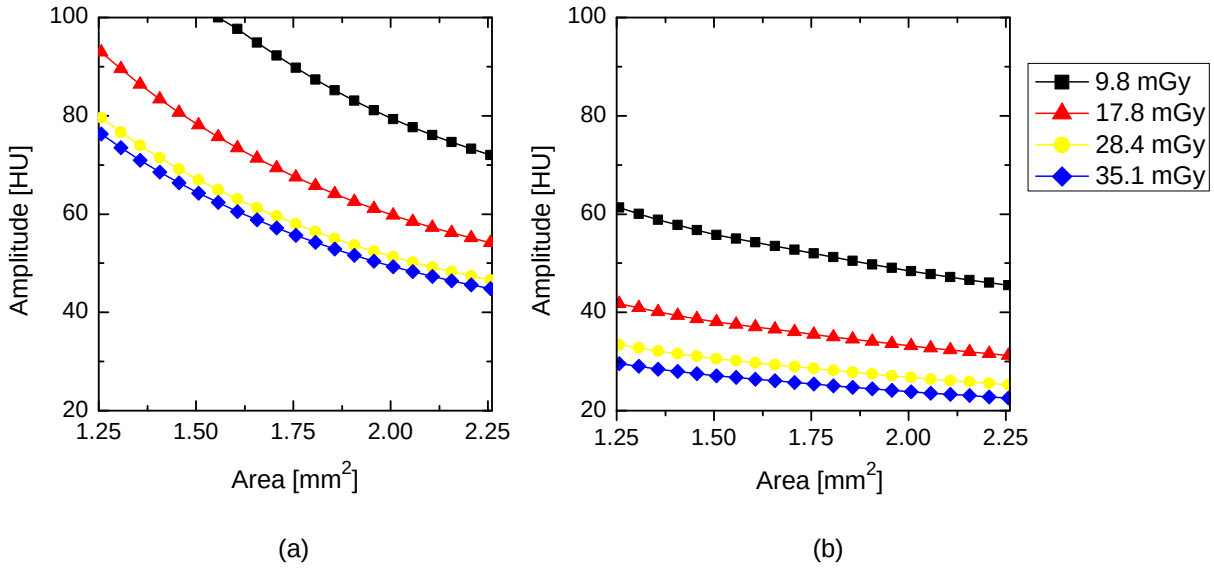

Figure 6.12: *Detection threshold for the image-space (a) and the Fourier (b) approach.*

In order to check whether these numbers of ROIs are enough to properly define the 1024×1024 matrices, a bootstrapping calculation was performed for 9.8 mGy as described in Sec. 4.1.

As expected, the standard deviation of the SNR decreased with an increasing n as can be seen in Fig. 6.13a. An exponential decay fitted the data points very well. Also the actual value of the SNR decreased exponentially with an increasing number of ROIs (Fig. 6.13b). The fit converged to a SNR value of 0.675 for a very large number of ROIs which is very close to 0.673, the value obtained by using all 105800 ROIs. For the laboratory CT system, 105800 ROIs were therefore enough to accurately define the covariance matrix and enabled the calculation of a reliable image-space SNR.

For 12800 ROIs, the fits in Fig. 6.13 gave a standard deviation of about 0.7 % and a SNR value of 0.702, which is 4.0 % higher than the actual SNR. Since the SNR depends inversely linear on the covariance matrix and hence on its eigenvalues, the location-specific eigenvalues are supposed to be 4.0 % $\pm$ 0.7 % lower than the actual values. Due to the low standard deviation, the covariance matrices are defined accurately enough for a relative comparison of the 9 regions such as done in Sec. 6.1.

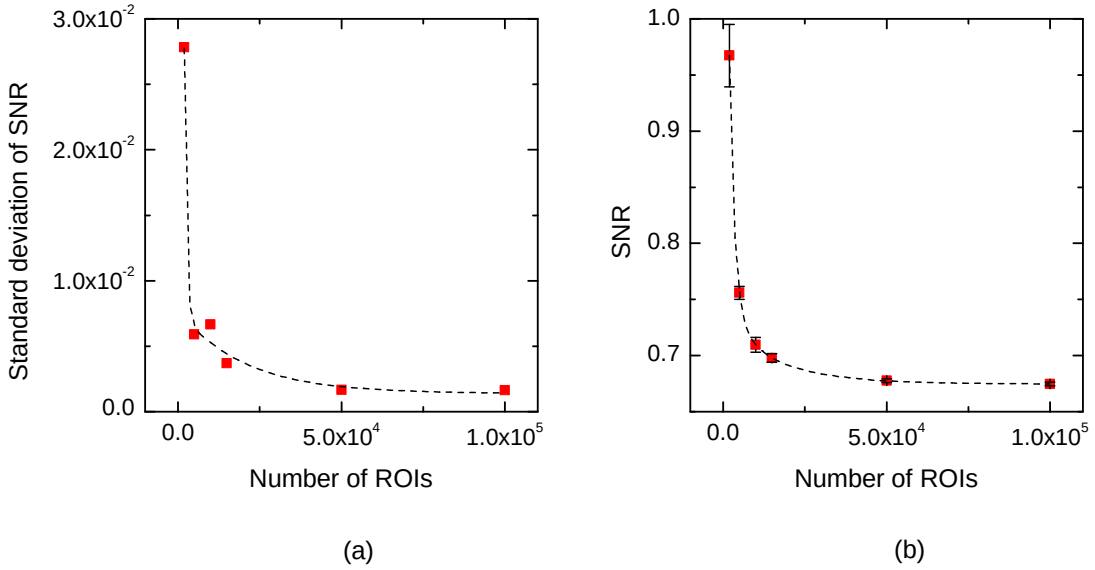

Figure 6.13: *Results of the bootstrapping calculations for 9.8 mGy. An exponential decay fitted the standard deviation (a) as well as the actual SNR (b).*

6.2. Clinical CT system

For the clinical CT system not only the quality of the reconstructed images was analyzed, but also the image quality of the raw data. The following section therefore presents a new method for the analysis of the raw data with the Fourier approach, which was developed with focus on new CT geometries such as the CT d'Or. Subsequently, images of the clinical CT reconstructed with various different filters were analyzed.

6.2.1. Raw data

Spatial resolution

The MTF of the raw data was determined for different wire - isocenter distances according to Sec. 4.2.1. The distances denoted in Fig. 6.14 were calculated from the CT raw data with the procedure described in Sec. 4.2.1. The MTF decreases with an increasing wire - isocenter distance, because of the bowtie filter of the CT which compensates for the shape of the human

body or head. Scattering in the filter causes a broadening of the effective focal spot size, which decreases the MTF. Since the filter is becoming thicker on the peripheries, the fraction of scattered radiation increases and hence the MTF decreases. The MTF curves determined from the CT raw data therefore behave according to theory.

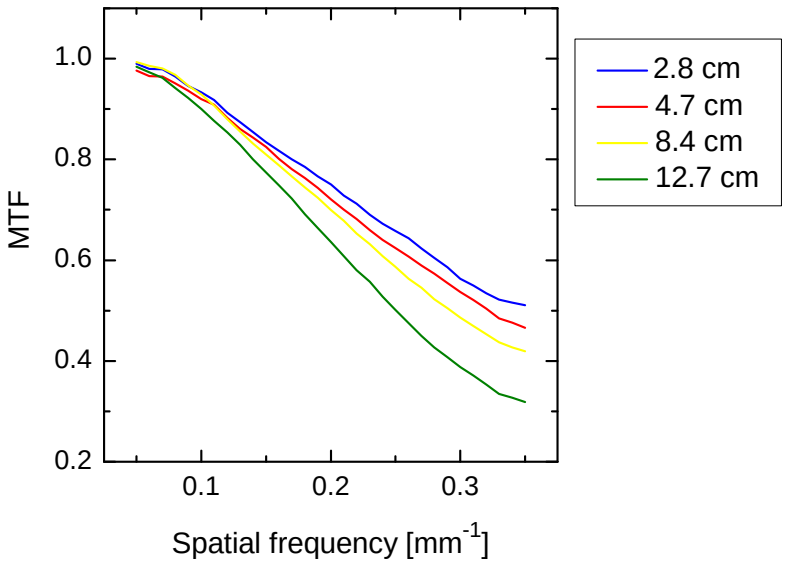

Figure 6.14: *MTF from the raw data for different wire - isocenter distances*

Noise

The NPS of the raw data is shown in Fig. 6.15 for different source voltages and currents. As expected, the NPS decreases with increasing source current. In order to quantify this effect, the average NPS is plotted against the source current on a double-logarithmic scale in Fig. 6.16a. The linear fits give a slope of about -1 for all source voltages. Noise in projection radiography is proportional to $1/\sqrt{N}$, where N is the number of photons. But the NPS is proportional to N^2 so that it is supposed to decrease linearly with $1/N$ [Han79]. This corresponds very well to the fitted slopes.

Figure 6.15 also illustrates that the NPS decreases with increasing source voltage. The dependence of the NPS on the source voltage is plotted in Fig. 6.16b. It is due to an increasing output of photons with an increasing source voltage. Simulating the spectra for different source voltages U on the central axis and integrating the number of photons N gave a proportionality of $N \propto (1 + \exp^{-\frac{U}{c}})^{-1}$, where c is a constant. Since the NPS is proportional to N^2, it is supposed to decrease with $\exp^{-U/c}$. This corresponds very well to the data, which can be fitted with an exponential decay function.

Noticeable in Fig. 6.15 are the peaks for high voltage and high current settings at the spatial frequencies 0.089 mm^{-1}, 0.177 mm^{-1} and 0.266 mm^{-1}. These frequencies correspond to 11.2 mm, 5.6 mm and 3.8 mm and accordingly to 8, 4 and 2.7 times the pixel size. Allowing

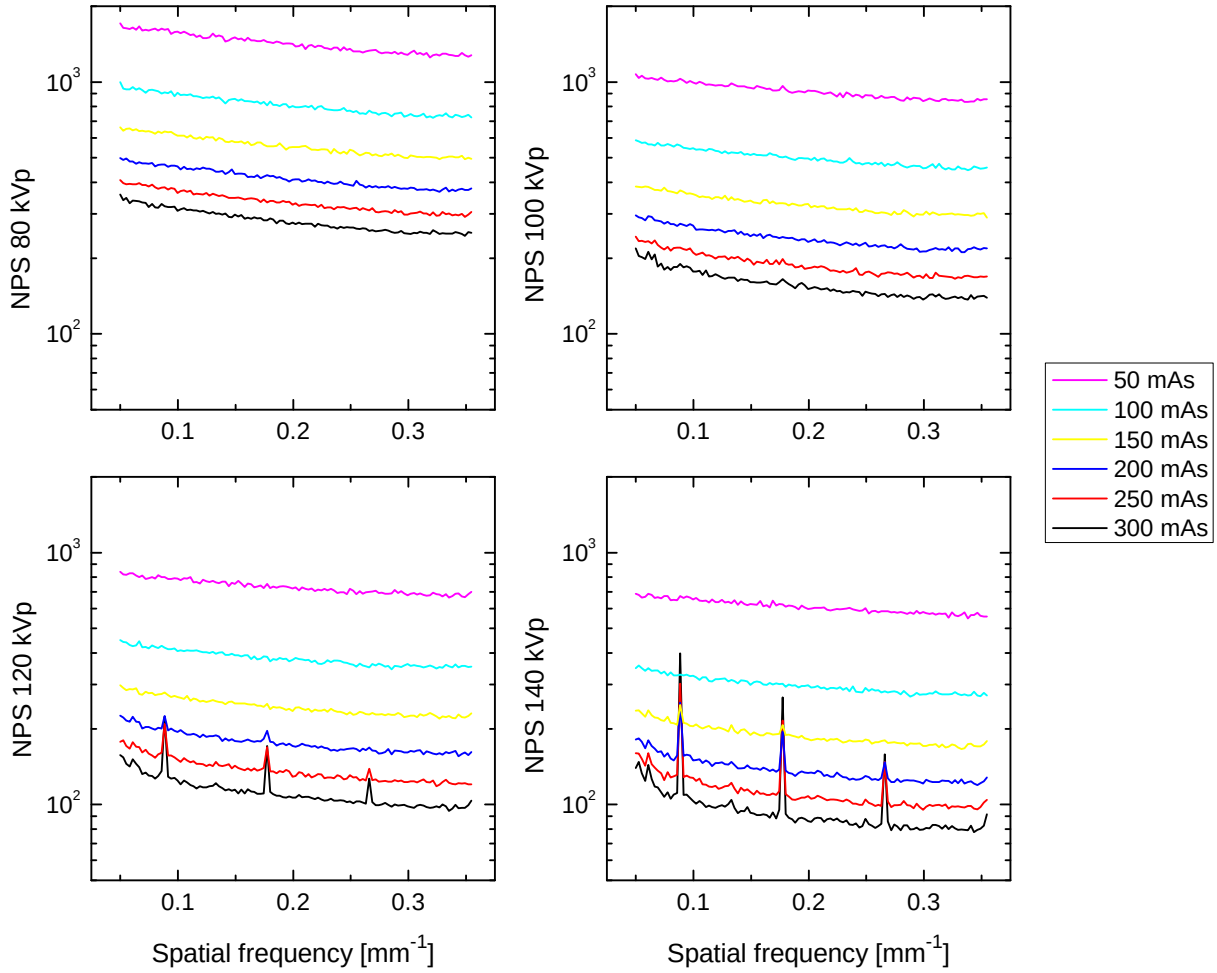

Figure 6.15: *NPS from the raw data for different source voltages and currents*

for small deviations due to averaging, the peaks have about the same height. For lower voltages and currents, they are not visible in the plots but masked by the quantum noise. If the peaks are effects of some kind of structure, first averaging over all rows and then calculating the Fourier transform should increase their height. Tests showed however that the relative height of the peaks stays the same. Further tests proved that the trend removal with a second order polynomial does not have any effect on the peaks. Whether the correction is done for the whole row or only for the ROI and with which order polynomial is not influencing them. These results suggest that the reason for the peaks lies in the readout electronics. Siemens however only confirmed that they know about the reasons, but that they cannot reveal the answer with reference to the corporate secret.

The presented NPS corresponds to the noise in the center region of the fan beam. Due to the bow tie filter, the number of photons reaching the detector in an air scan decreases from the center to the peripheries. This can be seen in the NPS, if it is calculated from a ROI on the edge of the detector. The comparison shows that the NPS at the peripheries is about 3.7 times higher than in the center, independent of the side of the detector.

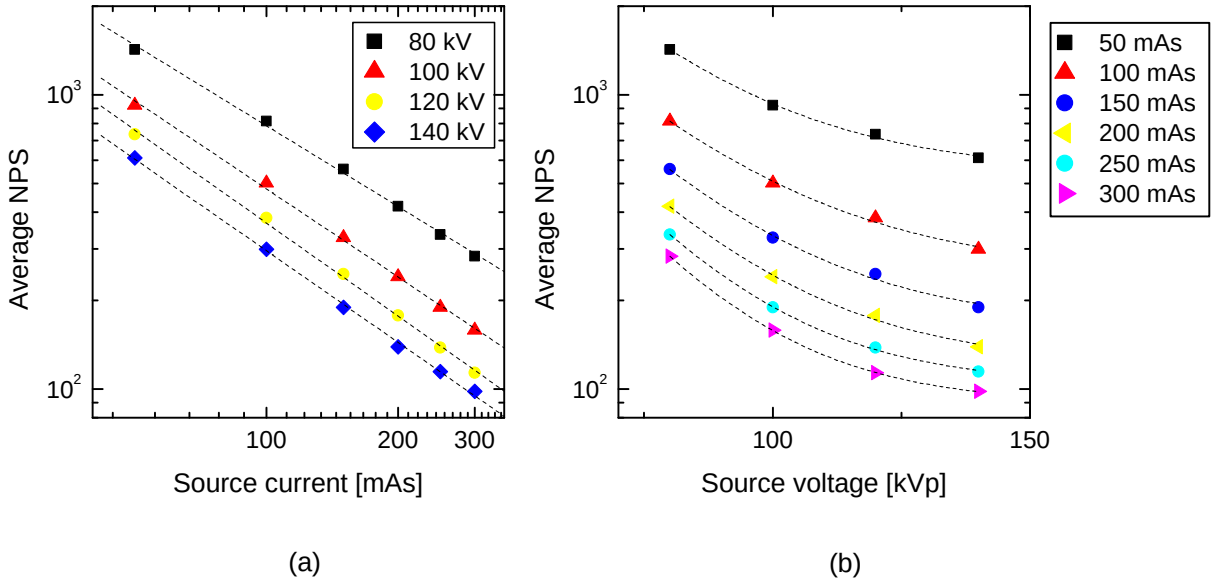

Figure 6.16: *Dependence of the NPS on the source current (a) and the source voltage (b). Linear (a) and exponential (b) fits are shown as dashed lines.*

The results presented in this section demonstrated that it is possible to analyze the hardware of a CT scanner by calculating the MTF and the NPS from the raw data. The results corresponded very well to the theories for spatial resolution and noise in projection radiography. The presented algorithms are both designed to work as well with data from the CT d'Or technology. The raw data obtained with the demonstrator are however not suitable for a proper analysis. This depends mainly on the small number of detectors which produce a sinogram of only about 67×197 pixels. The second reason is the unequal size of windows and shieldings, which results in different effective pixel sizes.

A drawback of this method is however that the readout of CT raw data is very complicated, since the actual structure varies not only between different manufacturers, but also between different models of the same manufacturer. A new readout program would have to be written for every scanner, which would be nearly impossible without information that is subject to a corporate secret.

6.2.2. Reconstructed images

Spatial resolution

The PSF curves of the clinical CT system were fitted following the procedure described in Sec. 4.2. Figure 6.17 shows the fitted PSF curves for the different reconstruction filters and Table 6.1 lists the corresponding parameters. As expected, the full-width-at-half-maximum (FWHM) of the peaks correlates with the sharpness of the filter: the more edge-enhancing the filter, the narrower is the PSF and the higher is the peak amplitude.

But even though the PSF curves were derived from images of the same object, the area under the 2-dimensional PSF is not equal for the different filters but decreases with increasing sharpness of the filter. We checked that this trend is not only a result of the fitting, but can also be found in the original measured images.

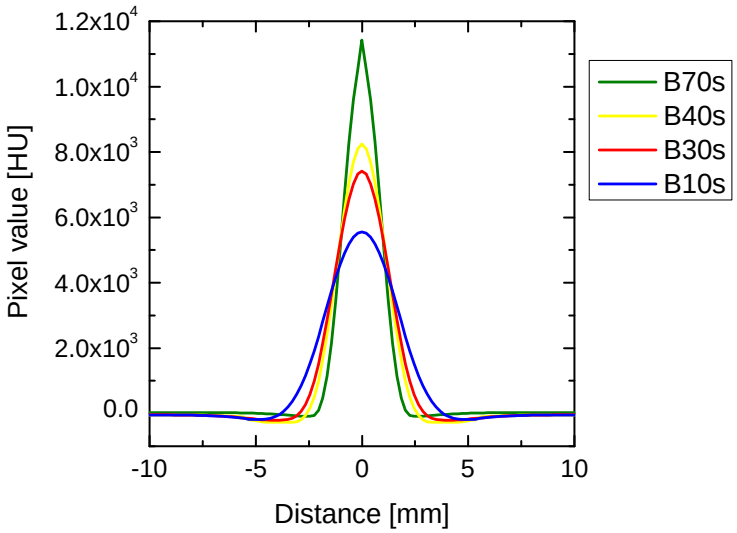

Figure 6.17: *Fitted PSF for the different reconstruction filters*

Table 6.1: *Parameters of the fitted PSFs. Filters are ordered with increasing sharpness.*

Filter	FWHM [mm]	Maximum value [HU]
B10s	7.3	5561
B30s	5.6	7419
B40s	5.0	8244
B70s	4.0	11430

Figure 6.18 shows the singular values of the $\mathbf{H}$ matrix (a) and the MTF (b) for the different reconstruction filters. The curves have different absolute values, because the MTF is normalized to one at zero frequency according to the IEC norm for projection radiography [IEC03], while the singular values are normalized such that the singular vectors are orthonormal. The MTF at a specific frequency is the magnitude with which a 2-dimensional cosine wave function of the same frequency is transferred through the imaging system, while the singular values correspond to the magnitude with which the systems singular vectors are transferred through the imaging system. Due to the normalization of the MTF at 0 frequency, the MTF of B10s, B30s and B40s have values higher than 1. This does not mean that the amount of information is higher on the output of the system than on the input. The smooth kernels seem to suppress the very higher frequencies, while the sharpest kernel has higher MTF at the larger frequencies.

For both approaches holds that the smoother the filter the lower the integral of the corresponding curve. But ranking the maximum values gives a different picture: B40s has the high-

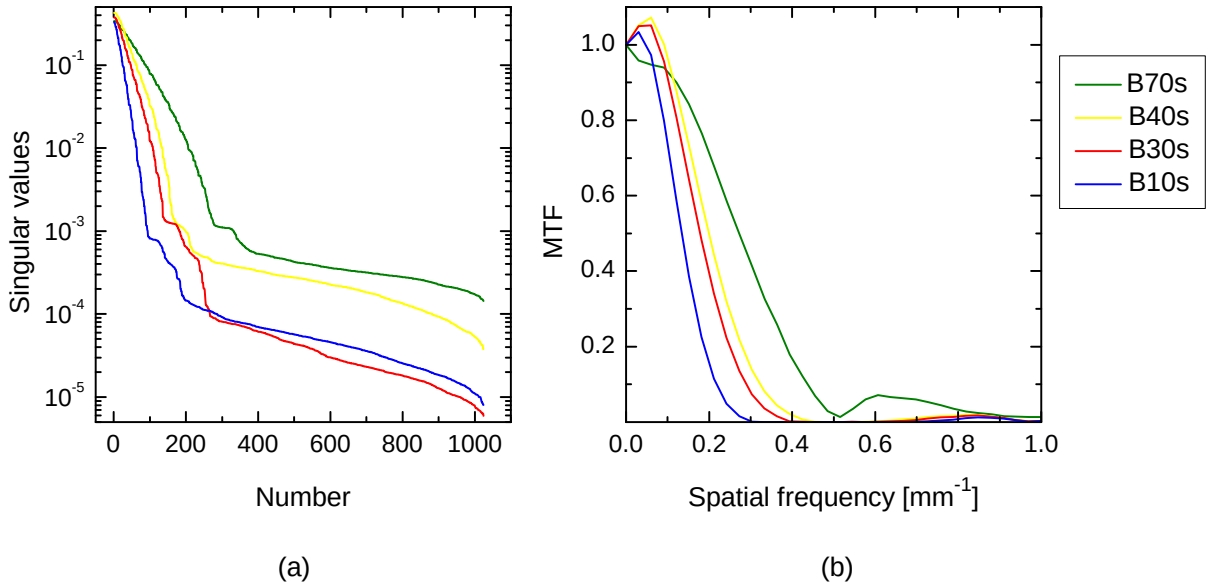

Figure 6.18: *Singular values of the H-matrix (a) and the corresponding MTF (b) of the clinical scanner. Please note that the scaling on the y-axes is not equal.*

est maximum value (0.43, 1.07) for both approaches, followed by B30s (0.37, 1.05), while the maximum values of the smoothest and the hardest filter, B10s (0.33, 1.03) and B70s (0.34, 1), are almost equal.

The spatial resolution is higher according to the Fourier approach than to the spatial approach, because of the strong decrease of the singular values of the $\mathbf{H}$ matrix compared to the MTF.

The simulated signal transfer of a disk with a diameter of 2 mm and an amplitude of 50 HU proves this assumption. The image in the top left corner of Fig. 6.19 corresponds to B10s, top right to B30s, bottom left to B40s and bottom right to B70s. All images of one approach are normalized to the maximum of the four images. The signals transfered by the H-matrix show a clear relation with the smoothness of the filter. The signals transfered by the MTF are much more similar for the different filters, though a trend from a smoother to a sharper signal is still visible. The images obtained from B30s and B40s are hardly distinguishable due to the very similar MTF curves. For all filters, the resolution predicted by the Fourier approach is higher than that predicted by the image-space approach.

In order to evaluate which approach gives a better description of the imaging system, images of a 3 mm Teflon pin were used, gained from the slice geometry and sensitometry module of the Catphan®phantom [Cat06]. A 32×32 pixel region was cut out of the reconstructed image around the pin. A disk with the same diameter and an amplitude of 990 HU corresponding to Teflon was simulated. The H-matrix and the MTF were applied to it and measured noise was added. The resulting images were then compared to the measured image of the Teflon pin (Fig. 6.20). The example of the B30s filter at 10.47 mGy shows that the real image is between the images generated with the H-matrix and the MTF: It is less blurred than the image generated

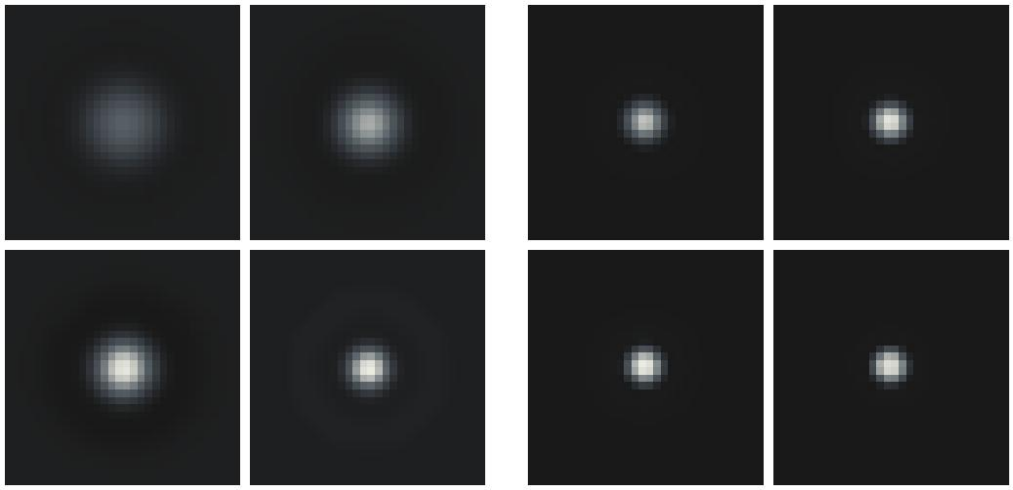

(a) (b)

Figure 6.19: *Signal transfer as predicted by the image-based approach (a) and the Fourier approach (b). The top left image respectively corresponds to B10s, top right to B30s, bottom left to B40s and bottom right to B70s.*

with the H-matrix, but it is not as sharp as the image generated with the MTF. The profiles of the transfered signals in Figure 6.21 confirm this statement. For all filters, the amplitude predicted by the Fourier approach considerably exceeds the amplitude of the measured signal and the FWHM is smaller than the measured one. The MTF therefore systematically overestimates the performance of the imaging system. For B10s and B30s, the amplitude estimated by the spatial approach is lower and the FWHM is larger than the original, resulting in an underestimation of the system performance. For B40s and B70s, however, the amplitude calculated with the **H** matrix is very close to the measured amplitude, providing a considerably better description of the signal transfer than the Fourier approach.

(a) (b) (c)

Figure 6.20: *Measured image of a 3 mm Teflon pin of the Catphan®phantom acquired with 10.47 mGy and reconstructed with B30s (a). The corresponding simulated signal generated with the H-matrix (b) and with the MTF (c).*

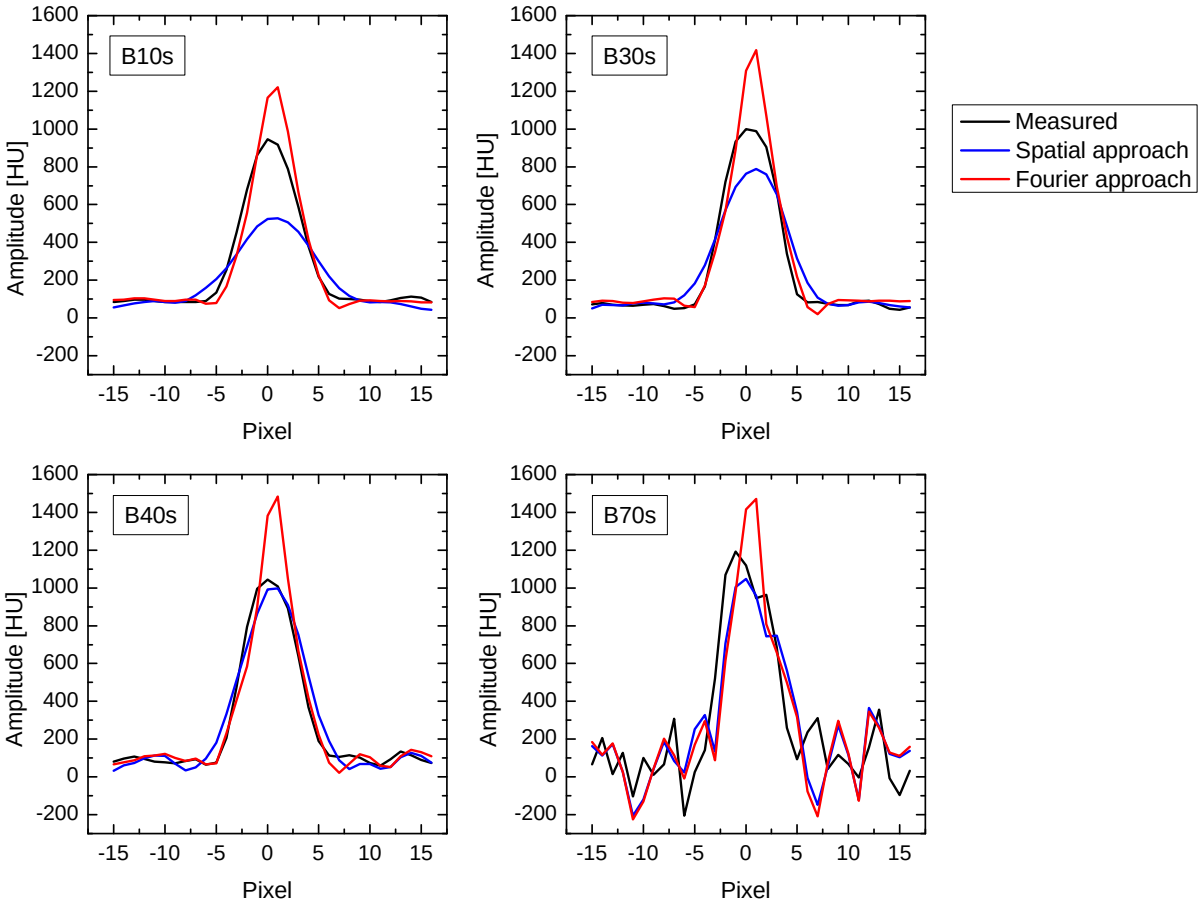

Figure 6.21: *Profiles of the transfered 3 mm Teflon pin*

Noise

The first 25 eigenvectors of the covariance matrices for the different filters at 10.47 mGy are shown in Fig. 6.22 sorted with decreasing magnitude of their corresponding eigenvalues. Since the structure of the noise depends on the filter and only the height of the noise depends on the dose, the eigenvectors look rather similar for different dose settings so that only 10.47 mGy is shown here. The pattern is larger for smoother filters, while it is very small-structured for B70s.

The eigenvalues of the covariance matrix are presented in Fig. 6.23 by using again the example of 10.47 mGy. For a quantitative comparison also the values of the 2-dimensional NPS sorted in descending order are inserted. As expected, the smoother the filter, the lower is the noise in the images. The sharpest filter B70s, however, produces considerably more noise in the images than the other filters. Although, particularly, the higher numbers are quite different for the two approaches, the difference of the integrals was for all calculated curves less than 10^{-3} HU^{2}mm^2. Therefore, the total amount of noise is described similar by both approaches.

The dependence of the 1-dimensional NPS on the filter and on the dose is shown in Fig. 6.24 using the example of 10.47 mGy (a) and B30s (b) respectively. For an increasing sharpness of the filter not only the height of the curve increases, but also the shape changes toward a bump in

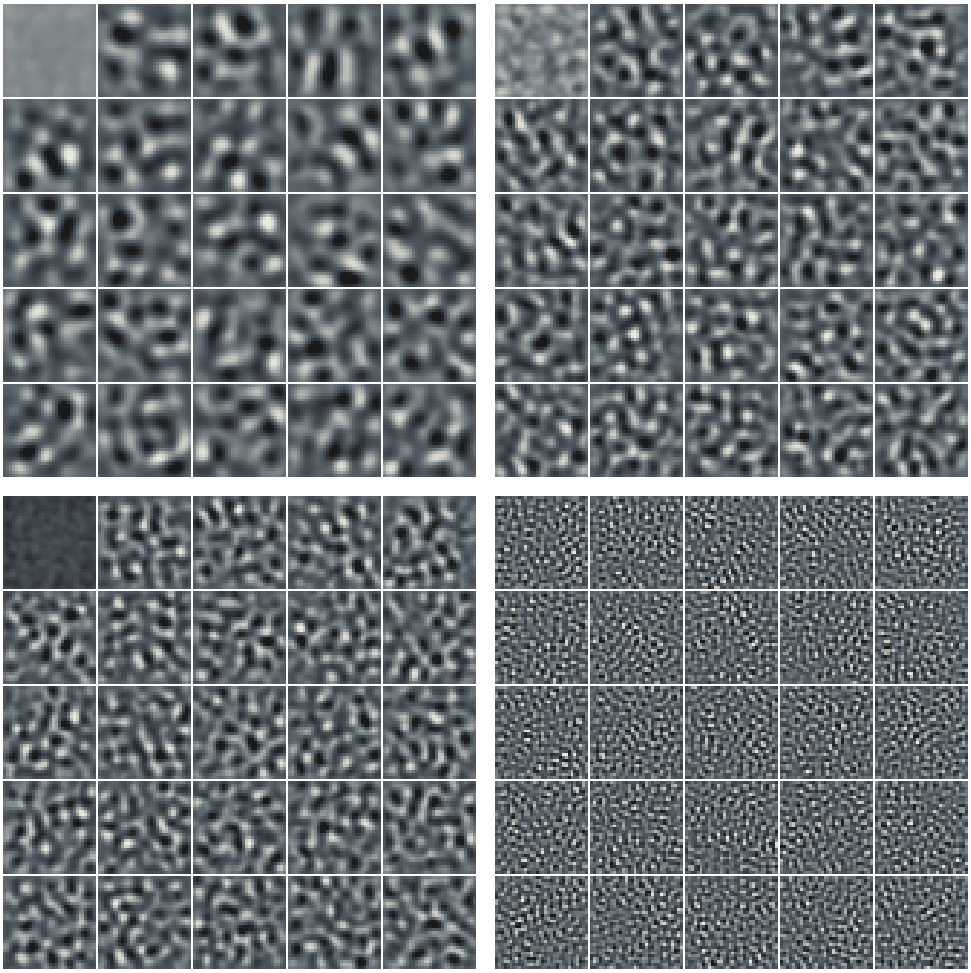

Figure 6.22: *First 25 eigenvectors for the different reconstruction filters at 10.47 mGy: top left B10s, top right B30s, bottom left B40s and bottom right B70s.*

the mid-frequency range. For different dose settings, the shape is the same, but the magnitude of the noise decreases with increasing dose.

Location-specific noise

In the same way as for the FDA system, the images of the clinical CT scanner were divided into 9 square regions and their individual covariance matrices were calculated and analyzed. The 1st eigenvectors at the position of their corresponding regions are shown in Fig. 6.25. The eigenvectors of B10s have a broad and smooth structure, which gets finer with an increasing sharpness of the filter. B30s, B40s and B70s have an indistinct starlike pattern, which is visible but by far not as clear as for the FDA system. By contrast, B10s shows no starlike pattern at all, but the structure of the noise seems to be the same for the whole image.

The dependence of the magnitude of noise is shown for the extreme filters B10s and B70s in Fig. 6.26. In accordance with the similar eigenvector patterns for B10s, the corresponding eigenvalues depend little on the location. The magnitude of noise is sensitive to the location when sharper filters are applied, showing the largest difference for B70s. Since dividing the

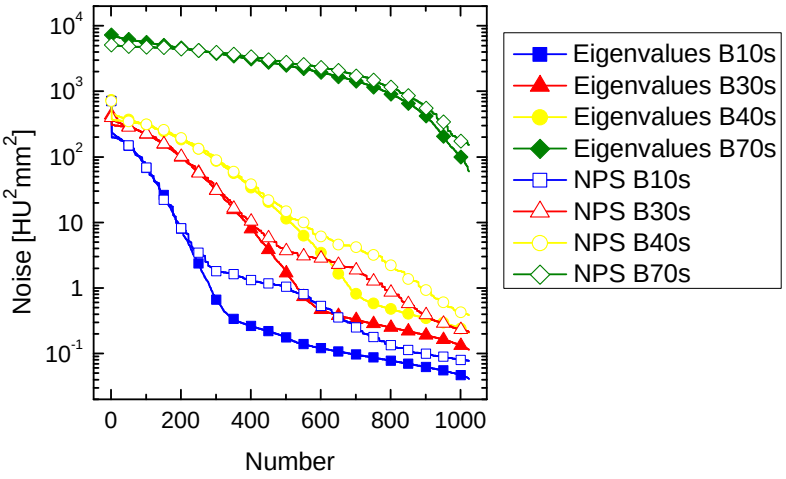

Figure 6.23: *Eigenvalues and the values of the 2-dimensional NPS sorted in descending order for 10.47 mGy.*

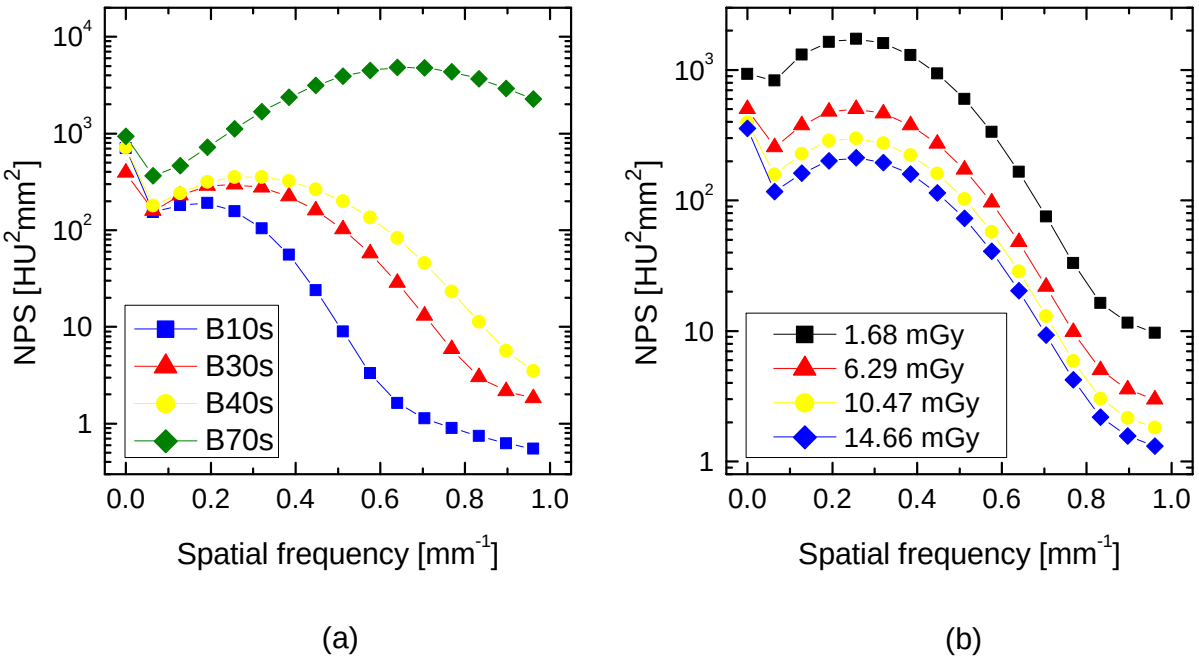

Figure 6.24: *Variation of the NPS in dependence of the filter at 10.47 mGy (a) and of the dose at B30s (b).*

266 × 266 pixel water region in 9 square regions resulted in only 840 ROIs for all 210 slices, only 840 eigenvalues of the covariance matrix could be defined. The remaining eigenvalues were essentially zero so the the covariance matrix did not have full rank and was therefore not invertible (compare Sec. 6.2.2).

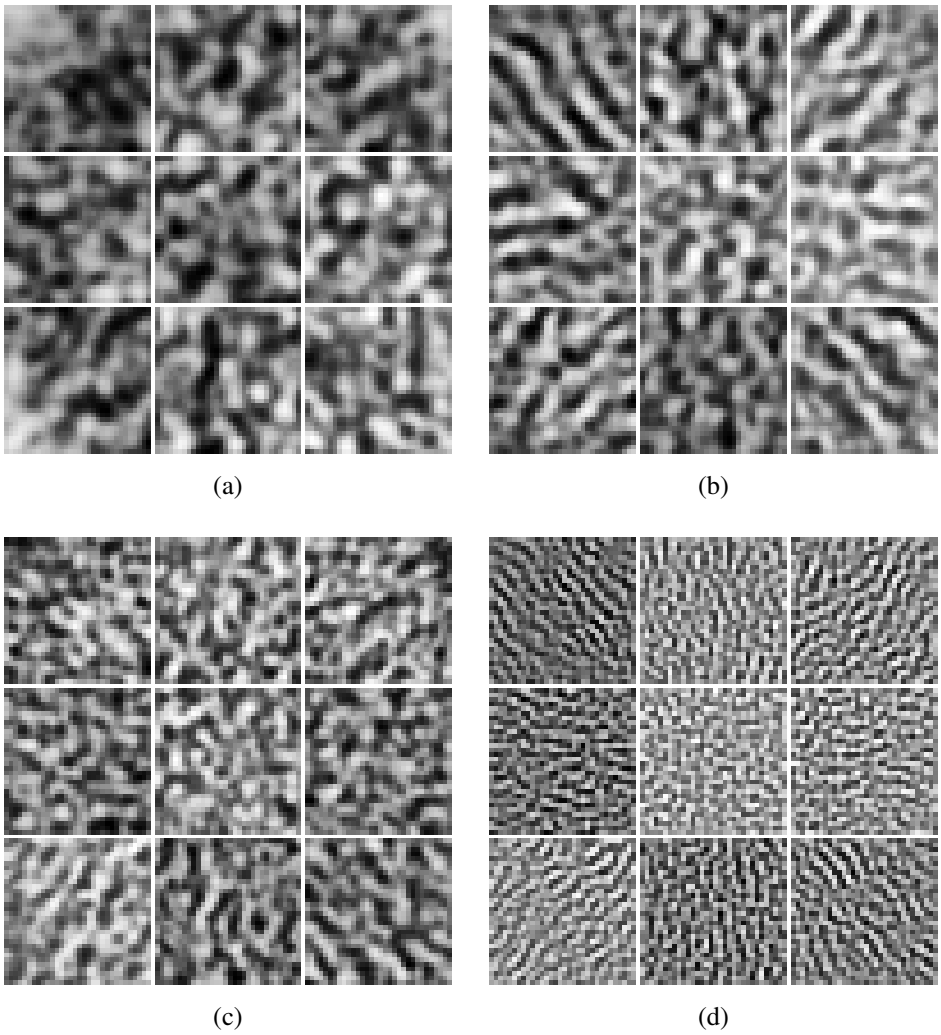

Figure 6.25: *1st eigenvectors at the position of the corresponding regions for 10.47 mGy: top left B10s, top right B30s, bottom left B40s and bottom right B70s.*

SNR

Comparison of the SNR

The SNR for the simulated disk (diameter 2 mm, amplitude 20 HU, background -30 HU) is shown in Figure 6.27 for the spatial (a) and the Fourier (b) approach. The spatial SNR is smaller due to a worse spatial resolution calculated from the $\mathbf{H}$ matrix than from the MTF. The Fourier SNR has about the same values for the filters B30s and B40s. Almost equally suited is B10s, but B70s is considerably worse. For the spatial approach, B40s is clearly better than B30s. Notice that B70s exceeds B10s. This is a very interesting example of how the filters are described by the different approaches: while the spatial SNR clearly favors B40s for this task, the Fourier SNR rates B30s and B40s equally and B10s is evaluated to be not much worse. Comparing these results with Figure 6.20 and Figure 6.21 leads to the conclusion that for the harder filters, B40s and B70s, the spatial SNR is expected to be more realistic than the Fourier

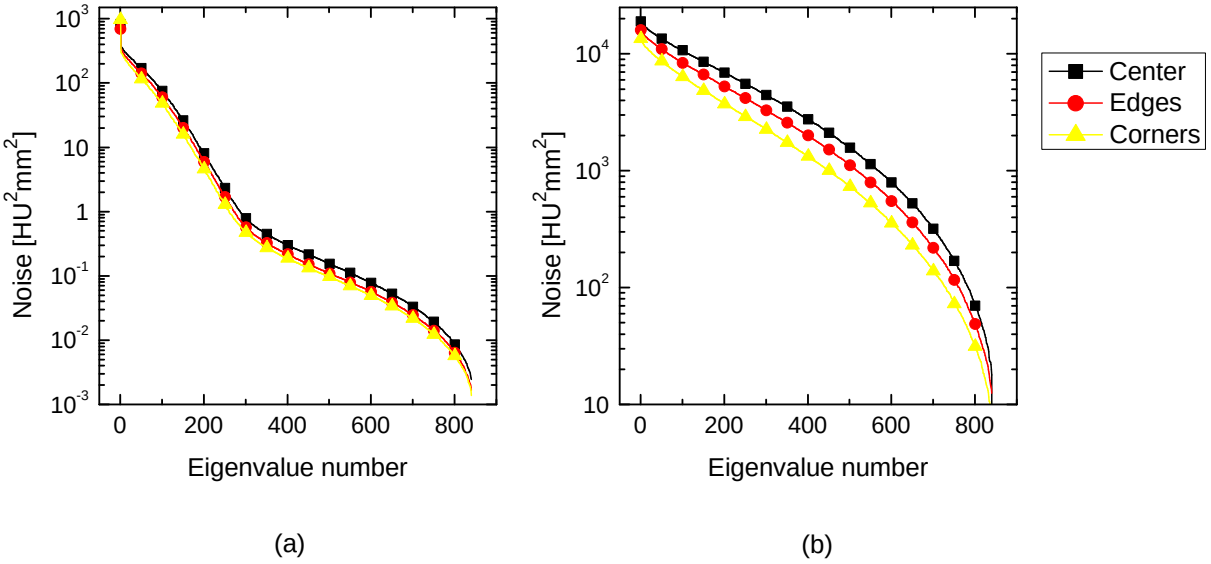

Figure 6.26: *Location-specific eigenvalues for B10s (a) and B70s (b).*

SNR. For the smoother filters, B10s and B30s, the real SNR lies probably in between the two approaches.

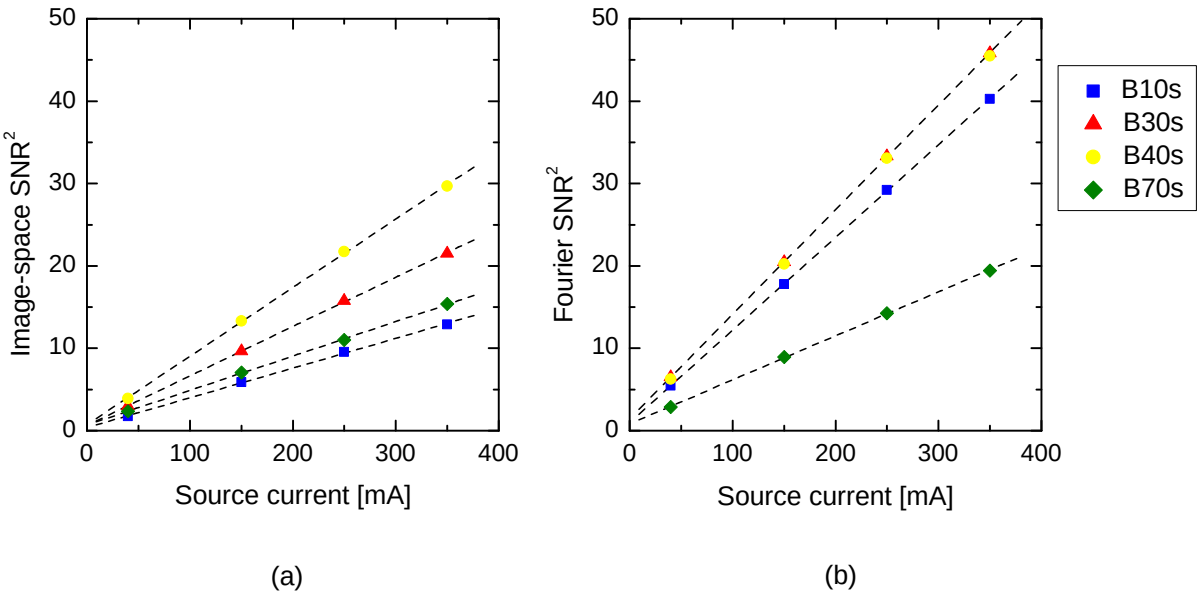

Figure 6.27: *SNR for the simulated disk for the image-space (a) and the Fourier (b) approach. Linear fits for the data are shown with black, dashed lines.*

Comparing these results with Fig. 6.20 and Fig. 6.21 leads to the conclusion that the real SNR lies in between the two approaches, but is for B40s probably closer to the image-space SNR.

Bootstrapping calculation

The water region of the 210 slices taken with the clinical CT scanner had a size of 266×266 pixels. Dividing this area into 32×32 ROIs with a spacing of 8 pixels (Sec. 4.2) gave 7560

ROIs in total. A bootstrapping calculation was performed (n = 1500, 2500, 5000 and 7500) for noise images taken at 10.47 mGy and reconstructed with B30s to check whether this number of ROIs was large enough to appropriately define the covariance matrix.

The standard deviation as well as the SNR decrease exponentially, approaching 0.034 and 4.21 respectively (Fig. 6.28). The image-space SNR, for which all 7560 available ROIs were used, was 3.97. The difference of 0.24 is produced by the random sampling with replacement, which is performed by definition for the bootstrapping calculation. It suggests that the number of ROIs was not enough for an appropriate definition of the covariance matrix so that the repeated contribution of some ROIs artificially decreased the noise. If there were enough ROIs, the replacement would not change the result and the SNR calculated with the bootstrapping method would converge to the image-space SNR as it did for the laboratory CT system. The image-space SNR is supposed to be closer to the real value, because of the good agreement of the integral of the eigenvalues with the integral of the NPS. The magnitude of the NPS is independent of the number of ROIs used for the calculation, but the more independent pixels are used, the less noisy is the NPS. The IEC norm [IEC03] requires at least 4 million independent image pixels for the calculation of the NPS. Since 7560 ROIs correspond to more than 7.7 million image pixels, the NPS is expected to be accurately determined.

When partitioning the images in 9 regions, only 840 ROIs could be created. Therefore, only 840 eigenvalues of the 1024×1024 covariance matrix were defined, while the remaining 184 eigenvalues were zero. The resulting matrix did not have full rank and was therefore not invertible as it would be necessary for the calculation of the SNR. The fits (Fig. 6.28) suggest a standard deviation of 27 % and a SNR of about 20; 476 % of the actual value. The corresponding eigenvalues are supposed to be about this factor lower than the real eigenvalues. Due to the high standard deviation, the comparison of the location-specific noise in Sec. 6.2.2 has to be interpreted with care.

6.3. CT d'Or combined with the clinical CT system

Since the methods elaborated in the previous chapters require a large number of images for the analysis, they could not be applied to the CT d'Or in combination with the C-arm device. Instead, the analysis had to be performed using images from the combination of the CT d'Or demonstrator with the clinical CT scanner, though Sec. 4.4 showed that the image quality has to be much lower. Therefore, the results presented in this chapter are not suited to demonstrate potential advantages of the CT d'Or geometry above conventional systems. This chapter is rather supposed to study the applicability of the image-space and the Fourier approach to new CT geometries such as the CT d'Or.

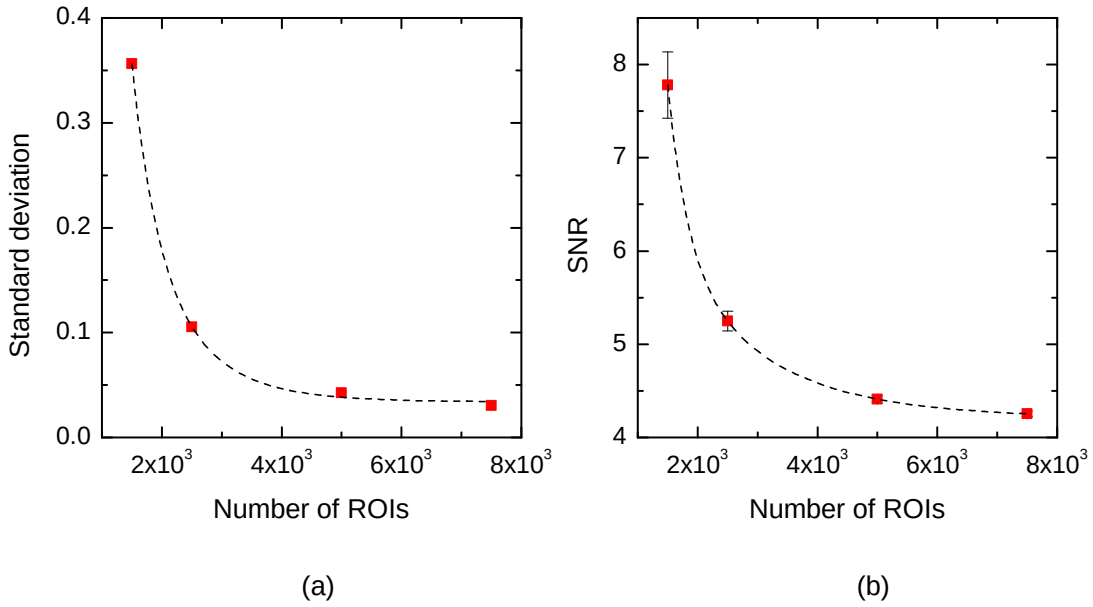

Figure 6.28: *Results of the bootstrapping calculations. The standard deviation (a) as well as the actual SNR (b) decrease exponentially.*

Spatial resolution

The spatial resolution was measured with a steel wire of 1.0 mm diameter at different distances from the isocenter. Figure 6.29 presents the fitted PSF curves for the three settings. The curves were normalized and only the values between -50 and +50 pixel are shown so that the very small differences between the peak shapes can be seen. The FWHM is the same for all curves, but the larger the distance to the isocenter, the smoother the transition from the peak to the tails.

This is also reflected in the lower singular values of the H-matrix (a) and in the MTF (b) in Figure 6.30. The closer the peak is to the isocenter, the higher is the MTF. Due to different noise

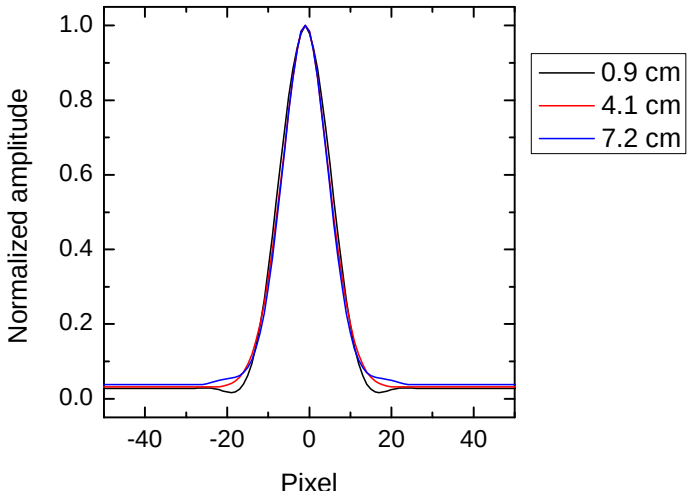

Figure 6.29: *Normalized PSF curves at different distances from the isocenter.*

patterns in different regions of the images (Fig. 4.19a), it can however not be excluded that this effect is just an artifact. Furthermore, the higher singular values behave in a different way. For 0.9 cm distance from the isocenter, the slope of the curve is steeper than for 4.1 cm and 7.2 cm, which decrease in about the same way. It is therefore expected that the image-space SNR is best for 4.1 cm, followed by 7.2 cm and 0.9 cm.

Notably is the abrupt drop-off after the first value of the MTF, which is due to the size of the wire. While the 0.08 mm wire used for the clinical CT was approximately a point object, the 1.0 mm wire used in the CT d'Or does not fulfill this criteria. A much thinner object can however not be detected by the CT d'Or demonstrator.

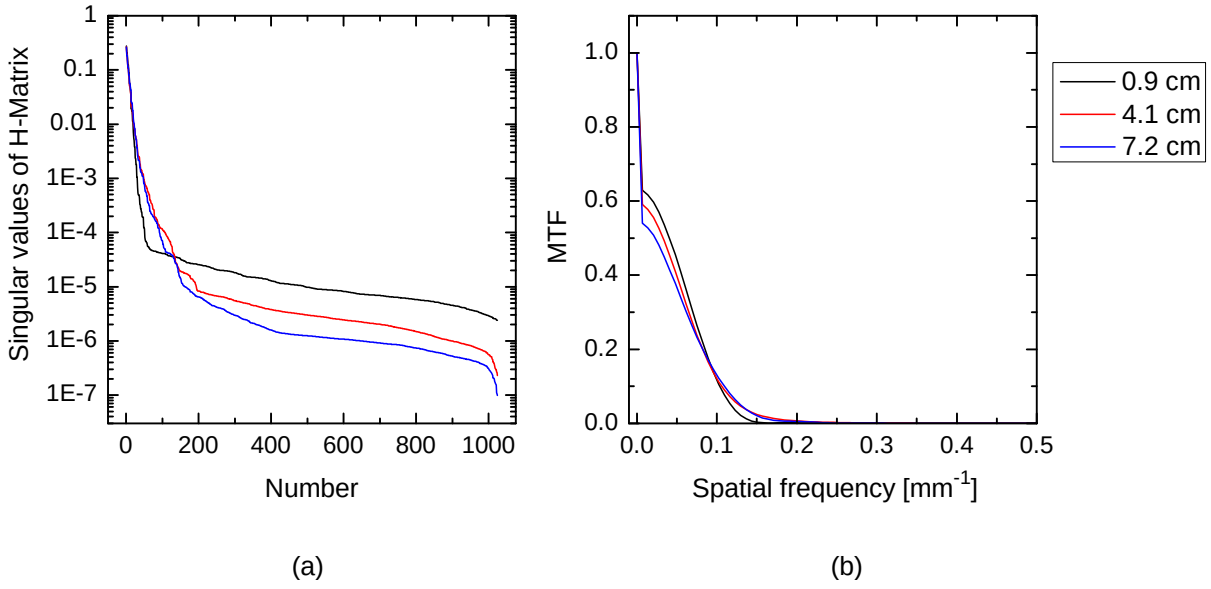

Figure 6.30: *Singular values of the H-matrix (a) and corresponding MTF (b)*

The size of the wire has however also its advantages, because it allows to use the image directly for a comparison of the signal transfer described by the two approaches. The wire was simulated as a disk with 1.0 mm diameter and the H-matrix and the MTF were applied to it respectively. Since the reconstructed image of the wire was not calibrated to HU, only the shape of the peak not the amplitude was compared. For this reason, no noise was added to the simulated images.

Figure 6.31 shows the measured image of the wire (a), the simulated signal generated with the H-matrix (b) and with the MTF (c). The real image is blurred quite similar to the image predicted by the image-space approach, while the Fourier approach predicts a much sharper image. This becomes even clearer when comparing the profiles of the images as it has been done in Fig. 6.32. The measured image is not symmetric, but the FWHM of the profile predicted by the image-space approach is only slightly larger in the original image, while the FWHM obtained with the Fourier approach is much smaller. This is unlikely to be due to an inaccurately defined MTF, since the MTF is supposed to get even better for thinner objects as its drop-off would disappear. For the CT d'Or, the image-space approach provides therefore a much

better description of the system than the Fourier approach, which considerably overestimates its performance.

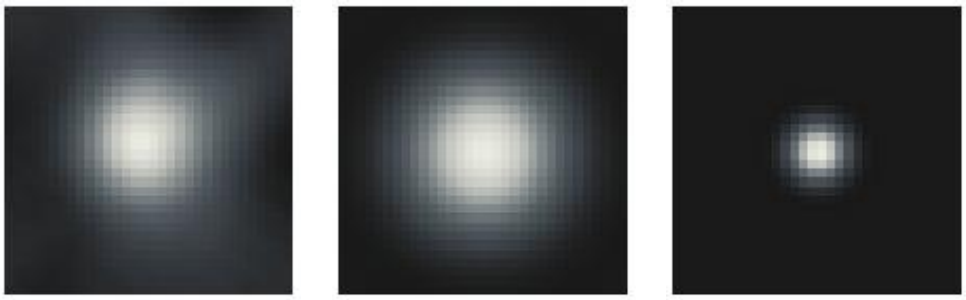

(a) (b) (c)

Figure 6.31: *Measured image of the 1.0 mm steel wire (a), the corresponding simulated signal generated with the H-matrix (b) and with the MTF (c).*

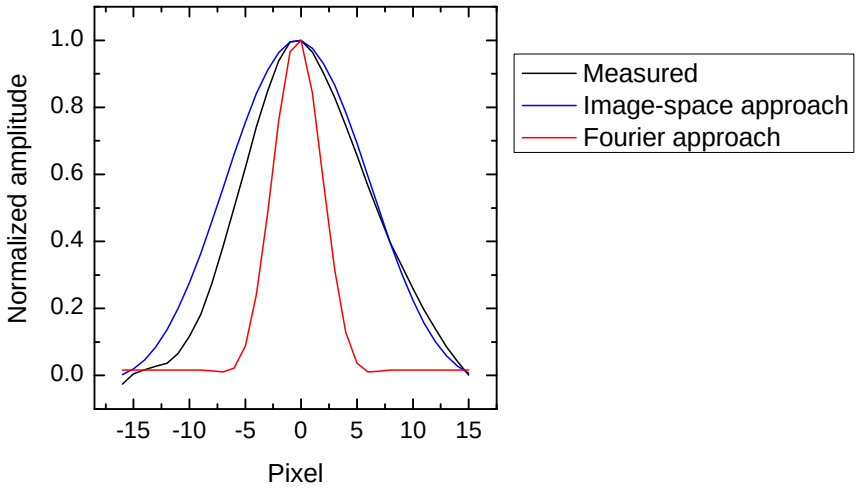

Figure 6.32: *Normalized profiles of the transfered 1.0 mm steel wire.*

Noise

Noise in CT d'Or images was determined from 30 images of a PMMA-slice, which were used to calculate the covariance matrix and the NPS. Figure 6.33 presents the first 64 of the 1024 eigenvectors of the covariance matrix sorted with decreasing magnitude of their corresponding eigenvalues. The dominating eigenvectors differ considerably from the eigenvectors of the other systems as well as from exponential wave functions, since they have very large, but quite regular structures. They probably describe the noise produced by the artifact patterns in the images. Starting at about eigenvector number 34, the structure becomes similar to the eigenvectors of the other systems. This example shows that the image-space approach provides a convenient method for the characterization of the noise structure in new CT geometries such as the CT d'Or.

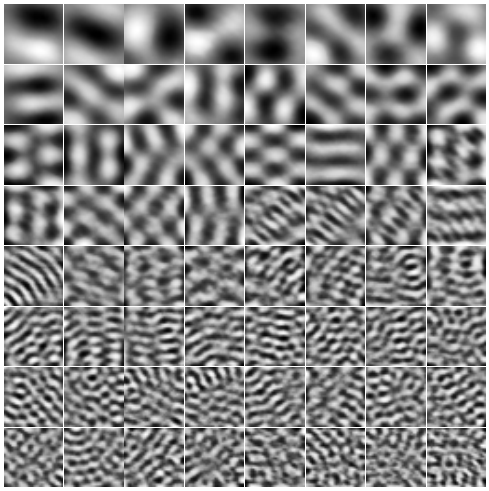

Figure 6.33: *First 64 eigenvectors of the covariance matrix*

Figure 6.34a shows the eigenvalues of the covariance matrix and the values of the 2-dimensional NPS sorted in descending order. The curves differ considerably from each other, and, in contrast to the other systems, the integrals of the curves do too. The sum of the NPS values is more than double the sum of the eigenvalues. This corresponds to the results of the bootstrapping calculations which revealed that the noise is underestimated by the image-space based approach, when not enough ROIs were used to calculate the covariance matrix.

The 1-dimensional NPS in Figure 6.34b has its maximum at low frequencies and subsequently decreases without a bump in mid-frequency range, because no edge-enhancing filter was used for the reconstruction.

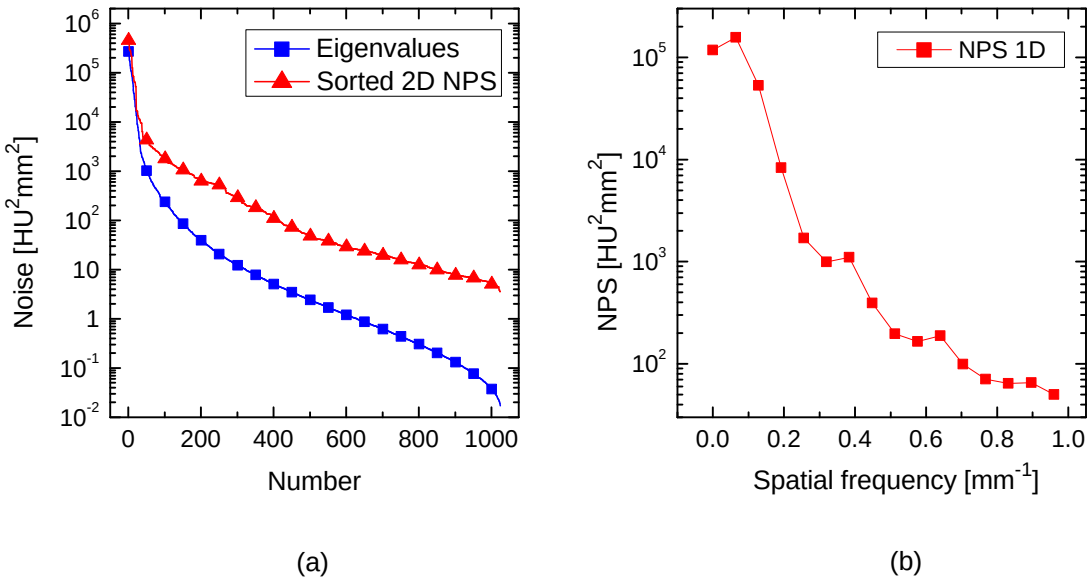

Figure 6.34: *Results of the noise analysis of the CT d'Or images: (a) Eigenvalues of the covariance matrix and values of the 2-dimensional NPS sorted in descending order and (b) the 1-dimensional NPS.*

SNR

Figure 6.35 gives the SNR for the CT d'Or at different distances from the isocenter. As expected from the results for the spatial resolution, the Fourier SNR decreases with increasing distance from the isocenter, while the image-space SNR does not have a trend, but follows the order predicted by the singular value curves of the H-matrix.

In this specific case, the measured image-space SNR is larger than the Fourier SNR. The results of the bootstrapping calculations for the other systems demonstrated however that this is only due to the small number of ROIs used to calculate the covariance matrix. In order to correct for this effect based on the bootstrapping calculations for the clinical CT system (Sec. 6.2.2), the measured image-space SNR has to be divided by 1.9 resulting in a corrected image-space SNR that is again smaller than the Fourier SNR (Fig. 6.35).

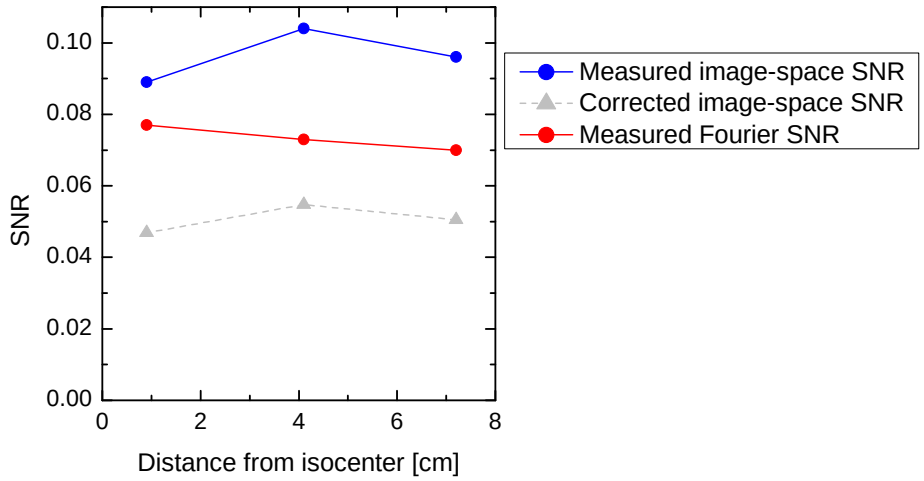

Figure 6.35: *SNR for the CT d'Or demonstrator in combination with the clinical CT. Besides the measured SNR for both approaches, also the corrected image-space SNR is shown.*

The analysis of the noise and the SNR can therefore only be a proof-of-principle that the image-space approach can be applied to the images obtained with the CT d'Or device. But since their quantitative information is known to be biased, the absolute values have to be interpreted with care.

7. Conclusions and Outlook

This work dealt with the development and experimental implementation of a physical concept for quality assurance of new CT methods with a special focus on the CT d'Or technique. Besides dose measurements this was achieved by applying the conventional Fourier methods as well as by introducing a completely different image-space based approach.

The Fourier approach is a well-established method which is commonly applied to CT images. The details in data treatment however still vary widely between different studies. The data processing developed for this work has been proposed to the IEC in September 2010 to become common standard[1]. A final decision has not been made till the completion of this work, but since it passed the initial survey, there is a good chance that the presented methods will be part of the next editions of the IEC norms about image quality in CT scanners.

Although normally only applied to reconstructed images, in this work the Fourier methods were also used for the analysis of CT raw data in order to separate the quality of the hardware from the reconstruction. In contrast to former studies, the data processing was especially developed with regard to the application to new CT methods, such as the CT d'Or concept. The measurement methods were designed to be simple and suitable for every CT geometry. The resulting MTF and NPS provided information about the scanner system additional to the information obtained from common analysis of the reconstructed images.

Even though the Fourier methods are well-established with digitalized systems, they make assumptions, such as shift-invariance and wide sense stationarity, which are not fulfilled by real CT scanners. In order to determine the errors introduced by nevertheless applying them, an image-space based approach was presented in this work, which is pixel based and therefore well-suited for reconstructed images. As the first comprehensive application of this approach to CT, the experimental implementation and the data treatment had first to be developed using known scanners. Once accomplished, a comparison of the results to the Fourier based approach revealed the similarities and differences. Despite the eigenvectors and eigenvalues not being equal, the magnitude of noise turned out to be the same for both approaches, for the laboratory and the clinical CT system. The spatial resolution was however considerably different for the two approaches, because the H-matrix actually blurs a simulated input signal much more than the MTF. A comparison with real images revealed that the MTF tends to overestimate the performance of an imaging system, while the H-matrix tends to underestimate it. But for some

[1] Proposed Amendment for IEC 61223-3-5 Ed. 1[IEC04] and IEC 61223-2-6 Ed. 2[IEC06] by Iacovos S. Kyprianou and Stanley H. Stern

cases, the image-space approach actually provides a reasonable description of the signal transfer. Since the SNR is based on the noise and the spatial resolution, it is always higher for the Fourier approach than for the image-space approach. From the comparison with real images, the actual SNR of the system is supposed to lie in between the image-space SNR and the Fourier SNR.

The application of the image-space approach to various CT systems revealed also its advantages and disadvantages. Its major advantage is that it is directly applicable to digitalized systems, because it is pixel based and it models the system properties with matrix operators. The assumptions necessary for Fourier transformation do not have to be made. The optimized eigenvectors give additional information about the structure of the noise and the spatial resolution is sometimes predicted more realistically by the H-matrix than by the MTF. Therefore, this approach has the potential to provide a better description of the imaging system than it is possible with the Fourier approach.

But the analysis in image-space involves also disadvantages, because neither spatial resolution nor noise can be assigned to their corresponding spatial frequencies. This is however an important information, especially as both MTF and NPS do not necessarily decrease linearly. Another drawback is the high measurement and computational effort, which is required to get enough data and analyze them appropriately. Instead of $4 \cdot 10^6$ independent pixels needed for the NPS according to the IEC [IEC03], the bootstrapping calculations in this work showed that at least 10^7 independent pixels are necessary for a proper description of the covariance matrix and that less pixels lead to a highly biased SNR. Taking enough images is a time-consuming process even for completely automated systems such as the clinical CT, but for the CT d'Or demonstrator it was impossible. Furthermore, the computational effort for the analysis according to the image-space approach is enormous. Although ROIs of the minimum reasonable size of 32×32 pixels were used, the calculation of the covariance matrix took several hours and the analysis of the resulting 1024×9216 H-matrix overran the capacity of a standard computer. For comparison, the MTF and the NPS can be calculated in seconds on the same computer. To handle larger ROI sizes, which would provide a better resolution, a high-capacity computer would be needed.

These drawbacks make it impossible at present to include the image-space approach into daily routine of quality assurance. Nevertheless, analyzing each system at least once with the image-space approach can give important additional information. The error implemented by the assumptions of the Fourier methods can be shown to be negligible as for the noise in the laboratory and the clinical CT system. But also discrepancies can be revealed between the spatial resolution predicted by the MTF, the H-matrix and the actual value. Detecting the limitations of the conventional methods can then help to account for them in daily routine.

This was first demonstrated with the improved version of the CT d'Or demonstrator in combination with the clinical CT system. In order to get as good images as possible, new algorithms for data treatment had to be developed first. The application of the new algorithms on a data set

sampled with the C-arm device and the comparison with images processed with the former software demonstrated the improvement of image quality achieved. For the combination of the CT d'Or with the C-arm device, remarkably good images could be produced, considering the drawbacks of the demonstrator. Due to a drastic decrease of sampling time and number of views, the image quality was much worse when combining the CT d'Or ring with the clinical CT. The resolution was decreased, the noise was considerably higher, and the data sampling implemented a regular pattern in the images. The resulting noise was biased low for the image-space approach, because not enough independent pixels were available for an appropriate analysis. Since only one slice is acquired by the CT d'Or demonstrator, no oversampled PSF was measured for the determination of the spatial resolution. Furthermore, the high noise and the patterns in the images introduced severe uncertainties in the results for the spatial resolution. Independent of the approach used, the analysis of the image quality has emphasized the major disadvantages of the CT d'Or demonstrator.

However, the measured dose reduction of more than 60 % justifies to follow up the concept of CT d'Or. But before a clinical prototype can be manufactured, several issues have to be considered. The ring must have a diameter of about 70 cm to be large enough for a human body and the number of detectors has to be increased to at least 1000 in order to achieve an adequate resolution. This gives a maximum width of the mask detectors of 1.1 mm. Furthermore, for a straightforward combination of the data sets, the mask detectors should have a sensitivity similar to the arc detector. This defines for a given material a minimum thickness of the detector. The shieldings must account for this, but they must not be much broader than the detectors. A probably resulting decrease of the thickness could be countervailed by replacing lead by tungsten or rhenium, which have higher densities than lead and hence a higher absorption.

These considerations recently led to the introduction of a modified version of the CT d'Or geometry. Instead of the mask detectors on the inner side of the shieldings and the arc detector outside the ring, it works with only one arc detector inside the ring, which collects both data sets simultaneously. This solves potential problems with the thickness of the mask detector and the smaller thickness of the shieldings. The modified CT d'Or is not an additional ring in an otherwise conventional CT system anymore, but an independent new CT technology. A prototype for a micro-CT system is under construction in order to investigate its potential and finally clarify if the theoretically predicted advantages of the CT d'Or geometry can be achieved in reality.

A. Mathematics for the reconstruction of the CT d'Or data

A.1. CT d'Or combined with the C-arm device

A.1.1. Data of the C-arm device

The calculations were done based on the coordinate system defined in Fig. A.1.

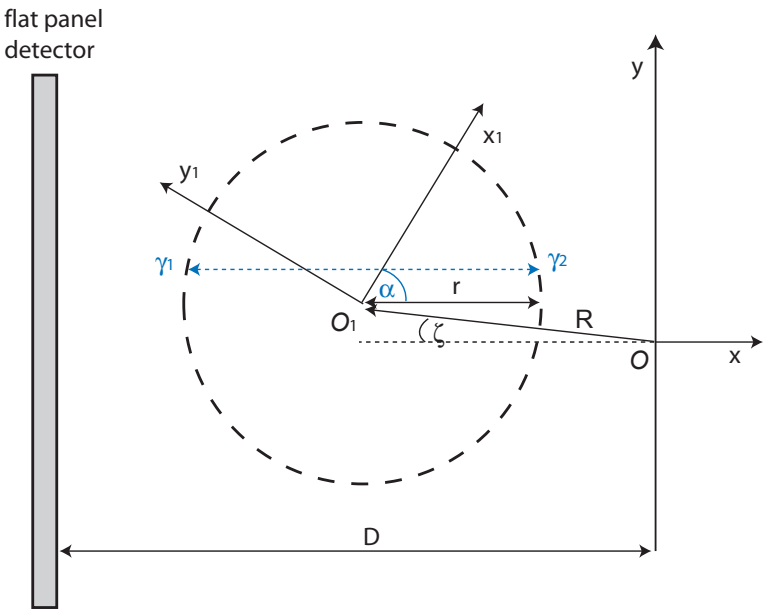

Figure A.1: *Coordinate system in C-arm device*

The reference system $Oxyz$ is defined by the origin O, which coincides with the source, a vector Ox normal to the detector, a vector Oy parallel to the detector, the central plane Oxy and a vector Oz normal to the central plane (not shown in the figure).

Let $O_1x_1y_1z_1$ be a coordinate system rotating in the reference system together with the ring around O_1z_1. Its origin O_1 is the center of the ring and O_1z_1 is the symmetry axis of the cylinder. The angle α is defined as the angle of rotation.

The length of the radius vector connecting O and O_1 is $R = \sqrt{R_x^2 + R_y^2}$, where R_x and R_y are defined as:

$$\begin{aligned} R_x &= -R\cos\zeta, \\ R_y &= R\sin\zeta. \end{aligned} \tag{A.1}$$

Ideally, ζ is supposed to be zero, however, a deviation of $\pm 1^\circ$ in the actual experimental set-up made it necessary to include ζ as an additional parameter in the calculations.

Defining r as the radius of the CT d'Or ring, the coordinates of the ring in $Oxyz$ are:

$$\begin{aligned} x &= R_x + r\cos(\gamma + \alpha), \\ y &= R_y + r\sin(\gamma + \alpha). \end{aligned} \tag{A.2}$$

The equation of a line connecting two distinct points γ_1, γ_{1+k} on the ring is:

$$\begin{aligned} &x\cos\left(\alpha + \frac{\gamma_{1+k} + \gamma_1}{2}\right) + y\sin\left(\alpha + \frac{\gamma_{1+k} + \gamma_1}{2}\right) = \\ &R_x\cos\left(\alpha + \frac{\gamma_{1+k} + \gamma_1}{2}\right) + R_y\sin\left(\alpha + \frac{\gamma_{1+k} + \gamma_1}{2}\right) + r\cos\frac{\gamma_{1+k} - \gamma_1}{2}. \end{aligned} \tag{A.3}$$

In the system, rays are defined as lines, which go through γ_1, γ_{1+k} and the origin O. This condition holds for the angle α that satisfies the equation:

$$R_x\cos\left(\alpha + \frac{\gamma_{1+k} + \gamma_1}{2}\right) + R_y\sin\left(\alpha + \frac{\gamma_{1+k} + \gamma_1}{2}\right) = -r\cos\frac{\gamma_{1+k} - \gamma_1}{2}. \tag{A.4}$$

Substituting equation (A.1) into equation (A.4) results in:

$$\cos\left(\zeta + \alpha + \frac{\gamma_1 + \gamma_{1+k}}{2}\right) = \frac{r}{R}\cos\frac{\gamma_{1+k} - \gamma_1}{2}. \tag{A.5}$$

As any ray is characterized with two parameters, α and γ, the angle β between ray (α, γ) and the normal to the detector is:

$$\tan\beta = -\frac{R_y + r\sin(\gamma + \alpha)}{R_x + r\cos(\gamma + \alpha)}. \tag{A.6}$$

Therefore, the y-coordinate of the point where ray (α, γ) hits the detector in a distance D from O are:

$$y = -D\frac{R_y + r\sin(\gamma + \alpha)}{R_x + r\cos(\gamma + \alpha)}. \tag{A.7}$$

The stripe (j, k) is defined as the collectivity of rays, which pass the windows j and $j + k$. In order to describe a single window to window stripe, the points on the CT d'Or ring are defined according to Fig. A.2:

$$\gamma_1 = j \cdot \frac{2\pi}{197} + \frac{2\pi}{197} \cdot \frac{5}{8}, \tag{A.8}$$

$$\gamma_2 = \gamma_1 + \frac{2\pi}{197} \cdot \frac{3}{8}, \tag{A.9}$$

$$\gamma_{1+k} = \gamma_1 + k\frac{2\pi}{197}, \tag{A.10}$$

$$\gamma_{2+k} = \gamma_2 + k\frac{2\pi}{197}, \tag{A.11}$$

taking into account that the width of the shieldings is 5 mm and the width of the windows is 3 mm.

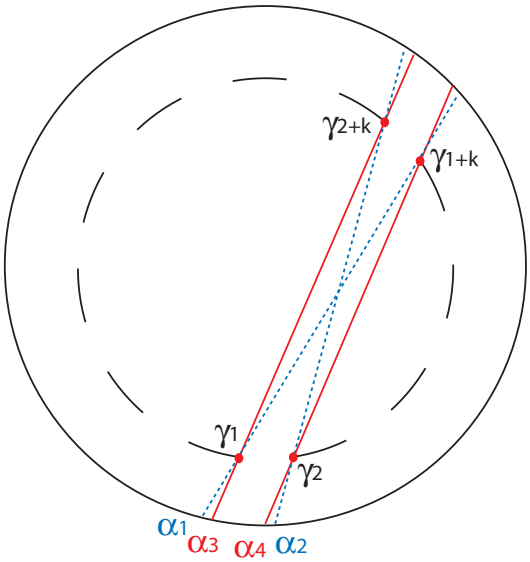

Figure A.2: *Angles which define a ray*

For any stripe $(j,\ k)$, there are four positions α_1, α_2, α_3 and α_4 of the ring. The first angle, α_1, denotes the source angle where exactly one ray runs from γ_1 to the point γ_{1+k}:

$$\alpha_1 = -\zeta - \frac{\gamma_1 + \gamma_{1+k}}{2} + \arccos\left(\frac{r}{R}\cos\frac{\gamma_{1+k} - \gamma_1}{2}\right). \tag{A.12}$$

Therefore, the last angle, α_2, describes the source angle where exactly one ray runs from γ_2 to the point γ_{2+k}:

$$\alpha_2 = -\zeta - \frac{\gamma_2 + \gamma_{2+k}}{2} + \arccos\left(\frac{r}{R}\cos\frac{\gamma_{2+k} - \gamma_2}{2}\right). \tag{A.13}$$

α_3 and α_4 denote the points where a ray runs from γ_1 to γ_{2+k} or γ_2 to γ_{1+k} respectively:

$$\alpha_3 = -\zeta - \frac{\gamma_1 + \gamma_{2+k}}{2} + \arccos\left(\frac{r}{R}\cos\frac{\gamma_{2+k} - \gamma_1}{2}\right), \tag{A.14}$$

$$\alpha_4 = -\zeta - \frac{\gamma_2 + \gamma_{1+k}}{2} + \arccos\left(\frac{r}{R}\cos\frac{\gamma_{1+k} - \gamma_2}{2}\right). \tag{A.15}$$

Then for each source impulse from the corresponding interval, all pixels between $y_{\min}$ and $y_{\max}$ have to be added. For all impulses between α_1 and α_3, $y_{\min}$ and $y_{\max}$ are defined as:

$$\begin{aligned} y_{\min} &= -D\frac{R_y + r\sin(\gamma_1 + \alpha)}{R_x + r\cos(\gamma_1 + \alpha)}, \\ y_{\max} &= -D\frac{R_y + r\sin(\gamma_{1+k}) + \alpha)}{R_x + r\cos(\gamma_{1+k} + \alpha)}. \end{aligned} \tag{A.16}$$

For all impulses between α_4 and α_2:

$$\begin{aligned} y_{\min} &= -D\frac{R_y + r\sin(\gamma_2 + \alpha)}{R_x + r\cos(\gamma_2 + \alpha)}, \\ y_{\max} &= -D\frac{R_y + r\sin(\gamma_{2+k} + \alpha)}{R_x + r\cos(\gamma_{2+k} + \alpha)}. \end{aligned} \tag{A.17}$$

And for all impulses between α_3 and α_4:

$$\begin{aligned} y_{\min} &= -D\frac{R_y + r\sin(\gamma_{1+k} + \alpha)}{R_x + r\cos(\gamma_{1+k} + \alpha)}, \\ y_{\max} &= -D\frac{R_y + r\sin(\gamma_{2+k} + \alpha)}{R_x + r\cos(\gamma_{2+k} + \alpha)}. \end{aligned} \tag{A.18}$$

Using these formulas, another program determined whether a data point belonged to a ray and if so to which one.

A.1.2. Data of the CT d'Or demonstrator

The coordinate system is depicted in Fig. A.3.

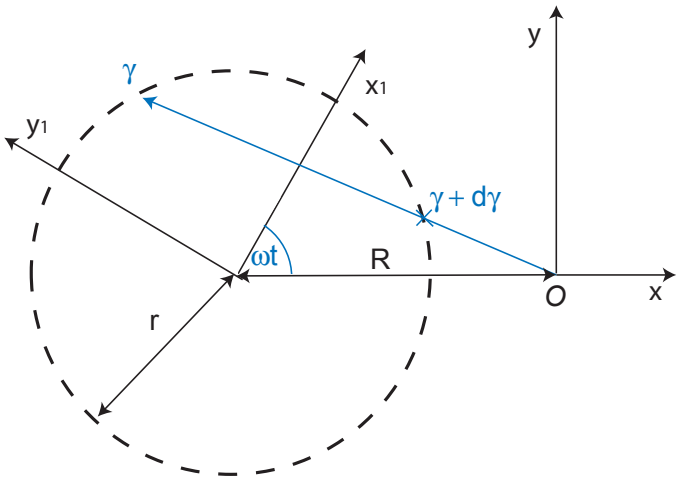

Figure A.3: *Coordinate system in the CT d'Or*

Any point of the ring is represented in Oxy as

$$\begin{aligned} x &= R + r\cos(\gamma + \omega t), \\ y &= r\sin(\gamma + \omega t). \end{aligned} \tag{A.19}$$

For a given point on the ring, $\gamma + d\gamma(t)$ is supposed to be the current position where line $O\gamma$ intersects the ring at the moment t. These values of γ are given by the relation

$$\cos\left(\gamma + \omega t + \frac{d\gamma}{2}\right) + \frac{r}{R}\cos\frac{d\gamma}{2} = 0. \tag{A.20}$$

Solving Eq. (A.20) relative to t gives

$$t = \left(\pi - \gamma - \frac{d\gamma}{2} - \arccos\left(\frac{r}{R}\cos\frac{d\gamma}{2}\right)\right)\frac{1}{\omega}. \tag{A.21}$$

Hence, for the detector located at point γ of the ring and for any given value $d\gamma$ a moment t can be found such that at this moment the ray hits the detector through the ring point $\gamma + d\gamma$. Therefore, for any window in the ring it is possible to find the time interval during which the detector is irradiated through this window.

Additionally, all detectors are read out simultaneously with frequency q_1, while the pulse frequency of the source of the C-arm device is q_2. Therefore, the position of the source in the moment of pulse ν is

$$\alpha_\nu^p = \alpha_0^p + \omega\frac{\nu}{q_2}, \tag{A.22}$$

where ω is the rotation velocity of the ring. Equivalently, the position of the source in the moment of readout i is

$$\alpha_i^r = \alpha_0^r + \omega\frac{i}{q_1}. \tag{A.23}$$

Only those α_i^r are interesting which satisfy the following conditions for a given value of index ν:

1. the detector is open to the source being in position α_ν^p
2. $\alpha_{i-1}^r < \alpha_\nu^p < \alpha_i^r$ so that event α_i^r happens either directly after event α_ν^p or both events coincide.

A.2. CT d'Or combined with the clinical CT system

$Oxyz$ is the reference system related to the CT d'Or ring, where O is the center of the ring. The reference system related to the CT scanner is $O_1x_1y_1z_1$, where O_1 corresponds to the isocenter. Let $\delta_x\delta_y\delta_z$ be coordinates of O_1 in $Oxyz$. The transformation from one reference system to the other is

$$\begin{pmatrix} x_1 \\ y_1 \\ z_1 \end{pmatrix} = \begin{pmatrix} \cos\theta_2 & 0 & \sin\theta_2 \\ 0 & 1 & 0 \\ -\sin\theta_2 & 0 & \cos\theta_2 \end{pmatrix} \begin{pmatrix} 1 & 0 & 0 \\ 0 & \cos\theta_1 & \sin\theta_1 \\ 0 & -\sin\theta_1 & \cos\theta_1 \end{pmatrix} \begin{pmatrix} x - \delta_x \\ y - \delta_y \\ z - \delta_z \end{pmatrix}, \tag{A.24}$$

where θ_1 and θ_2 are parameters of angular discrepancy between xyz and $x_1y_1z_1$. This can be written as

$$\begin{aligned} x_1 &= (x - \delta_x)\cos\theta_2 - (y - \delta_y)\sin\theta_1\sin\theta_2 + (z - \delta_z)\sin\theta_2\cos\theta_1, \\ y_1 &= (y - \delta_y)\cos\theta_1 + (z - \delta_z)\sin\theta_1, \\ z_1 &= -(x - \delta_x)\sin\theta_2 - (y - \delta_y)\sin\theta_1\cos\theta_2 + (z - \delta_z)\cos\theta_1\cos\theta_2. \end{aligned} \tag{A.25}$$

In $x_1y_1z_1$ the motion of the source is described with $\vec{R}$

$$\vec{R}(t) = \begin{pmatrix} R\cos(\omega t) \\ R\sin(\omega t) \\ 0 \end{pmatrix}. \tag{A.26}$$

The detector ring is described as a cylinder, the points of which in xyz are $\vec{r}$

$$\vec{r}(\beta, z) = \begin{pmatrix} r\cos\beta \\ r\sin\beta \\ z \end{pmatrix}. \tag{A.27}$$

A.2.1. Data of the CT d'Or demonstrator

Let $\vec{R}_0$ be the vector directed from O to the source. Let the ray emitted by the source hit point $\vec{r}(\beta, 0)$ through point $\vec{r}(\beta + \Delta\beta, z)$ of the ring cylinder. For this, the ray equality

$$\Delta\vec{r} \times \vec{R}_O = \Delta\vec{r} \times \vec{r} \tag{A.28}$$

is valid, where $\Delta\vec{r} = \vec{r}(\beta + \Delta\beta) - \vec{r}(\beta)$. In order to describe the orthogonal projection onto plane Oxy, only the z-coordinate of Eq. (A.28) is needed. The expanded form of this equation is

$$\begin{aligned} &R\cos(\omega t)\left(\cos\left(\beta + \frac{\Delta\beta}{2}\right)\cos\theta_2 - \sin\left(\beta + \frac{\Delta\beta}{2}\right)\sin\theta_1\sin\theta_2\right) + \\ &+ R\sin(\omega t)\sin\left(\beta + \frac{\Delta\beta}{2}\right)\cos\theta_1 = \\ &= r\cos\frac{\Delta\beta}{2} - \left(\delta_x\cos\left(\beta + \frac{\Delta\beta}{2}\right) + \delta_y\sin\left(\beta + \frac{\Delta\beta}{2}\right)\right). \end{aligned} \tag{A.29}$$

In order to solve this equation relative to t, it is rewritten as

$$\Omega_1\cos(\omega t) + \Omega_2\sin(\omega t) = \frac{r}{R}\cos\left(\frac{\Delta\beta}{2}\right) - \frac{1}{R}\left(\delta_x\cos\left(\beta + \frac{\Delta\beta}{2}\right) + \delta_y\sin\left(\beta + \frac{\Delta\beta}{2}\right)\right), \tag{A.30}$$

where Ω_1 and Ω_2 are defined as

$$\begin{aligned} \Omega_1 &= \cos\left(\beta + \frac{\Delta\beta}{2}\right)\cos\theta_2 - \sin\left(\beta + \frac{\Delta\beta}{2}\right)\sin\theta_1\sin\theta_2, \\ \Omega_2 &= \sin\left(\beta + \frac{\Delta\beta}{2}\right)\cos\theta_1. \end{aligned}$$

By introducing angle ϕ such that

$$\cos\phi = \frac{\Omega_1}{\sqrt{\Omega_1^2 + \Omega_2^2}}, \qquad \sin\phi = \frac{\Omega_2}{\sqrt{\Omega_1^2 + \Omega_2^2}},$$

Eq. (A.30) can be written as

$$\cos(\omega t - \phi) = \frac{r}{R\sqrt{\Omega_1^2 + \Omega_2^2}}\cos\left(\frac{\Delta\beta}{2}\right) - \epsilon, \tag{A.31}$$

where ϵ is defined as

$$\epsilon = \frac{r}{R\sqrt{\Omega_1^2+\Omega_2^2}}\left(\delta_x \cos\left(\beta+\frac{\Delta\beta}{2}\right)+\delta_y \sin\left(\beta+\frac{\Delta\beta}{2}\right)\right).$$

Equation A.31 has two solutions

$$\omega t = \phi \pm \arccos\left(\frac{r}{R\sqrt{\Omega_1^2+\Omega_2^2}}\cos\left(\frac{\Delta\beta}{2}\right)-\epsilon\right), \tag{A.32}$$

of which "+" is the needed one. For the special case when the CT d'Or device is perfectly aligned in the gantry ($\theta_1, \theta_2 = 0$), $\phi = \beta + \frac{\Delta\beta}{2}$ and $\epsilon = 0$ so that Eq. (A.32) simplifies to

$$\omega t = \beta + \frac{\Delta\beta}{2} + \arccos\left(\frac{r}{R}\cos\left(\frac{\Delta\beta}{2}\right)\right). \tag{A.33}$$

Let $\Delta\alpha = \frac{2\pi}{197}$ be the segment of the ring which corresponds to one shielding and one window. The moment of first readout is referred to as initial moment. The angle β_j is described in dependence of detector j,

$$\beta_j = (\lambda_1 + j)\Delta\alpha, \tag{A.34}$$

where λ_1, $0 \leq \lambda_1 < 1$, is a free parameter.

According to Eq. (A.32), the time interval, during which detector j can be seen from the source through window k, is $\Delta t = t_2 - t_1$

$$t1 = \left(\phi(\beta_j, \Delta\beta_1) + \arccos\left(c_1 \cos\frac{\Delta\beta_1}{2} - \epsilon_1(\beta_j, \Delta\beta_1)\right)\right)\frac{1}{\omega},$$
$$t2 = \left(\phi(\beta_j, \Delta\beta_2) + \arccos\left(c_2 \cos\frac{\Delta\beta_2}{2} - \epsilon_2(\beta_j, \Delta\beta_2)\right)\right)\frac{1}{\omega},$$

where

$$\Delta\beta_1 = k\Delta\alpha + \frac{\Delta S}{2}, \qquad \Delta\beta_2 = (k+1)\Delta\alpha - \frac{\Delta S}{2} \tag{A.35}$$

depends on the angular size of one shielding ΔS.

A.2.2. Data of the clinical CT

Using Eq. (A.25), a line of intersection of the iso-plane with the cylinder can be found easily. Since for the iso-plane $z_1 = 0$, it follows

$$z - \delta_z = (x - \delta_x)\frac{\sin\theta_2}{\cos\theta_1\cos\theta_2} + (y - \delta_y)\frac{\sin\theta_1}{\cos\theta_1}. \tag{A.36}$$

By inserting this equation into the first two equations of Eq. (A.25), one obtains the parametric representation of the line in $O_1x_1y_1$:

$$\begin{aligned} x_1(\beta) &= \frac{(r\cos\beta - \delta_x)\cos\theta_1}{\cos\theta_1\cos\theta_2}, \\ x_2(\beta) &= \frac{(r\sin\beta - \delta_y)\cos\theta_2 + (r\cos\beta - \delta_x)\sin\theta_2\sin\theta_1}{\cos\theta_1\cos\theta_2}. \end{aligned} \tag{A.37}$$

For a ray emitted from the source at position α and passing through points β_1 and β_2 defined by Eq. (A.37), the following relation must hold:

$$(x_1(\beta+\Delta\beta)-x_1(\beta))(R\sin\alpha-y_1(\beta))=(y_1(\beta+\Delta\beta)-y_1(\beta))(R\cos\alpha-x_1(\beta)). \quad \text{(A.38)}$$

Inserting Eq. (A.37) into Eq. (A.38) and simplifying the expression, results in Eq. (A.29), which can be used for the determination of position α given β_1 and $\Delta\beta$.

In order to determine the point the detector is hit by a given ray, the coordinate of this ray in the fan needs to be known. The equation of the ray emitted by the source from position α to point β_1 on the line defined by Eq. (A.37) is

$$x_1(y_1(\beta_1)-R\sin\alpha)+y_1(R\cos\alpha-x_1(\beta_1))=R(y_1(\beta_1)\cos\alpha-x_1(\beta_1)\sin\alpha). \quad \text{(A.39)}$$

This expression can be reformed to the equation of view $x_1\cos\phi+y_1\sin\phi=t$, where

$$t=\frac{y_1(\beta_1)R\cos\alpha-x_1(\beta_1)R\sin\alpha}{\sqrt{(y_1(\beta_1)-R\sin\alpha)^2+(R\cos\alpha-x_1(\beta_1))^2}} \quad \text{(A.40)}$$

is the distance of the line to the isocenter. The desired coordinate of the ray is $\psi=\arccos t$.

Let Δl be the size of the detector bin, D the source to detector distance, and N the number of detector elements. Taking into account the flying focus technique and the quarter detector offset, ray ψ hits detector bin i

$$i=\frac{\psi-\psi_0}{\Delta\psi},$$

where the resolution of the fan beam $\Delta\psi$ is

$$\Delta\psi=\frac{1}{2}\frac{\Delta\gamma}{D}$$

and

$$\psi_0=\frac{\pi}{2}-\left(N+\frac{1}{4}\right)\Delta\psi.$$

Again, the initial moment is the moment of first readout. The uncertainty of the ring position is modeled via parameter λ_2, $0\leq\lambda_2<1$, so that coordinates of points $\beta_1(j)$, $\beta_2(j)$ that characterize window j are

$$\beta_1(j)=(\lambda_2+j)\Delta\alpha \qquad \beta_2(j)=\beta_1(j)+\Delta W, \quad \text{(A.41)}$$

where ΔW is the size of the windows. This equation makes clear that λ_2 has to be handled independently from λ_1.

Bibliography

[AAMP08] AAMP. *The measurement, reporting and management of Radiation Dose in CT*. American Association of Physicists in Medicine, 2008.

[Ang05] W. Angerstein, editor. *Grundlagen der Strahlenphysik und radiologischen Technik in der Medizin*. H. Hoffmann GmbH Verlag, Berlin, 2005.

[Bar04] H.H. Barrett and K.J. Myers. *Foundations of Image Science*. Wiley Interscience, New Jersey, 2004.

[Bar85] H.H. Barret, W.E. Smith, K.J. Myers, T.D. Milster, and R.D. Fiete. Quantifying the performance of imaging systems. *Proc Soc Photo Opt Instrum Eng*, 535:65–69, 1985.

[Bar90] H.H. Barrett. Objective assessment of image quality: Effects of quantum noise and object variability. *Journal of the Optical Society of America A*, 7:1266–1278, 1990.

[Beu00] J. Beutel, H.L. Kundel, and R.L. Van Metter, editors. *Handbook of medical imaging - Volume 1. Physics and Psychophysics*. SPIE Press, 2000.

[BfS08] BfS. Umweltradioaktivität und Strahlenbelastung. Technical report, Bundesamt für Strahlenschutz, 2008.

[BfS10] BfS. Bekanntmachung der aktualisierten diagnostischen Referenzwerte für diagnostische und interventionelle Röntgenuntersuchungen. Technical report, Bundesamt für Strahlenschutz, 2010.

[Bog09] W. Bogdanich. Radiation overdoses point up dangers of CT scans. *The New York Times*, October 15, 2009.

[Bre06] D.J. Brenner and R.K. Sachs. Estimating radiation-induced cancer risks at very low doses: Rationale for using a linear no-threshold approach. *Radiation and Environmental Biophysics*, 44:253–256, 2006.

[Bri05] G. Brix, E. Nekolla, and J. Griebel. Strahlenexposition von Patienten durch diagnostische und interventionelle Röntgenanwendungen. *Radiologe*, 45:340–349, 2005.

[Bru10] C.C. Brunner, S.A. Hurowitz, S.F. Abboud, C. Hoeschen, and I.S. Kyprianou. Noise characterization of computed tomography using the covariance matrix. *Proc. SPIE*, 7622:76224Z, 2010.

[Buh03] E. Buhr, S. Guenther-Kohfahl, and U. Neitzel. Simple method for Modulation Transfer Function determination of digital imaging detectors from edge images. *Proc. SPIE*, 5030:877–884, 2003.

[Bur99] A.E. Burgess. The Rose model, revisited. *Journal of the Optical Society of America A*, 16:633–646, 1999.

[Bye09] J. Byers. ACR, ASNR call for CT scan, dosage protocols. *Health Imaging & IT*, November 2, 2009.

[Cat06] Catphan® 500 and 600 manual. Technical report, The Phantom Laboratory, 2006.

[Cor73] A. McLeod Cormack. Reconstruction of densities from their projections, with applications in radiological physics. *Physics in Medicine and Biology*, 18:195–207, 1973.

[Cra97] K. Cranley, B.J. Gilmore, G.W.A. Fogarty, and L. Desponds. Catalogue of diagnostic x-ray spectra and other data. Report No78, The Institute of Physics and Engineering in Medicine, 1997.

[DIN08] DIN. Bewertung und routinemäßige Prüfung in Abteilungen für medizinische Bildgebung - Teil 2-6: Konstanzprüfungen - Leistungsmerkmale zur Bildgebung von Röntgeneinrichtungen für die Computertomographie (IEC 61223-2-6:2006); Deutsche Fassung EN 61223-2-6:2007. Technical report, Deutsches Institut für Normung e.V., 2008.

[Dan09] J.E. Danielsa and M. Drakopoulos. High-energy x-ray diffraction using the Pixium 4700 flat-panel detector. *Journal of Synchrotron Radiation*, 16:463–468, 2009.

[Dun01] C.F. Dunkl and Y. Xu. *Orthogonal Polynomials of Several Variables In: Encyclopedia of Mathematics and its Applications vol. **81***. Cambridge Univ. Press, 2001.

[Efr79] B. Efron. Bootstrap methods: Another look at the jackknife. *The Annals of Statistics*, 7:1–26, 1979.

[FDA10] FDA. Initiative to reduce unnecessary radiation exposure from medical imaging. Technical report, U.S. Food and Drug Administration, 2010.

[Faz09] R. Fazel, H.M. Krumholz, Y. Wang, J.S. Ross, J. Chen, H.H. Ting, N.D. Shah, K. Nasir, A.J. Einstein, and B.K. Nallamothu. Exposure to low-dose ionizing radiation from medical imaging procedures. *The New England Journal of Medicine*, 361:849–857, 2009.

[Fei05] L.E. Feinendegen. Evidence for beneficial low level radiation effects and radiation hormesis. *The British Journal of Radiology*, 78:3–7, 2005.

[Flo06] T.G. Flohr, C.H. McCollough, H. Bruder, M. Petersilka, K. Gruber, C. Süß, M. Grasruck, K. Stierstorfer, B. Krauss, R. Raupach, A.N. Primak, A. Küttner, S. Achenbach, C. Becker, A. Kopp, and B.M. Ohnesorge. First performance evaluation of a dual-source (DSCT) system. *European Radiology*, 16:256–268, 2006.

[Fuc01] T.O.J. Fuchs, J.U. Krause, and W.A. Kalender. Measurement of 3D spatial resolution in multi-slice spiral computed tomography. *Physica Medica*, 17:129–134, 2001.

[Fuj92] H. Fujita, D.-Y. Tsai, T. Itoh, K. Doi, J. Morishita, K. Ueda, and A. Ohtsuka. A simple method for determining the Modulation Transfer Function in digital radiography. *IEEE Transactions on Medical Imaging*, 11(1):34–39, 1992.

[Goe10] T. Goetz. From success of the fab four, a key driver of health-care costs arose. *The Washington Post*, February 10, 2010.

[Gof92] J.W. Gofman. Supra-linear dose-response for radiation-induced cancer: no basis for Piepho's doubt. *Health physics*, 63:236–237, 1992.

[Gra00] M. Grass, T. Köhler, and R. Proksa. 3D cone-beam CT reconstruction for circular trajectories. *Physics in Medicine and Biology*, 45:329–347, 2000.

[Gre04] H. Greess, J. Lutze, A. Nömayr, H. Wolf, T. Hothorn, W.A. Kalender, and W. Bautz. Dose reduction in subsecond multislice spiral CT examination of children by online tube current modulation. *European Radiology*, 14:995–999, 2004.

[Han79] K.M. Hanson. Detectability in computed tomographic images. *Medical Physics*, 6:441–451, 1979.

[Har10] T. Hara, K. Ichikawa, S. Sanada, and Y. Ida. Image quality dependence on in-plane positions and directions for MDCT images. *European Radiology*, 75:114–121, 2010.

[Her08b] H. de las Heras. *Development and test of a new scanning geometry for Computed Tomography*. PhD thesis, Technical University of Munich, Germany, 2008.

[Hot31] H. Hotelling. The generalisation of Student's ratio. *The Annals of Mathematical Statistics*, 2:360–378, 1931.

[Hou73] G.N. Hounsfield. Computerized transverse axial scanning (tomography): Part 1. Description of system. *British Journal of Radiology*, 46:1016–1022, 1973.

[Hsi03] J. Hsieh. *Computed Tomography : Principles, Design, Artifacts, and Recent Advances*. SPIE Press monograph PM114, 2003.

[ICRP07] ICRP. Managing patient dose in multi-detector computed tomography (MDCT). *Annals of the ICRP*, 102, 2007.

[ICRU96] ICRU. Report 54: Medical imaging - The assessment of image quality. Technical report, International Commission on Radiation Units and Measurements, 1996.

[IEC03] IEC. 62220-1: Medical electrical equipment - characteristics of digital x-ray imaging devices - Part 1: Determination of the detective quantum efficiency. Technical report, International Electrotechnical Commission, 2003.

[IEC04] IEC. CEI/IEC 61223-3-5:2004 Evaluation and routine testing in medical imaging departments - Part 3-5: Acceptance tests - Imaging performance of computed tomography X-ray equipment. International Standard, International Electrotechnical Commission, Geneva, Switzerland, November 2004.

[IEC06] IEC. CEI/IEC 61223-2-6:2006 Evaluation and routine testing in medical imaging departments - Part 2-6: Constancy tests - Imaging performance of computed tomography X-ray equipment Edition 2.0. International Standard, International Electrotechnical Commission, Geneva, Switzerland, November 2006.

[ISO99] ISO. X and gamma reference radiation for calibrating dosemeters and doserate meters and for determining their response as a function of photon energy - Part 3: Calibration of area and personal dosemeters and the measurement of their response as a function of energy and angle of incidence. Technical report, International Organization of Standardization, 1999.

[ImPACT06] ImPACT. Report 06013: 32 to 64 slice CT scanner comparison report version 14. Technical report, NHS Purchasing and Supply Agency, 2006.

[ImPACT09] ImPACT. Comparative specifications - 64 slice CT scanners. Technical report, NHS Purchasing and Supply Agency, 2009.

[ImPACT10] ImPACT. Market review - advanced CT scanners for coronary angiography. Technical report, NHS Purchasing and Supply Agency, 2010.

[KCA04] KCARE. MHRA 04011: Comparative specifications of multipurpose C-arm systems. Technical report, King's Centre for the Assessment of Radiological Equipment, 2004.

[Kac06] M. Kachelriess, M. Knaup, C. Penssel, and W.A. Kalender. Flying focal spot (FFS) in cone-beam CT. *IEEE Transactions on Nuclear Science*, 53:1238–1247, 2006.

[Kak01] A.C. Kak and M. Slaney. *Principles of Computerized Tomographic Imaging*. Society of Industrial and Applied Mathematics, 2001.

[Kal05] W.A. Kalender. *Computed Tomography*. Publics Corporate Publishing, Erlangen, 2005.

[Kal07] W.A. Kalender and Y. Kypriakou. Flat-detector computed tomography (FD-CT). *European Radiology*, 17:2767–2779, 2007.

[Kal90] W.A. Kalender, Wolfgang Seissler, Ernst Klotz, and Peter Vock. Spiral volumetric CT with single-breath-hold technique, continuous transport, and continuous scanner rotation. *Radiology*, 176:181–183, 1990.

[Kal99] W.A. Kalender, H. Wolf, C. Suess, M. Gies, H. Greess, and W. Bautz. Dose reduction in CT by on-line tube current control: Principles and validation on phantoms and cadavers. *European Radiology*, 9:323–328, 1999.

[Kri09] F.L. Kritz. Adding up the radiation from scans. *The Washington Post*, October 6 October 6, 2009.

[Kwa07] A.L.C. Kwan, J.M. Boone, K. Yang, and S.-Y. Huang. Evaluation of the spatial resolution characteristics of a cone-beam breast CT scanner. *Medical Physics*, 34:275–281, 2007.

[Kyp05a] I.S. Kyprianou, A. Ganguly, S. Rudin, D.R. Bednarek, B.D. Gallas, and K.J. Myers. Efficiency of the human observer compared to an ideal observer based on a generalized NEQ which incorporates scatter and geometric unsharpness: Evaluation with a 2AFC experiment. *Proc. SPIE*, 5749:251–262, 2005.

[Kyp05b] I.S. Kyprianou, S. Rudin, D.R. Bednarek, and K.R. Hoffmann. Generalizing the MTF and DQE to include x-ray scatter and focal spot unsharpness: Application to a new microangiographic system. *Medical Physics*, 32(2):613–626, 2005.

[Kyp06a] I.S. Kyprianou, A. Badano, B.D. Gallas, S. Park, and K.J. Myers. A practical method for measuring the H-matrix of digital x-ray and cone beam CT imaging systems. *Proc. SPIE*, 6142:61421U, 2006.

[Kyp06b] I.S. Kyprianou, S. Paquerault, B.D. Gallas, A. Badano, S. Park, and K.J. Myers. Framework for determination of geometric parameters of a cone beam CT scanner for measuring the system response function and improved object reconstruction. In *Biomedical Imaging: Macro to Nano. 3rd IEEE International Symposium*, pages 1248–1251, Washington DC, 2006. ISBI, IEEE.

[Kyp07] I.S. Kyprianou, A. Badano, B.D. Gallas, and K.J. Myers. A method to estimate the point response function of digital x-ray detectors from edge measurements. *Proc. SPIE*, 6510:65100B, 2007.

[Kyp08] I.S. Kyprianou, A. Badano, B.D. Gallas, and K.J. Myers. Singular value description of a digital radiographic detector: Theory and measurements. *Medical Physics*, 35(35):4744–4756, 2008.

[Kyp09] I.S. Kyprianou, A. Badano, S. Park, H. Liu, and K.J. Myers. Noise and signal detection in digital x-ray detectors using the spatial definition of SNR. *Proc. SPIE*, 7258:725819, 2009.

[Liu09] H. Liu, I.S. Kyprianou, A. Badano, K.J. Myers, R.J. Jennings, S. Park, R.V. Kaczmarek, and K. Chakrabarti. SKE/BKE task based ideal observer SNR methodology for mammography. *Proc. SPIE*, 7258:72581D, 2009.

[Maz07] S.R. Mazin, J. Star-Lack, N.R. Bennett, and N.J. Pelc. Inverse-geometry volumetric CT system with multiple detector arrays for wide field-of-view imaging. *Medical Physics*, 34:2133–2142, 2007.

[Mos06] M. Moscovitch, T.J. St. John, J.R. Cassata, P.K. Blake, J.E. Rotunda, M. Ramlo, K.J. Velbeck, and L.Z. Luo. The application of LiF:Mg,Cu,P to large scale personnel dosimetry: current status and future directions. *Radiation Protection Dosimetry*, 119:248–254, 2006.

[Pad05] R. Padgett and C.J. Kotre. Development and application of programs to measure modulation transfer function, noise power spectrum and detective quantum efficiency. *Radiation Protection Dosimetry*, 117:282–287, 2005.

[Rad17] J. Radon. Über die Bestimmung von Funktionen durch ihre Integralwerte längs gewisser Mannigfaltigkeiten. *Akademie der Wissenschaften, Leipzig*, 69:262–277, 1917.

[Rie78] S.J. Riederer, N.J. Pelc, and D.A. Chesler. The noise power spectrum in computed x-ray tomography. *Physics in Medicine and Biology*, 23:446–454, 1978.

[RoeV02] Peinsipp, Roos, and Weimer. *Röntgenverordnung - RöV: Verordnung über den Schutz vor Schäden durch Röntgenstrahlung*. Forkel Verlag, 2003.

[Schl06] H. Schlattl, O. Tischenko, Y. Xu, and C. Hoeschen. Scatter noise correction of detector signals for projection-based imaging. Technical report, European patent application PLA 06A01, Submitted on 10/02/2006.

[Schl08] H. Schlattl and C. Hoeschen. The built-in capacity of CT D'Or's static ring for scatter correction. *Proc. SPIE*, 6513:651352, 2008.

[Schm04] T.G. Schmidt, R. Fahrig, N.J. Pelc, and E.G. Solomon. An inverse-geometry volumetric CT system with a large-area scanned source: A feasibility study. *Medical Physics*, 31(9):2623–2627, 2004.

[Tis05] O. Tischenko, C. Hoeschen, and E. Buhr. Reduction of anatomical noise in medical x-ray images. *Radiation Protection Dosimetry*, 114:69–74, 2005.

[Tis06] O. Tischenko, Y. Xu, and C. Hoeschen. A new scanning device in CT with dose reduction potential. *Proc. SPIE*, 6142:61422L–1, 2006.

[Tis10] O. Tischenko, A. Schegerer, Y. Xu, and C. Hoeschen. Properties of a parameterization of radon projection by the reconstruction on circular disc. *Proc. SPIE*, 7622:76222F, 2010.

[Tur01] H. Turbell. *Cone-beam reconstruction using filtering backprojection*. PhD thesis, Linköpings Universitet, Sweden, 2001.

[Ulr04] R. Ulrich and J. Miller. Threshold estimation in two-alternative forced-choice (2AFC) tasks: The Spearman-Kärber method. *Perception & Psychophysics*, 66:517–533, 2004.

[Wag79] R.F. Wagner, D.G. Brown, and M.S. Pastel. Application of information theory to the assessment of computed tomgraphy. *Medical Physics*, 6:83–94, 1979.

[Wal06] B.F. Wall, G.M. Kendall, A.A. Edwards, S. Bouffler, C.R. Muirhead, and J.R. Meara. What are the risks from medical x-rays and other low dose radiation? *The British Journal of Radiology*, 79:285–294, 2006.

[Wat10] H. Watanabe, E. Honda, and T. Kurabayashi. Modulation transfer function evaluation of cone beam computed tomography for dental use with the oversampling method. *Dentomaxillofacial Radiology*, 39:28–32, 2010.

[Xu06a] Y. Xu, O. Tischenko, and C. Hoeschen. A new reconstruction algorithm for Radon data. *Proc. SPIE*, 61422:791–798, 2006.

[Xu06b] Y. Xu. A new approach to the reconstruction of images from Radon projections. *Advances in Applied Mathematics*, 36:388–420, 2006.

[Xu07a] Y. Xu, O. Tischenko, and C. Hoeschen. Image reconstruction by OPED algorithm with averaging. *Numerical Algorithms*, 45:179–193, 2007.

[Xu07b] Y. Xu and O. Tischenko. Fast OPED algorithm for reconstruction of images from radon data. *East Journal of Approximations*, 13:427–444, 2007.

[Xu09] Y. Xu, O. Tischenko, and C. Hoeschen. Fast implementation of the image reconstruction algorithm OPED. *Proc. SPIE*, 7258:72585F, 2009.

Acknowledgments

This work would not exist without the help of numerous people who I want to thank here:

- Prof. Dr. Dr. Herwig G. Paretzke for giving me the possibility to work on this topic under his supervision and providing experienced advice on my problems.

- Prof. Dr. Christoph Hoeschen for giving me the chance to work in his department in this very interesting field of research. His support, motivation and scientific guidance were essential for this work. Especially, I want to thank him for arranging my stay at the FDA.

- Iacovos "Jake" Kyprianou, Ph.D., for giving me the chance to spend three months at the FDA. Under his patient supervision I learned tons of theory about imaging and his support and numerous ideas were essential for this work. Especially, I want to thank him for the time he still finds to supervise me even though I long left the FDA.

- Dr. Helmut Schlattl for always being available for me and for taking care of all my small and large scientific, administrative and computer problems. His sensible and careful corrections thoroughly improved this work.

- Dr. Oleg Tischenko for helping me with the reconstruction of the CT d'Or images. Especially, I want to thank him for always having time for me and patiently answering all my questions in detail.

- Dr. Hugo de las Heras for teaching me everything about the CT d'Or, providing me with his programs and allowing me to use his figures in my work. Especially, I want to thank him for providing me shelter and taking care of me during my time in Washington.

- Bernhard Renger from the Hospital rechts der Isar for spending numerous evenings in the clinic with me, taking images and helping me to develop the most appropriate set-up and measurement procedure.

- Dr. Matthias Greiter and Dr. Felix Schöfer for always being available for fruitful discussions and answering all my countless questions.

- Tilman Janzen for extensively proofreading my work and providing moral support whenever needed.

- Kyle Myers, Ph.D., and Aldo Badano, Ph.D., for allowing me to work at the FDA and giving helpful input to my work.

- Samir Abboud for measuring the dose in the FDA system and sending me all the additional information I needed to evaluate the data. Especially, I want to thank him for spending hours with me in the machine shop helping me to build my phantoms.

- Stefanie Hurowitz for acquiring the images at the FDA for me, even if it sometimes took several attempts till it worked the way we wanted it to.

- Werner Panzer for helping me to calibrate the TLDs and answering all my numerous questions about this topic.

- The Auswertungsstelle of the Helmholtz Zentrum München, and especially Markus Figel, for providing the TLDs, reading them out, and patiently answering all my questions.

- The machine shop of the Helmholtz Zentrum München, and especially Martin Scherer, for always processing my stuff as fast as possible.

- The whole Department of Medical Radiation Physics and Diagnostics for the very kind working atmosphere and for scientific and moral support whenever needed.

- My family and friends for always supporting and helping me, for their leniency and patience.

Furthermore I want to thank

- The German Academic Exchange Service, DAAD, for funding two months of my stay at the FDA.

- The Life Science Foundation for unbureaucratically financing the third month of my stay in the USA.